TAMPEREEN TEKNILLINEN YLIOPISTO

JUHO PELTOLA

DYNAMICS IN A CIRCULATING FLUIDIZED BED: EXPERIMENTAL AND NUMERICAL STUDY

Master of Science Thesis

Examiners: Docent Pentti Saarenrinne, D.Tech Markus Honkanen
Examiners and title approved in the Faculty of Automation, Mechanical and Material Technology Council meeting on June 3rd 2009

ABSTRACT

TAMPERE UNIVERSITY OF TECHNOLOGY
Master's Degree Programme in Mechanical Engineering
PELTOLA, JUHO: Dynamics in a Circulating Fluidized Bed: Experimental and Numerical Study
Master of Science Thesis, 95 pages
October 2009
Major: Heat Transfer and Fluid Mechanics
Examiners: Docent Pentti Saarenrinne, D.Tech Markus Honkanen
Keywords: fluidized bed, CFB, experimental, numerical, CFD, multiphase, Euler-Euler, PIV, high-speed imaging, shadowgraphy

The introduction of particles to create a fluidized bed combustor increases mixing and reduces temperature fluctuations, allowing emission reduction and a wider range of fuels. The particles and combustion air create a complicated gas-solid multiphase flow. Mathematical modelling of such flows is very challenging and the simulations require considerable computational capacity. Improving the performance of fluidized bed combustors requires knowledge of the particle motion in the reactor. As a result there is a need for a quick, time-averaged simulation method that could be used as a design tool in the industry.

This thesis concentrates on the particle dynamics of a non-reacting, pilot-scale Circulating Fluidized Bed (CFB). The particle motion was studied by applying image based measurements and transient computer simulations with the Eulerian two-fluid approach. The goal for the measurements was to provide detailed information about the particle behaviour for the validation of transient and time-averaged simulations, and for modelling parameter definition.

For the simulations, the goal was to evaluate the feasibility of using a solver based on the OpenFOAM open source code library to simulate circulating fluidized beds. Meaningful simulation of the pilot-scale CFB required modification of the Eulerian multiphase solver included in the public OpenFOAM release. The results, speed, stability and parallel efficiency of the modified solver were found to be competitive.

Shadowgraphy was the illumination method of choice for the measurements. Local and instantaneous particle volume fractions were determined by correlating the grey-scale values of the recorded images. Particle velocities were measured with the Particle Image Velocimetry (PIV) method based on a statistical determination of the particle displacement from the images. For the particle small-scale random motion a method based on change in the PIV-correlation peak width was used. The method was implemented – together with a PIV algorithm – in MATLAB. Particle Tracking Velocimetry (PTV) methods for the measurement of individual particle properties were reviewed, developed and validated, but were only applied to the measurement of particle size distribution from a separate sample.

Results are presented for simulated and measured particle mean velocities and volume fractions, as well as for the measured standard deviation values, the volume fraction weighted mean particle velocities, the Reynolds stresses and the particle small-scale random motion.

TIIVISTELMÄ

TAMPEREEN TEKNILLINEN YLIOPISTO
Konetekniikan koulutusohjelma
PELTOLA, JUHO: Dynamiikka kiertoleijupedissä: kokeellinen ja laskennallinen tutkimus
Diplomityö, 95 sivua
Lokakuu 2009
Pääaine: Lämmönsiirto- ja virtaustekniikka
Tarkastaja: dosentti Pentti Saarenrinne, TkT Markus Honkanen
Avainsanat: leijupeti, kokeellinen, laskennallinen, virtaussimulointi, CFD, monifaasi, Euler-Euler, PIV, PTV, suurnopeuskuvaus, varjokuvaus

Leijupetikattila on erityisesti biopolttoaineiden polttoon kehitetty lämpövoimaloiden kattilatyyppi. Leijupetikattilan palotilassa on kiinteitä partikkeleja, joita leijutetaan alapuolelta pumpatulla polttoilmalla. Reaktorissa olevat partikkelit tehostavat sekoittumista ja tasaavat lämpötilan vaihteluja. Tämä mahdollistaa päästöjen alentamisen ja laajemman polttoainevalikoiman. Tämä on erityisen tärkeää käytettäessä biopolttoaineita, joiden laatu voi olla hyvin vaihteleva.

Partikkelit ja polttoilma muodostavat leijupetikattilaan fysikaalisesti huomattavan monimutkaisen kaksifaasivirtauksen, jonka mallintaminen on hyvin vaativaa. Nykyään leijupetejä simuloidaan ajasta riippuvilla simulaatioilla, mutta laskennallisesti ne ovat hyvin raskaita virtauksen epävakaan luonteen vaatimista pitkistä keskiarvotusajoista johtuen. Kattiloiden suorituskyvyn parantaminen vaatii tietoa partikkelien liikkeestä ja jakautumisesta. Täten on olemassa tarve nopealle, aikakeskiarvotetulle simulointimenetelmälle, joka soveltuisi teollisuuden suunnittelukäyttöön.

Työ keskittyy partikkelien dynamiikkaan reagoimattomassa pilottikoon kiertoleijupedissä, mitä tarkastellaan sekä mittausten että numeerisen mallinnuksen avulla. Tutkittavan laitteen koko sallii nopeiden kaksiulotteisten simulointien ja kehittyneiden kuvaan perustuvien mittausmenetelmien käytön, joka ei olisi mahdollista teollisen mittakaavan laitteessa. Mittausten tavoitteena on tuottaa yksityiskohtaista tietoa partikkelien liikkeestä ajasta riippuvien ja aikakeskiarvotettujen simulointien validointiin ja malliparametrien määrittämiseksi.

Virtaussimuloinneissa on käytetty ajasta riippuvaa Euler-Euler -kaksinestemallia. Tavoitteena on ollut selvittää OpenFOAM-nimiseen vapaan lähdekoodin kirjastoon perustuvan virtausratkaisijan soveltuvuutta leijupetien mallinnukseen. Ohjelman julkinen levitysversio sisältää tarkoitukseen mahdollisesti soveltuvan ratkaisijan ja lähes kaikki tarvittavat mallit. Ratkaisijaa testattaessa kuitenkin paljastui, että merkityksellinen kiertoleijun simulointi vaatii OpenFOAMin ratkaisijan muokkaamista. Ongelmat liittyivät pääasiassa ratkaisijan käyttäytymiseen suurilla partikkelien tilavuusosuuksilla, erityisesti käytettäessä kineettiseen teoriaan perustuvaa partikkeli-partikkeli -vuorovaikutusmallia. Ongelmat ilmenivät ratkaisujen epäfysikaalisina tilavuusosuuksina sekä ratkaisijan yleisenä epävakautena.

Ongelmien poistamiseksi ratkaisijaan on tehty muutoksia. Kineettisen teorian partikkelien tilavuusosuutta rajoittavan termin, kitkapaineen (engl. *frictional pressure*),

käsittely on muutettu implisiittisemmäksi. Partikkelien tilavuusosuuden siirtoyhtälölle on lisätty adaptiivinen alirelaksointi sekä sen ajasta riippuvassa ratkaisijassa vaatimat lisäiteraatiot. Näillä muutoksilla ratkaisijan vakaus parantui, mutta käytetty kitkapaineen käsittely mahdollisti sen toimimisen epäfysikaalisena liikemäärälähteenä. Tästä johtuen ratkaisija ei ollut edelleenkään kyllin vakaa. Ongelman ratkaisemiseksi on kehitetty algoritmi rajoittamaan kitkapaineen suuruutta hetkellisesti ja laskentaelementeittäin. Rajoitin perustuu kitkapaineen tuottaman vuon ja muun virtauskentän vertailuun. Muutosten jälkeen ratkaisija on osoittautunut tulosten, nopeuden, vakauden ja rinnakkaistumisen osalta kilpailukykyiseksi.

Numeeriseen vakauden parannuttua oli mahdollista keskittyä tarvittaviin fysikaalisiin malleihin. Niiden osalta ratkaisijaan on lisätty suodatettuihin liikemääräyhtälöihin perustuva alihilaturbulenssimalli, kaksi partikkelivirtausmallinnuksessa yleisesti käytettyä reunaehtoa sekä muutamia alimalleja kineettiseen teoriaan.

Sakean suspension mittauksissa valon läpäisykyky on usein rajoittava tekijä. Siten laitteen litteästä, lähes kaksiulotteisesta geometriasta johtuen kuvausmenetelmäksi on valittu varjokuvantaminen. Tällöin partikkelivirtausta kuvataan vastavaloon ja partikkelit näkyvät kuvissa varjoina. Kuvaan tallennettu valon intensiteetti kuvaa suspension läpäisemän valon määrää. Tällöin partikkelien paikallista ja hetkellistä tilavuusosuutta voidaan arvioida korreloimalla kuvan harmaasävyjä tilavuusosuuksien kanssa. Menetelmän heikkoutena on tarkkuus suurilla partikkelien tilavuusosuuksilla, jolloin valo ei juuri läpäise suspensiota.

Työssä tarkastellaan kahta partikkelien nopeuksien määritykseen soveltuvaa menetelmä. Particle Image Velocimetry (PIV) on partikkelikuvien tilastolliseen korrelointiin perustuva menetelmä, joka antaa partikkelien todennäköisimmän nopeuden mittaustilavuudessa. Menetelmän hyviä puolia ovat varmatoimisuus ja soveltuvuus laajalle skaalalle suspension tiheyksiä. Toinen tarkasteltu menetelmä on Particle Tracking Velocimetry (PTV), jossa tunnistetaan kuvista yksittäisiä partikkeleita ja määritetään niiden nopeudet. Menetelmän vahvuuksia ovat paras mahdollinen paikkaresoluutio, mahdollisuus partikkelien koon ja muodon määrittämiseen sekä se, että jokainen nopeus vastaa todellista partikkelia. Partikkelien tunnistaminen on kuitenkin algoritmisesti haastavaa, joten nopeuksien määritys on laskennallisesti hidasta verrattuna PIV:iin. Tämä korostuu erityisesti kiertoleijun kaltaisissa sakeissa suspensioissa. Tästä johtuen menetelmä soveltuu vain harvan suspension alueille. Tässä diplomityössä partikkelien nopeuksien määritykseen on käytetty PIV-menetelmää. PTV-menetelmiä on kehitetty ja validoitu, mutta sovellettu ainoastaan partikkelien kokojakauman määritykseen erillisestä näytteestä.

Mittauksia suoritettiin kahdella eri mittausalalla, jotta sekä suuren että pienen skaalan ilmiöt saatiin mitattua. Suurempi mittausikkuna kattoi koko nousuputken leveyden. Tällöin on mahdollista tutkia partikkeliklusterien kehitystä ja vuorovaikutusta, mutta yksittäisten partikkelien havainnoiminen on mahdotonta eikä nopeuden määrityksen paikkaresoluutio riitä jyrkimpien nopeusgradienttien mittaamiseen. Suuri mittausalue sallii nousuputken nopeuksien ja tilavuusosuuksien määrityksen laajalta alalta, antaen hyvän yleiskuvan virtauksesta. Suuresta mittausalasta johtuen valaisuun on käytetty loisteputkia.

Pienempi mittausalue oli kooltaan 40x30 mm, joka salli valaisemisen pulssitetulla diodilaserilla. Tällöin yksittäiset partikkelit erottuvat selvästi, eikä liike-epätarkkuutta esiinny. Näistä hyvälaatuisista kuvista nopeuden 1,65 mm suuremmat skaalat voidaan mitata tarkasti, lukuun ottamatta sakeimpia alueita, joilla valo ei mitattavasti läpäise suspensiota. Tarkka nopeuksien määritys ja kuvan harmaasävystä korreloitu, yhtäaikainen tilavuusosuuden määritys sallii tilavuusosuuspainotettujen keskiarvojen ja Reynoldsin jännitysten laskennan. Kyseiset suureet ovat tärkeitä aikakeskiarvotetulle mallinnukselle.

Kuvausmenetelmä, jossa yksittäiset partikkelit ovat eroteltavissa, sallii myös partikkelien mittaustilavuutta pienemmän skaalan satunnaisen liikkeen tilastollisen määrityksen PIV-korrelaation tulosten perusteella. Dijkhuizen et al. (2007) ehdottamaa menetelmää sovellettiin partikkelien varjokuviin. Menetelmä implementoitiin MATLAB-ympäristöön yhdessä PIV-algoritmin kanssa ja validoitiin synteettisillä partikkelikuvilla.

Mittaukset ja simuloinnit suoritettiin kahdella eri leijutusnopeudella. Partikkelien keskinopeuksille ja -tilavuusosuuksille esitetään simuloituja ja mitattuja tuloksia. Lisäksi esitetään mittaustuloksista lasketut arvot tilavuusosuuspainotetulle partikkelien keskinopeudelle, Reynoldsin jännityksille sekä partikkelien pienen skaalan satunnaisen liikkeen energialle.

PREFACE

This Master of Science thesis was written at Tampere University of Technology (TUT) in the Department of Energy and Process Engineering. The measurement portion of the thesis is part of the research project Time-Averaged CFD Modelling of Circulating Fluidized Beds (TAveCFD_CFB) funded by Tekes, the Finnish Funding Agency for Technology and Innovation. The simulation and CFD-solver development portions of the thesis have been carried out on my spare time, although they are partially based on my work at VTT, the Technical Research Institute of Finland, during the summer of 2008.

Firstly, I would like to thank my supervisor Pentti Saarenrinne for opportunity and encouragement to take part in interesting research during the last two and a half years, and most recently in the TAveCFD_CFB project. The expertise of the whole TUT experimental fluid dynamics team in image-based measurements – built over several years – has enabled the measurements of this thesis to be carried out. My examiner, Markus Honkanen deserves special thanks for his wide knowledge of multiphase flow measurements and his willingness to share his knowledge. The shadowgraphy PTV method discussed in Sections 6.3.1 and 6.3.2 owes a lot to his research.

The knowledge and guidance of Sirpa Kallio (VTT) and Veikko Taivassalo (VTT) on all things fluidized and Eulerian multiphase modelling have also been vital for my work. Alf Hermanson (Åbo Akademi University), who supervised the construction of the experimental device, constructed much of the measurement setup and operated the CFB during the measurements, has also been indispensable for the experimental research. I would also like to thank Ville Tossavainen (TUT), for introducing me to OpenFOAM, discussion and help with the TUT computational cluster, and Alberto Passalacqua (Iowa State University), for discussion and provision of material related to the twoPhaseEulerFoam solver, including the source code used in his PhD thesis.

Finally, I would like to thank my friends and family, for bringing balance to work and leisure, and Essi, for her patience, love and support.

Tampere, September 22nd 2009

Juho Peltola

TABLE OF CONTENTS

ABBREVIATIONS AND SYMBOLS

Abbreviations

AC	Auto-Correlation
CC	Cross-Correlation
CCD	Charge Coupled Device
CFB	Circulating Fluidized Bed
CFD	Computational Fluid Dynamics
CMOS	Complementary Metal Oxide Semiconductor
DOF	Depth of Field
FDM	Finite Difference Method
FEM	Finite Element Method
FFT	Fast Fourier Transform
FVM	Finite Volume Method
GPVS	Glare Point Velocimetry and Sizing
IPI	Interferometric Particle Imaging
KTGF	Kinetic Theory for Granular Flow
LES	Large-Eddy Simulation
PIV	Particle Image Velocimetry
PTV	Particle Tracking Velocimetry
RANS	Reynolds-Averaged Navier-Stokes
RMS	Root Mean Square
SGS	Sub-Grid Scale

Mathematical symbols

Normal typeface denotes a scalar variable.
Bold typeface denotes a vector, tensor or matrix variable.

Roman symbols

A	Surface area
$\boldsymbol{A}$	Coefficient matrix
A_d	Momentum transfer coefficient, drag
A_l	Momentum transfer coefficient, lift
A_{vm}	Momentum transfer coefficient, virtual mass

$\mathcal{A}_{\varphi}$	Coefficient matrix of discretized momentum equation for phase φ
C_{φ}	A constant related to φ
C_D	Drag coefficient
C_l	Lift coefficient
C_{vm}	Virtual mass coefficient
C_s	Smagorinsky coefficient
d_p	Particle diameter
e	Coefficient of restitution
$\boldsymbol{F}$	Force
f	Drag factor, or friction coefficient
f_N	Number frequency distribution
f_c	Maxwellian distribution
$\boldsymbol{G}$	Relative velocity
G_{pp}	Powder Modulus
G_{pf}	Frictional pressure Modulus
$\boldsymbol{g}$	Gravitational acceleration
g_0	Radial distribution
I_{φ}	Indicator step function for phase φ
I	Measured light intensity
$\boldsymbol{I}$	Light intensity matrix, or identity matrix
$\boldsymbol{J}$	Impulsive force
J_{vis}	Granular temperature dissipation due to fluid viscosity
J_{slip}	Granular temperature production due to fluid turbulence
K_d	Momentum transfer coefficient, drag
k	Turbulent kinetic energy
l	A characteristic length
m	Mass
$\boldsymbol{n}$	Surface normal unit vector
p	Pressure
P_s	Solids pressure
P_f	Frictional solids pressure
P_{kt}	Kinetic solids pressure
$\mathbf{q}_{\Theta}$	Granular temperature flux
$\boldsymbol{R}$	Correlation matrix
Re_l	Reynolds number with characteristic length l
$\boldsymbol{S}$	Rate of deformation tensor
$\mathbf{S}_{\mathrm{f}}$	Cell face surface area vector

St	Stokes Number
$\boldsymbol{u}_{\varphi}$	Velocity of phase φ
$\boldsymbol{u}_{r}$	Relative velocity
$\boldsymbol{u}_{c}$	Mixture velocity
V	Volume
v_0	Critical velocity, speed of wave propagation

Greek symbols

α_{φ}	Phase volume fraction of phase φ
$\alpha_{s,max}$	Maximum particle volume fraction
β	Momentum transfer coefficient, drag
γ_s	Granular temperature dissipation due to inelastic collisions
Δ	SGS-filter size
Δ_{x}	Image scale
ε	Dissipation of turbulent kinetic energy, or a small tolerance
ϵ	Residual
μ	Dynamic viscosity
ν	Kinematic viscosity
σ	Statistical standard deviation
σ^2	Statistical variance
σ_N	Surface normal stress
ρ	Density
Θ	Granular temperature
κ_s	Granular temperature conductivity
λ_s	Solids bulk viscosity
$\boldsymbol{\tau}$	Deviatoric stress tensor
$\boldsymbol{\tau}_{Re}$	Reynolds stress tensor
$\boldsymbol{\tau}_{r}$	Residual stress tensor
$\boldsymbol{\tau}_{SGS}$	SGS-stress tensor
τ_c	Time-scale of continuous phase turbulent eddies
τ_V	Particle relaxation time
τ_s	Time-scale of the system
τ_K	Kolmogorov time-scale
φ_f	Angle of internal friction
ϕ	Volume flux
ϕ_o	Sphericity
ϕ_{spec}	Specularity coefficient

Subscripts, superscripts and oversymbols

$\boldsymbol{Q}$ is a scalar, vector, tensor or matrix variable.

$\boldsymbol{Q}_{\varphi}$	Value of Q in phase φ
$\boldsymbol{Q}_{s}$	Value of Q in solids phase
$\boldsymbol{Q}_{g}$	Value of Q in gas phase
$\boldsymbol{Q}_{t}$	Turbulent
$\boldsymbol{Q}^{T}$	Transpose
$\boldsymbol{Q}'$	Fluctuation with respect to average
$\boldsymbol{Q}''$	Fluctuation with respect to density weighted average
$\boldsymbol{Q}^{*}$	Modified or corrected
$\dot{\boldsymbol{Q}}$	Rate of change
$\overline{\boldsymbol{Q}}$	Average
$\overline{\boldsymbol{Q}}_{\boldsymbol{\varphi}}$	Conditional average
$\widetilde{\boldsymbol{Q}}$	Density weighted average
$\widetilde{\boldsymbol{Q}}_{\varphi}$	Density weighted conditional average

1. INTRODUCTION

An efficient and environmentally friendly energy source is vital for a modern society. Although there is a strong push for development of alternative energy sources – such as wind and solar power – today, and in future decades different kinds of combustion processes are responsible for the majority of global energy production. The increasing pressure towards non-fossil fuels adds to the challenges of combustion related research and the design of reactors: the properties of such fuels differ from traditional fuels, and their quality is more varied.

The introduction of fluidized particles to the combustor has advantages over traditional combustors. Firstly, fluidized bed combustors are less sensitive to the choice of fuel, and secondly, the nitrous and sulphur oxide emissions can be reduced. Mixing is greatly enhanced by the presence of the particle phase, allowing combustion at lower temperatures, while the improved mixing, together with the heat capacity of the particles, smoothes out the temperature field. In addition, emission absorbent particles may be inserted directly into the reactor. Fluidized beds are also used in other types of chemical processes, such as catalytic cracking in oil refining, where it enhances mixing and provides a large surface area contact between the phases.

Even if chemical reactions and heat transfer are ignored, the physics of the multiphase flow in fluidized beds is very complex. In current practice, fluidized beds are always simulated with time dependent, transient simulations with reasonably fine computational meshes to capture the complicated physical phenomena. In industrial applications the fluidized beds are large and their size, together with long averaging times necessitated by the unsteady nature of the flow leads to unfeasibly large computational costs. These computational costs have created the demand for an efficient, time-averaged simulation method that could be used as a design tool in industry.

The aim of this thesis is to provide detailed experimental data about the dynamics of the particle phase in a pilot scale Circulating Fluidized Bed (CFB) by applying image-based measurement methods. Such data is needed for the validation and model parameter definition of transient and time-averaged simulations. In addition, a feasibility study has been carried out on the use of an OpenFOAM based Eulerian two-phase solver for transient simulations of a CFB, together with parallelization to offset the computational cost of the time-dependent simulations.

2. FLUIDIZATION AND GAS-SOLID FLOW

This chapter introduces the physical phenomena of fluidization and gas-solid flow to give the reader adequate background information for the later chapters. Much of the detailed analysis is omitted. More information on fluidization can be found in books by Kunii and Levenspiel (1991), Gidaspow (1994) and Grace et al. (1997) among others, and on general particle-fluid flow in books by Crowe et al. (1998) and Michaelides (2006).

A basic example of a fluidized bed is a vertical pipe partially filled with spherical particles as shown in Figure 2.1. A porous distributor plate which allows the fluid pumped from below to flow through it while stopping the particles is located at the bottom of the pipe. For good quality fluidization the distributor plate should produce a sufficient pressure drop, for the incoming fluid flow to be distributed evenly across the bottom of the pipe. (Gidaspow, 1994, p. 97.)

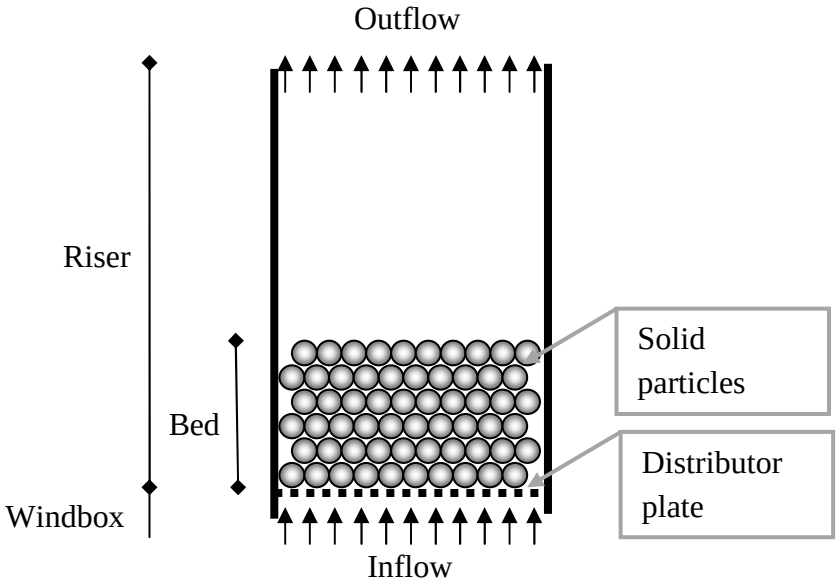

Figure 2.1. S*chematic of a basic fluidized bed*

The gas or liquid flow upward through the particle bed causes a pressure drop. As the inlet gas or liquid mean velocity, i.e. fluidization velocity is increased the pressure drop increases until it is great enough to support the weight of the particles. At this point the pressure drop stabilises and the particles begin to move. This point is called the

minimum fluidization state and the corresponding mean inlet velocity the *minimum fluidization velocity*. (Gidaspow, 1994, p. 97.)

If the wall friction and the friction between the particles is ignored, the balance between the pressure drop and the buoyancy can be written as

$$(1-\alpha_g)(\rho_s-\rho_g)g = \frac{\beta}{\alpha_g}(u_g-u_s) \tag{2.1}$$

In a dense bed β is obtained from the Ergun (1952) Equation (2.2).

$$\beta = 150\frac{(1-\alpha_g)^2\mu_g}{\alpha_g(d_p\phi)^2} + 1.75\frac{\rho_g|\boldsymbol{u}_g-\boldsymbol{u}_s|(1-\alpha_g)}{d_p\phi_o} \tag{2.2}$$

α_g is the gas volume fraction, ρ_s and ρ_g solid and gas densities respectively, g the gravitational acceleration, and u_g and u_s the respective gas and solid velocities. μ_g is the gas viscosity, d_p the particle diameter and the particle sphericity is ϕ_o, Equation 2.3. (Gidaspow, 1994, pp.100-101.)

$$\phi_o = \frac{\pi^{1/3}(6V_p)^{2/3}}{A_p} \tag{2.3}$$

Sphericity is defined as the ratio of the surface area of a sphere with the same volume as the particle, V_p and the surface area of the particle, A_p.

Geldart (1973) suggested classification of uniform size powders into four groups based on their behaviour in a fluidized bed. The classification is valid for air fluidized beds in ambient conditions. The parameters used for the classification are the density difference between the particles and air, and the mean size of the particles. Geldart's diagram is shown in Figure 2.2. (Gidaspow, 1994, p. 105.)

The particles used in the circulating fluidized bed examined in this thesis belong to group B (bubbling). These particles are characterized by a mean diameter of between 40 μm and 500 μm and a density from 1400 kg/m^3 to 4000 kg/m^3. These powders start bubbling at the minimum fluidization velocity and the expansion of the bed is small at atmospheric pressure. With a steady fluidization velocity, the rise velocity of the bubbles is lower than the velocity of the gas inlet jet. (Gidaspow, 1994, p. 105.)

The other groups are: small or low density particles, group A (Aerated), large and very dense particles, group D, and particles that are difficult to fluidize, group C (Cohesive), because of their tendency to lift as a plug, rat-hole and agglomerate on the furnace

walls. For group C particles the inter-particle forces are larger than the forces exerted by the fluid on the particles. (Gidaspow, 1994, p. 105.)

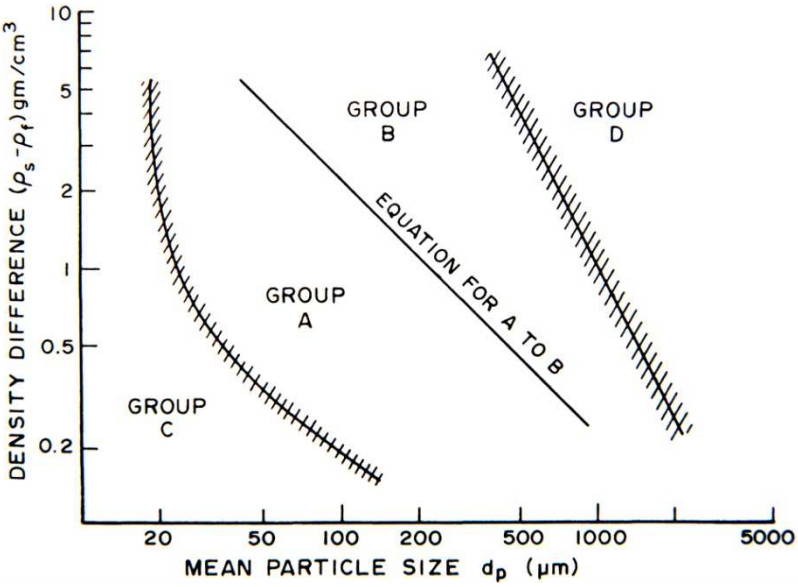

Figure 2.2. *Geldart's classification of fluidized particles (Gidaspow, 1994, p. 103.)*

Fluidization has distinct flow regimes which are visualized in Figure 2.3. At the *minimum fluidization state*, the particles lie at the bottom of the pipe in fully packed state and reorganize according to the minimum energy principle. With Geldart class B particles bubbles begin to appear as the fluidization velocity is increased and the system enters the *bubbling* regime. If the riser is narrow and the bed is sufficiently tall, the bubbles will coalesce and form slugs that cover almost the whole cross-section of the riser. This is called the *slugging* regime. (Gidaspow, 1994. p. 97.)

At even higher velocities the bubble and slug structures break and the bed becomes *turbulent*. In a turbulent bed, dilute and dense areas alternate rapidly and neither state dominates the behaviour. The pressure fluctuations reach their highest standard deviation values in the turbulent regime (Grace and Bi, 1997). Above the turbulent region is the *fast fluidization* regime. Li and Kwauk (1980) and Takeuchi et al. (1986) defined fast fluidization as a state where dilute and dense areas coexist. Horio (1991, 1997) added that the bed is in the fast fluidization state, if the superficial gas velocity is higher than the transport velocity, even if the system doesn't have dilute areas. Fast fluidization systems often have dense regions on the walls moving downwards, while the main part of the suspension, mostly dilute, moves upwards in the middle. With a further increase in fluidization velocity the system moves into the *pneumatic conveying* regime, which is characterized by the disappearance of dense regions and by a vertically uniform particle distribution. (Passalacqua, 2008, p. xii.)

In fast fluidization and pneumatic conveying regimes, with fluidization velocities above the terminal velocity of the particles, some particles are blown out of the riser. The continuous operation of such a system requires an inflow of particles into the system. In a Circulating Fluidized Bed (CFB) the particles are separated, most commonly with a cyclone, from the gas outflow and returned to the bottom of the bed. (Gidaspow, 1994. pp. 97-98.) CFBs usually operate in the fast fluidization regime, as was the case with the CFB examined in this thesis.

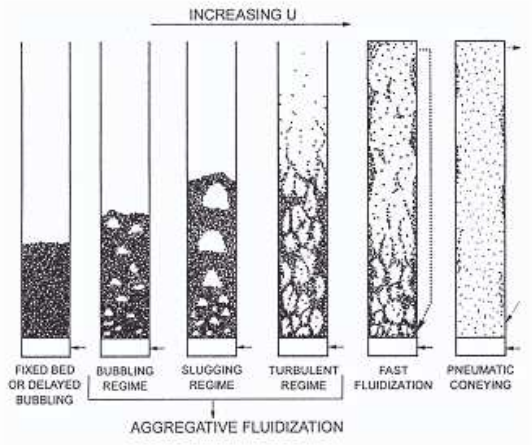

Figure 2.3. *Flow regimes of a fluidized bed in Grace et al. (1997) according to Passalacqua (2008, p. xi).*

2.1. Fluid-particle interaction

The study of the interaction between a solid sphere and a fluid flow has a long history. The first pioneers in the field were Sir Isaac Newton (1642-1727) and Jean le Rond d'Alembert (1717-1783). During the intervening centuries of study several mechanisms of momentum transfer between the sphere and the fluid have been identified. The most intuitive, and often the most important, of these is the steady-state drag force, which is the force felt while holding a beach ball in a steady breeze. The drag force affecting a solid, spherical particle can be quantified with Equation 2.4, where $\boldsymbol{F}_D$ is the drag force vector affecting the particle. $\boldsymbol{u}_g$ and $\boldsymbol{u}_s$ are velocity vectors for the fluid and the particle. ρ_g is the density of the flowing, continuous medium and A is the frontal area of the particle. As the particle is spherical the frontal area A is $\frac{\pi}{4}d_p^2$, where d_p is the diameter of the particle.

$$\boldsymbol{F}_D = \frac{1}{2}\rho_g C_D A\left|\boldsymbol{u}_s - \boldsymbol{u}_g\right|\left(\boldsymbol{u}_s - \boldsymbol{u}_g\right) \tag{2.4}$$

Drag coefficients, C_D, have been defined for bodies of various shapes with analytical, experimental and numerical methods. The commonly accepted drag coefficient of a sphere in a steady, uniform flow is described by the *standard drag curve*, Figure 2.4, as a function of the Reynolds number, Equation 2.5, based on the diameter of the sphere, d_p. $|u|$ is the magnitude of (relative) velocity of mean flow and $\nu = \mu/\rho$ is kinematic viscosity of the flowing medium.

$$Re_d = \frac{|\boldsymbol{u}| d_p}{\nu} \tag{2.5}$$

The Reynolds number describes the ratio of viscous and convective effects in the flow. At a low Reynolds number, drag is caused solely by the friction between fluid and the surface of the sphere. This is called *Stokes drag* and it is valid for $Re_d < 1$. As the Reynolds number increases the flow begins to detach from the surface and an increasing proportion of the drag is caused by the low pressure in the detached wake of the sphere. This is known as pressure or shape drag. Above Reynolds number 10^3 practically all of the drag is pressure drag. At the critical Reynolds number, $\sim 5 \times 10^5$ the boundary layer on the sphere becomes turbulent and the flow reattaches as a result of increased mixing, i.e. apparent increase in viscosity, due to the turbulent eddies. The drag coefficient drops sharply as the transition from laminar to turbulent boundary layer occurs due to reduced pressure drag.

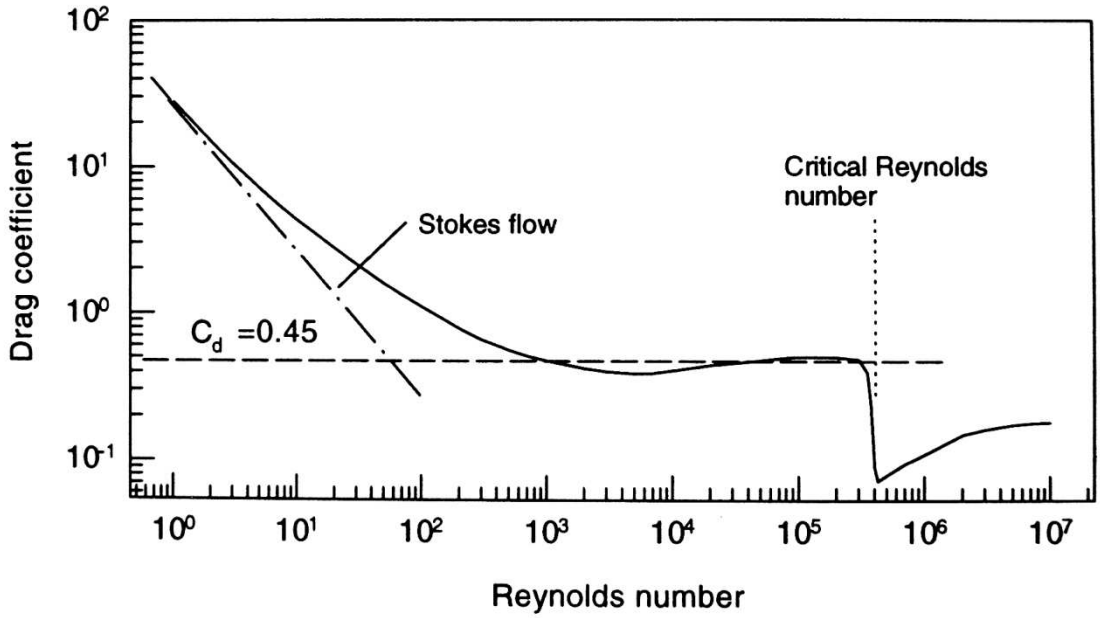

Figure 2.4. *Drag coefficient of a sphere by Reynolds number. (Crowe et al., 1998, p. 68.)*

If the flow experienced by the sphere is not uniform an additional *Faxen force* (Happel and Brenner, 1973) is created. The ratio between Faxen force and Stokes drag is

proportional to $\left(d_p/l\right)^2$, where l is the characteristic length related to the flow field curvature. In a laminar flow through a bent pipe the curvature would be the radius of the bend. In a turbulent flow the characteristic curvature can also be the scale of turbulent eddies. At higher Reynolds numbers the Stokes drag represents increasingly small proportion of the drag, reducing the effect of the Faxen force relative to the uniform flow drag. (Crowe et al., 1998, p. 69.)

$$\frac{|\boldsymbol{F}_{Faxen}|}{|\boldsymbol{F}_{Stokes}|} \sim \left(\frac{d_p}{l}\right)^2 \tag{2.6}$$

Gravity creates a pressure gradient in the fluid that creates a force in a direction opposed to the gravity on the particle which is equal to the weight of the fluid displaced by the particle. The gravity also affects the particle, creating a force equal to the weight of the particle in the direction of the gravity. The net buoyant force from combining these two forces can be described with Equation 2.7, where $\boldsymbol{g}$ is the gravitational acceleration, V_s the volume of the particle and ρ_s and ρ_g are the particle and fluid densities respectively.

$$\boldsymbol{F} = \boldsymbol{g}V_s(\rho_s - \rho_g) \tag{2.7}$$

The equation for the motion of a particle including drag and buoyancy effects is

$$m\frac{d\boldsymbol{u}_s}{dt} = 3\pi\mu_g d_p f\left(\boldsymbol{u}_g - \boldsymbol{u}_s\right) + m\boldsymbol{g} - \rho_g \boldsymbol{g} V_s \tag{2.8}$$

or

$$\frac{d\boldsymbol{u}_s}{dt} = \frac{f}{\tau_V}\left(\boldsymbol{u}_g - \boldsymbol{u}_s\right) + \boldsymbol{g}\left(1 - \frac{\rho_g}{\rho_s}\right) \tag{2.9}$$

$$f = \frac{C_D}{C_{D_{Stokes}}} = \frac{C_D Re_r}{24} \tag{2.10}$$

$$\tau_V = \frac{\rho_s d_p^2}{18\mu_c} \tag{2.11}$$

Where f is the drag factor describing the ratio of drag coefficient to Stokes drag and τ_V is the particle relaxation time. The particle relaxation time describes a characteristic time scale it takes for the particle to react to changes in the surrounding flow. If the density ratio ρ_g/ρ_s is small, as it is in the case of a CFB combustor, the equation for motion can be approximated with Equation 2.12. (Crowe et al., 1998, p. 77.)

$$\frac{d\boldsymbol{v}}{dt} = \frac{f}{\tau_V}(\boldsymbol{u}_g - \boldsymbol{u}_s) + \boldsymbol{g} \tag{2.12}$$

Unsteady flow creates additional forces that affect the particles. Virtual or apparent mass force represents the force needed to accelerate the fluid surrounding the particle, as the velocity of the particle changes relative to the fluid. Another force is the Basset, or "history", force. This force is caused by temporal development of the boundary layer surrounding the particle as the velocity of the particle changes. (Crowe et al., 1998, pp. 81-86.) Vojir and Michaelides (1994) and Liang and Michaelides (1992) showed that the Basset force is negligible for gas-particle flows if $\rho_g/\rho_s < 0.002$ and $d_p > 1$ μm (Enwald et al. 1996, p. 45). Including the Basset and virtual mass terms in the equation of motion with Stokes drag for a particle, we get the Basset-Boussinesq-Oseen (BBO) equation which can be written as Equation 2.13. If the density ratio ρ_g/ρ_s is small the Equation 2.13 simplifies to Equation 2.12 with $f = 1$. (Crowe et al., 1998, pp. 86-87.)

$$\begin{aligned}\left(1 - \tfrac{1}{2}\frac{\rho_g}{\rho_s}\right)\frac{d\boldsymbol{u}_s}{dt} &= \frac{1}{\tau_V}(\boldsymbol{u}_g - \boldsymbol{u}_s) + \tfrac{3}{2}\frac{\rho_g}{\rho_s}\dot{\boldsymbol{u}} + g\left(1 - \frac{\rho_g}{\rho_s}\right) \\ &+ \sqrt{\frac{\boldsymbol{9}}{\boldsymbol{2\pi}}}\left(\frac{\rho_g}{\rho_s}\right)^{\frac{1}{2}}\frac{1}{\sqrt{\tau_V}}\left[\int_0^t \frac{\dot{\boldsymbol{u}}_g - \dot{\boldsymbol{u}}_s}{\sqrt{t-t'}}\,dt' + \frac{(\boldsymbol{u}_g - \boldsymbol{u}_s)_{\boldsymbol{0}}}{\sqrt{\tau_V}}\right]\end{aligned} \tag{2.13}$$

Rotation of the particle causes a lift force. Rotation can be caused by interaction with walls, other particles, or by a velocity gradient in the flow. The pressure force created by the velocity gradient induced rotation is called the Saffman lift force. The lift caused by particle rotation imposed by other sources is called the Magnus force. (Crowe et al., 1998, pp. 95-99.) Similarly to virtual mass force, the Saffman and Magnus forces are proportional to the density ratio when included in the BBO-equation, and can be considered insignificant if the density ratio is small.

The effect of continuous phase turbulence on particle movement depends on the time and length scales of the turbulent flow and the particle relaxation time, Equation 2.11, as well as size. The Stokes number, Equation 2.14, is the ratio between the particle relaxation time and the characteristic time scale of the surrounding flow, Equation 2.15, where L_s and U_s are the characteristic length and velocity of the flow respectively. If the Stokes number is small, $St \ll 1$, the particles follow turbulent velocity fluctuations obediently. If the Stokes number is large, $St \gg 1$, the continuous phase turbulence has little effect on the particle movement.

$$St = \frac{\tau_V}{\tau_s} \tag{2.14}$$

$$\tau_s = \frac{L_s}{U_s} \tag{2.15}$$

Continuous phase turbulence tends to increase the drag coefficient of a sphere at sub critical Reynolds numbers and lower the critical point, but there's a lot of variation in the results presented in literature (Crowe et al., 1998, pp. 88-91). The presence of particles also affects the turbulence in the continuous phase. This is often called *modulation of turbulence*. Michaelides (2006, p. 233) lists six mechanisms for turbulence modulation due to the presence of a discrete phase, which are applicable to solid particles:

a) Vortex breaking and dissipation of turbulent kinetic energy on the surface of the immersed objects.
b) Modification of the effective viscosity of the fluid.
c) Eddy energy dissipated on the acceleration and deceleration of the elements of the dispersed phase.
d) Wakes and shedding of vortices behind the immersed objects.
e) Fluid moving with the immersed objects or being displaced by them.
f) Enhancement of fluid velocity gradients between two neighbouring immersed objects.

The first three mechanisms increase the dissipation and last three the production of the turbulent kinetic energy. Peirano and Leckner (1998, p. 264) state that b) and f) may not be significant in dilute suspensions.

According to Peirano and Leckner (1998, p. 263), Elgobashi (1991) classified the coupling between the particles and the turbulence of the surrounding flow into three categories based on the volume fraction of the particles or the relative distance between the particles, and the ratio of the flow and particle time scales. Figure 2.5 is a diagram of this classification. Here τ_c , Equation 2.16, is the characteristic time scale of the turbulent eddies in the continuous phase according to the commonly used *k*-ε turbulence model, and τ_K is the Kolmogorov time scale, Equation 2.17, that describes the smallest timescales of turbulence in the continuous phase. The kinetic energy of the turbulence is k and ε is the dissipation of the turbulent energy. The third timescale in the diagram, τ_V, is the particle relaxation time described above. (Peirano and Leckner,1998, p. 263-264.)

$$\tau_c = C_\mu \frac{k}{\varepsilon},\ C_\mu = 0.09 \tag{2.16}$$

$$\tau_K = \left(\frac{\upsilon}{\varepsilon}\right)^{\frac{1}{2}} \tag{2.17}$$

With a very low particle phase volume fraction, the inertia of the discrete phase is low and has little effect on the turbulence of the carrying fluid. This is called a "one-way coupling" by Elgobashi (1991). As the volume fraction of the particles increases to around 10^{-6}, the discrete phase begins to modulate the turbulence through the six

mechanism listed earlier, creating a “two-way coupling” between the phases. With high Stokes numbers the particles enhance the turbulence and at low Stokes numbers the dissipation is enhanced. The region of increasingly dense suspension, $\alpha_s > 10^{-3}$, where the collisions between the particles become important is characterized by “four-way coupling” with increasing complexity. (Peirano and Leckner, 1998, p. 264.) The part of the diagram that describes the area of interest in conventional chemical engineering applications is shaded (Passalacqua, 2008, p. 45). According to Peirano and Leckner (1998, p. 282.) the effects of particle presence on dissipation and production of turbulence are governed by redistribution of the turbulent kinetic energy spectrum, rather than uniform mechanisms over the whole spectrum.

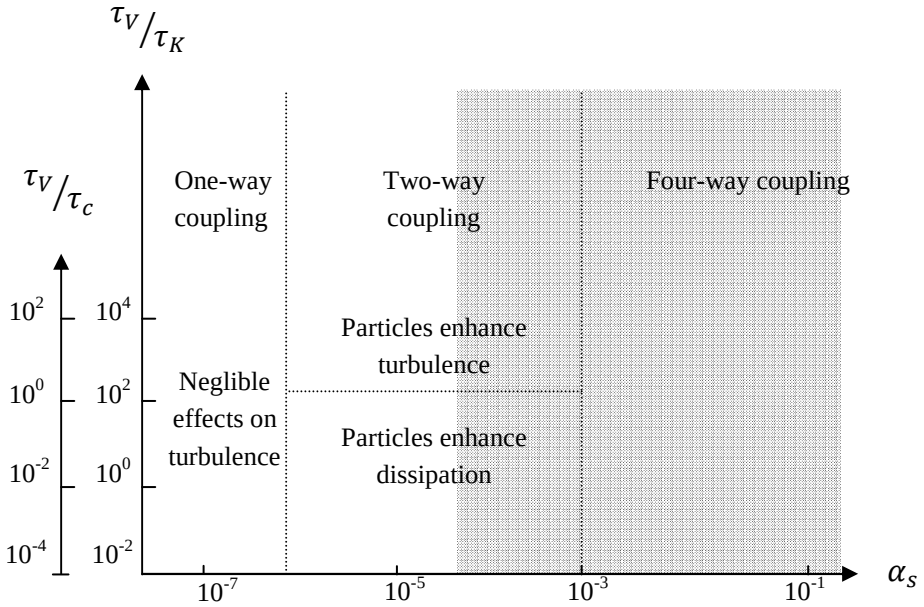

Figure 2.5. *Elgobashi’s (1991) classification of particle-turbulence coupling according to Peirano and Leckner (1998*, p. 263*).*

Tsuji et al. (1984) conducted experiments with a dilute vertical pipe flow with particles in isotropic turbulence and found that small particles, 200 μm, reduced turbulence intensity everywhere, while large particles, 3 mm, increased it. With medium sized particles, 500 μm and 1000 μm –the smaller of which is similar in size to the particles used in the pilot scale CFB studied in this thesis – increased the intensity of turbulence in the core section of the pipe but reduced it near the walls. These results have been theoretically predicted by Derevich (1988) since then. (Peirano and Leckner 1998, pp. 281-282.)

In a gas-solid flow, with particle volume fractions such as are found in a CFB, the presence of other nearby particles affects the fluid forces exerted on a particle. The development of drag models for particle clouds is challenging. Analytical modelling is difficult as all of the particles’ contribution to flow has to be considered, and flow

measurements inside a particle cloud are often obstructed by the particle cloud itself. Ergun (1952) conducted a classic study of flow through a packed particle bed which resulted in Equation 2.2 mentioned above. The correlation is valid for a packed bed up to minimum fluidization, but Gidaspow (1994) suggested that it works quite well as long as the particle volume fraction is more that $\alpha_s > 0.2$ and as such it should be used in dense regions. (Crowe et al., 1998, pp. 78-79.)

Wen and Yu (1966) correlated both their own and Richardson and Zaki's (1954) fluidization experiments with Equation 2.18, where $f_0$is the single particle drag factor. For $g(\alpha_g)$ they suggested Equation 2.19, which approaches single particle drag as the particle volume fraction approaches zero. (Crowe et al., 1998, p. 80.)

$$\boldsymbol{F}_D = g(\alpha_g) 3\pi\mu_g d_p f_0(\boldsymbol{u} - \boldsymbol{v}) \tag{2.18}$$

$$g(\alpha_g) = \alpha_g{}^{-3.7} \tag{2.19}$$

In fluidized bed simulations, a combination of Ergun (1952) and Wen-Yu (1966) drag models as suggested by Gidaspow (1994, p. 315) is often used, the Ergun model being used when local particle volume fraction is above $\alpha_s > 0.2$ and the Wen-Yu in other cases.

2.2. Particle-Particle Interaction

At low particle phase volume fractions the probability of particle-particle collisions is low and such rare collisions can be ignored in calculations. However in many applications, such as fluidized beds, particle concentrations are so high that the particle-particle interaction has to be accounted for. Often two basic approaches are commonly used to model particle collisions, the hard-sphere and soft-sphere models. The hard sphere model is written as integral equations and ignores particle deformation, while the soft-sphere model is written as a differential equation and uses an overlapping displacement variable to describe the deformation. Both models assume that the Coulomb friction law is valid for sliding particles and once sliding stops the particles won't slide any more. (Crowe et al., 1998, pp.128-135.)

For a basic example of a particle-particle collision, let's consider a collision of two spherical, inelastic particles as described in Figure 2.6. The colliding particles 1 and 2 have initial translational velocities $\mathbf{u}_1$ and $\mathbf{u}_2$, as well as rotational velocities $\boldsymbol{\omega}_1$ and $\boldsymbol{\omega}_2$ respectively. According to the hard-sphere model the momentum transfer between the particles occurs at contact point and can be described by writing impulsive force, **J**, balance for the particles. The impulsive force can be divided into two components:

tangential and normal to the surfaces of the sphere. From this balance it is possible to calculate the translational and rotational velocities after the collision, if the coefficients of friction, f, and restitution, e, are known for the collision. (Crowe et al., 1998, pp.128-135.)

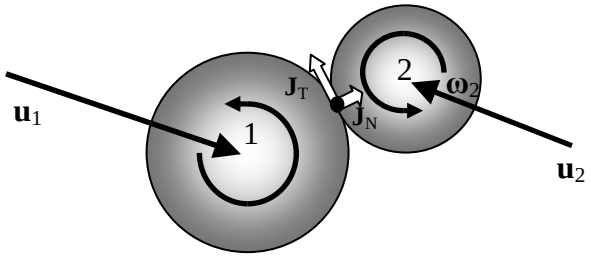

Figure 2.6. *Diagram of a collision between two spherical particles.*

The coefficient of restitution, Equation 2.20, is defined as the ratio of the pre- and post-collisional relative velocities, $\boldsymbol{G_0}$ and $\boldsymbol{G}$ respectively, inner product with the particle surface normal unit vector, $\boldsymbol{n}$, i.e. it describes the loss of translational momentum in the collision and elasticity of the particles. Depending on collisional velocities and the coefficients of friction and restitution, the particles either continue or stop sliding relative to each other during the collision, resulting in two different solutions for the post-collisional velocities. (Crowe et al., 1998, pp. 130-131.)

$$e = -\frac{\boldsymbol{n}\cdot\boldsymbol{G}}{\boldsymbol{n}\cdot\boldsymbol{G_0}} \tag{2.20}$$

In the soft-sphere model the collision is modelled as a system of springs and dampers. The model requires definitions for the coefficient of friction, the stiffness and the damping coefficient. The friction can be measured, the stiffness determined from material properties and the damping coefficient can be derived from the stiffness. However these stiffness values can rarely be used in numerical simulation because of short time steps demanded by the natural oscillation periods of the particles. For this reason, a conveniently small stiffness and a damping coefficient derived by relating it to the coefficient of restitution are often used to facilitate the numerics. (Crowe et al., 1998, pp.136-138.)

The same modelling approaches can be applied to particle-wall collisions. It should be remembered, that in real life applications particles are rarely perfectly spherical, and this has a significant effect on the post-collisional velocities. Shen et al. (1989) calculated trajectories for a particle with a sphericity of 1.043 in a two dimensional channel and demonstrated that even such a nearly spherical particle has a significantly irregular trajectory. (Crowe et al., 1998, pp. 123-124.)

3. 2D PILOT-SCALE CFB

A pilot-scale CFB has been built at Åbo Akademi University. The design and construction of the CFB is presented in detail in Matias Guldén's Master of Science thesis (2008). The device has also been described by Kallio et al. (2009a, 2009b). The objective was to create a reasonably large but relatively two-dimensional fluidized bed. Reasonably large to facilitate the scaling of the results to industrial scale and two-dimensional to allow quick simulation and image based velocity and volume fraction measurements.

The riser section of the CFB is 3.0 m high and 0.4 m wide. The distance between the front and back walls of the riser is 0.015 m. The wall material is clear, 10 mm thick, hardened polycarbonate. The fluidization air is injected from eight equally spaced 0.013 x 0.013 m injectors at the bottom of the bed. For adequate pressure loss in the injectors, 4 mm diameter restrictors are placed below the injector nozzles. The device has been designed for fluidization velocities of up to 4.0 m/s. Instead of a cyclone the CFB has a simple separator to separate the particles from the gas outflow. A schematic and pictures of the CFB are shown in Figure 3.1.

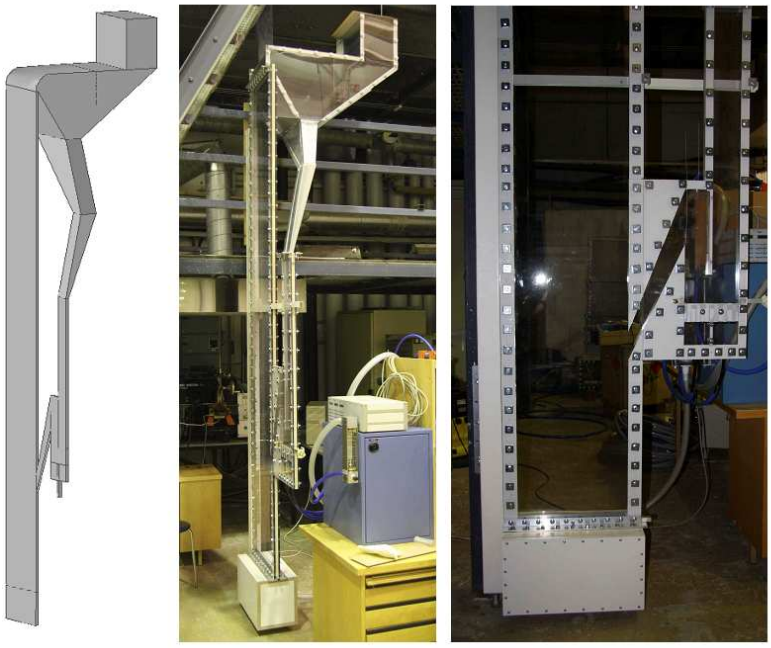

Figure 3.1. *A schematic and pictures of the 2D pilot scale CFB and the lower portion with the windbox and the loop seal. Picture Matias Guldén (2008).*

To eliminate static electricity, water was injected into the fluidization air so that a relative humidity of 40-50% was maintained at the gas outlet. To further reduce the static electricity a dose of 0.08%$_{mass}$ of Larostat 519 antistatic powder was mixed with the particles.

Approximately 3.8 kg of spherical glass particles with a density of 2480 kg were used as the bed material. With the fluidization velocities used, 3.25 m/s and 3.75 m/s, the riser section of the CFB had 3.2 and 3.1 kg of the particles respectively. They were sieved and the diameter distribution was measured from a sample of 11443 particles with shadowgraphy, as shown in Figure 3.2. Particle detection was carried out using the two-step algorithm described in chapter 6.3. Only particles with an aspect ratio smaller than 1.3 were included in the results. The bed material also includes a minor portion of deformed, non-spherical particles. The diameter was defined as the diameter of circle with equivalent projected area. The sauter mean diameter of the particles is 442 μm. The terminal velocity of such a particle is 3.125 m/s with a Reynolds number of 88, and it belongs in Geldart's group B (Figure 2.3). The bulk density of the packed particle bed is 1554 kg and thus maximum volume fraction of the particles is 0.625.

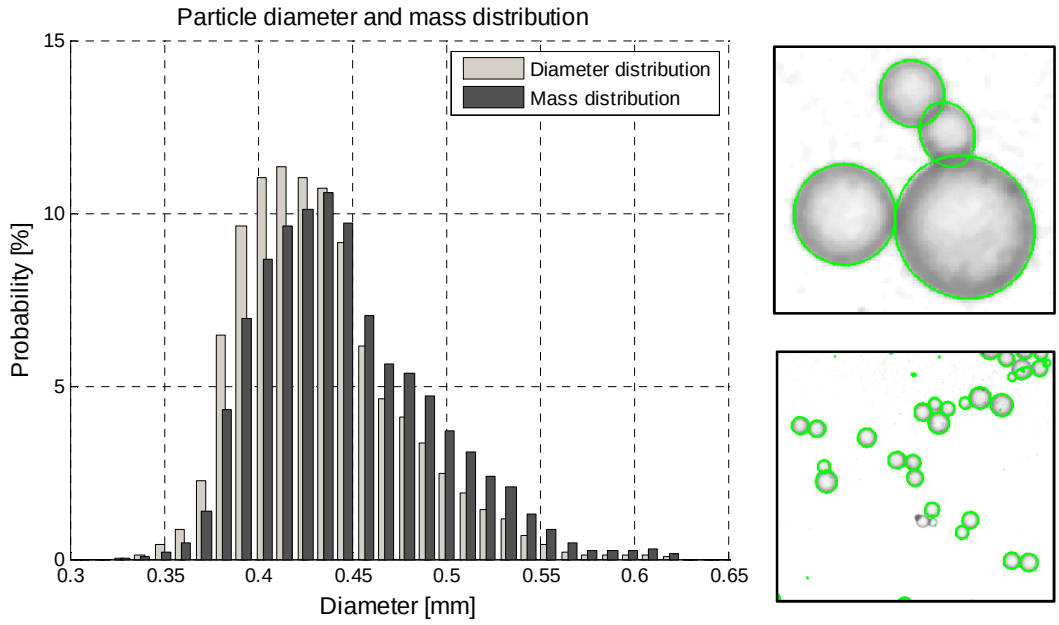

Figure 3.2. *A sample of the particles used and their diameter distribution as measured with shadowgraphy.*

4. EULERIAN CFD MODELLING OF CFB

Computational Fluid Dynamics (CFD) means modelling fluid flow using computers to numerically solve the equations that describe the flow. The equations are based on principles of mass, momentum and energy conservation. In CFD, they are usually based on the classic Navier-Stokes equations that are believed to describe any single-phase flow. The equations are the work of Claude-Louis Navier (1785-1836) and Sir George Stokes (1819-1903).

In principle, it is possible to solve these equations directly provided there is enough spatial and time resolution. In practice, with the current computers, this is impossible in most practical applications and the equations have to be simplified. Common practices for simplification are leaving out less important terms and averaging the equation in time and space. The averaging creates additional fluctuation terms that require modelling. In single phase flows these are called Reynolds Stresses while the averaged equations are called Reynolds Averaged Navier-Stokes (RANS) equations. They are named after Osborne Reynolds (1842-1912) who proposed the method.

There are two main approaches to the numerical simulation of fluid-particle flows: Lagrangian and Eulerian. In the Lagrangian approach each individual particle is tracked and its interaction with fluid, walls and other particles is modelled with the single particle models described in chapter 2, or similar. The fluid phase is modelled in the same way as the single phase flows, but with the addition of fluid-particle interactions. The advantages of the Lagrangian approach are that the interactions of a single particle are relatively well known and have good mathematical formulations, and that the effects of particle history can be included. The commonly used Lagrangian multiphase models are, however, only valid at low particle volume fractions and as such are not applicable to fluidization.

The Lagrangian model that is suitable for dense applications, such as fluidization, is called the *Discrete Element Method* (DEM, see e.g. Tsuji, 2007). Here the computational particle trajectories are calculated and single particle models are used for the particle interactions, including particle-particle interaction. The problem with the model is that in dense flows the number of particles is necessarily high, and thus the number of equations and computational costs are correspondingly high. Another reason for the high computational cost is the short time step required by the soft-sphere collision model. Currently, DEM models are not usable for industrial scale applications

although they have been applied to small risers. Zhang et al. (2008) used a periodic computational domain to simulate a long riser with a small computational domain.

In the Eulerian approach, the particle phase is also modelled as a fluid and the equations describe the local average properties of the flow and particle clouds. The major advantage of the method is that the number of equations only depends on the number of phases, instead of the number of particles as in the Lagrangian approach. Additionally, the forms of the equations are similar to those used in single-fluid simulation, thereby easing the implementation of the method as a lot of the existing framework can be utilized. The disadvantages are that in reality the particles don't always behave like a fluid and modelling of the particle cloud interactions is challenging. Complex statistical models such as the *Kinetic Theory for Granular Flow* (KTGF, see e.g. Gidaspow, 1994) are often used to describe the particle-particle interaction. The Euler-Euler method is currently the standard method for simulation of fluidized beds.

The following Sections 4.2-4.5 present incompressible Eulerian equations for the simulation of fluidized beds and common closure models used in this thesis. Section 4.1 takes a look into the averaging procedure on which the two-fluid method is based.

4.1. Conditional averaging and the Euler-Euler approach

This section is based on and uses similar notation to Weller's (2005) report, where he describes the algorithm employed in the OpenFOAM based Euler-Euler two-phase CFD solver. A description of averaging procedures can also be found in Enwald et al. (1996, pp. 26-31) and Crowe et al. (1998, Appendix B).

To derive the equations for the Euler-Euler (two-fluid) method, the instantaneous momentum, mass and energy balance equations are conditionally averaged by first multiplying them with the indicator step function, $I_\varphi(\boldsymbol{r},t)$. The indicator function is one in phase φ and zero otherwise. Ensemble averaging is then applied to the equations.

The volume fraction for phase φ, $\alpha_\varphi(\boldsymbol{r},t)$, is defined as the ensemble average of $I_\varphi(\boldsymbol{r},t)$ i.e. the probability of finding phase φ at point $(\boldsymbol{r},t)$.

$$\alpha_\varphi = \bar{I}_\varphi(\boldsymbol{r},t) \tag{4.1}$$

The ensemble average is denoted here with an overbar. For any fluid property $\boldsymbol{Q}(\boldsymbol{r},t)$, be it scalar, vector or tensor, the conditional ensemble average, $\overline{\boldsymbol{Q}}_\varphi$, is defined as

$$\overline{I_\varphi \boldsymbol{Q}} = \alpha_\varphi \overline{\boldsymbol{Q}}_\varphi \, . \tag{4.2}$$

The conditional density weighted average i.e. Favre-average, $\widetilde{\boldsymbol{Q}}_\varphi$ is defined as

$$\overline{I_\varphi \rho \boldsymbol{Q}} = \alpha_\varphi \bar{\rho}_\varphi \widetilde{\boldsymbol{Q}}_\varphi . \tag{4.3}$$

With fluctuations around the $\widetilde{\boldsymbol{Q}}_\varphi$ are defined as

$$\boldsymbol{Q}''_\varphi \equiv \boldsymbol{Q} - \widetilde{\boldsymbol{Q}}_\varphi \, . \tag{4.4}$$

Then, the conditional average of the product of two fluid properties, such as the convection terms of the momentum equation used here as an example, becomes

$$\overline{I_\varphi \rho \boldsymbol{u}\boldsymbol{u}} = \alpha_\varphi \bar{\rho}_\varphi \tilde{\boldsymbol{u}}_{\boldsymbol{\varphi}} \tilde{\boldsymbol{u}}_{\boldsymbol{\varphi}} + \alpha_\varphi \bar{\rho}_\varphi \left(\widetilde{\boldsymbol{u}''_\varphi \boldsymbol{u}''_\varphi} \right), \tag{4.5}$$

where $\alpha_\varphi \bar{\rho}_\varphi \left(\widetilde{\boldsymbol{u}''_\varphi \boldsymbol{u}''_\varphi} \right)$ is analogous with Reynolds stresses in single phase flows and requires modelling. Similar relations hold for non-mass weighted averaging, but without the density variable. These stresses are commonly neglected in transient CFB simulations but are vital for time-averaged simulations.

4.2. Continuity and Momentum Conservation

The continuity equation (4.6) dictates the conservation of mass for phase φ, while the conservation of momentum produces equations for both the gas and particle phase momentum, Equations 4.7-4.8 and Equations 4.9-4.10, respectively. Both phases are considered incompressible. In the momentum equations, the virtual mass, history and lift forces have been ignored. The terms τ_s and τ_g are the viscous stresses, $\boldsymbol{g}$ is gravity and K_d is a momentum transfer coefficient for the drag force. P_s is the solids pressure arising from particle-particle interaction and it requires a closure model, as do drag, solids bulk viscosity λ_s and turbulent stresses. The bulk viscosity represents the solids resistance to compression. (Gidaspow, 1994; Weller, 2005.)

$$\frac{\partial \alpha_\varphi \bar{\rho}_\varphi}{\partial t} + \nabla \cdot \left(\alpha_\varphi \bar{\rho}_\varphi \tilde{\boldsymbol{u}}_\varphi \right) = 0 \tag{4.6}$$

$$\frac{\partial \alpha_g \bar{\rho}_g \widetilde{\boldsymbol{u}}_g}{\partial t} + \nabla \cdot \left(\alpha_g \bar{\rho}_g \widetilde{\boldsymbol{u}}_g \widetilde{\boldsymbol{u}}_g\right) = \nabla \cdot \tau_g - \alpha_g \nabla p + \alpha_g \bar{\rho}_g \boldsymbol{g} - K_d\left(\widetilde{\boldsymbol{u}}_g - \widetilde{\boldsymbol{u}}_s\right) \tag{4.7}$$

$$\tau_g = \mu_g \left[\left(\nabla \widetilde{\boldsymbol{u}}_g + \nabla^{\mathrm{T}} \widetilde{\boldsymbol{u}}_g\right) - \frac{2}{3}\left(\nabla \cdot \widetilde{\boldsymbol{u}}_g\right)\mathbf{I}\right] \tag{4.8}$$

$$\frac{\partial \alpha_s \bar{\rho}_s \widetilde{\boldsymbol{u}}_s}{\partial t} + \nabla \cdot \left(\alpha_s \bar{\rho}_s \widetilde{\boldsymbol{u}}_s \widetilde{\boldsymbol{u}}_s\right) = \nabla \cdot \tau_s - \alpha_s \nabla p - \nabla \mathrm{P_s} + \alpha_s \bar{\rho}_s \boldsymbol{g} - K_d\left(\widetilde{\boldsymbol{u}}_s - \widetilde{\boldsymbol{u}}_g\right) \tag{4.9}$$

$$\tau_s = \mu_s\left(\nabla \widetilde{\boldsymbol{u}}_s + \nabla^{\mathrm{T}} \widetilde{\boldsymbol{u}}_s\right) + \left(\lambda_s - \tfrac{2}{3}\mu_s\right)\left(\nabla \cdot \widetilde{\boldsymbol{u}}_s\right)\mathbf{I} \tag{4.10}$$

4.3. Particle-Fluid Momentum Transfer

For the drag term, the treatment suggested by Gidaspow (1994, p. 151, Model A) as described in section 2.1 was chosen. Two different equations are used for the K_d depending on the volume fraction of the particle phase. In dilute regions, $\alpha_s < 0.2$, the drag formulation Equation 4.11 is used based on a model suggested by Wen and Yu (1966). In denser regions the Ergun (1959) Equation (4.15) is used. The drag coefficient C_D for the Wen and Yu (1966) model is given by Equations 4.12 and 4.13 – as suggested by Schiller and Naumann (1935) – depending on the particle diameter based Reynolds number, Equation 4.14. (Gidaspow, 1994; Enwald et al., 1996, pp. 40-41.)

$$K_d = \frac{3}{4}\frac{C_D \alpha_s \alpha_g \rho_g \left|\widetilde{\mathbf{u}}_g - \widetilde{\mathbf{u}}_s\right|}{d_p} \alpha_g^{-2.65}, \qquad \alpha_s < 0.2 \tag{4.11}$$

$$C_D = \frac{24}{Re_d}\left(1 + 0.15 Re_p^{0.687}\right). \quad Re_d < 1000 \tag{4.12}$$

$$C_D = 0.44\,, Re_p \geq 1000 \tag{4.13}$$

$$Re_d = \frac{d_p \left|\widetilde{\boldsymbol{u}}_g - \widetilde{\boldsymbol{u}}_s\right|}{\nu_g} \tag{4.14}$$

$$K_d = 150\frac{\mu_s \alpha_s^2}{\alpha_g^2 d_p^2} + 1.75\frac{\rho_g \alpha_s}{\alpha_g d_p}\left|\widetilde{\boldsymbol{u}}_g - \widetilde{\boldsymbol{u}}_s\right|, \alpha_s > 0.2 \tag{4.15}$$

4.4. Particle-Particle Interaction and Kinetic Theory for Granular Flow

As the particle phase is modelled as a fluid in the Euler-Euler method, it is necessary to introduce a model for particle-particle interactions. These models usually appear either as additional source term, solids pressure, in the momentum equations or they are included in the viscosity. Two approaches are introduced in this section. Firstly, the powder modulus, or particle normal force model, which only affects the solids pressure, and secondly, Kinetic Theory for Granular Flow (KTGF) which is analogous with kinetic theory for dense gases. KTGF gives values for the shear and bulk viscosity of the particle phase, as well as for solids pressure.

4.4.1. Powder Modulus

The solids pressure can be modelled by introducing a powder modulus term (Equation 4.16) to the momentum equation. This describes the particle normal stress, σ_n, caused by particle collisions. The powder modulus is defined as Equation 4.17 and is strongly dependent on the volume fraction of the particle phase. The powder modulus is related to the speed of wave propagation, v_0, in a granular medium by Equation 4.18. (Gidaspow, 1994, p. 81.)

$$\nabla P_s = \nabla \alpha_s G_{pp} \tag{4.16}$$

$$G_{pp} = \frac{d\sigma_n}{d\alpha_s} \tag{4.17}$$

$$v_0 = \sqrt{G_{pp}/\rho_s} \tag{4.18}$$

Models for the particle-particle interaction should vanish in dilute flow while rapidly increasing at high solids volume fractions. Rietma and Mutsers (1973) correlated experimental data from a tilted fluidized bed with Equation 4.19. However, in numerical simulations Bouillard et al. (1989) found out that the G_α had to be adjusted to prevent unphysically high particle volume fractions and suggested Equation 4.20 for the powder modulus, with typical values of $G_0 = 1$ Pa, $\kappa = 600$ and $\alpha_{s,0} = 0.624$ (Gidaspow, 1994, p. 82). According to Enwald et al. (1997), Gidaspow and Ettediah (1983) had earlier suggested a similar model with parameters $\kappa = 20$ and $\alpha_{s,0} = 0.38$, and Gidaspow and Syamlal (1985) with $\kappa = 500$ and $\alpha_{s,0} = 0.598$. Gidaspow (1994, p. 138) also notes that the powder modulus approach has a tendency to cause unexpected numerical problems in transient simulations.

$$G_{pp} = 10^{-8.76\alpha_g + 5.43} \text{ N/m}^2 \tag{4.19}$$

$$G_{pp} = G_0 e^{\kappa(\alpha_s - \alpha_{s,0})} \tag{4.20}$$

4.4.2. Kinetic Theory Approach and Granular Temperature

A more complicated but physically more complete model for particle-particle interaction is given by the kinetic theory for granular flow. It is based on a suggestion by Ogawa, Unemura and Oshima (1980), that the mechanical energy is first transformed into random particle motion, instead of dissipating directly to heat. They also derived a conservation equation to describe the transport of the small scale random particle motion. An expression for the repulsive force of the particles in shear flow by Bagnold (1954) is generally regarded as the origin of the kinetic theory approach for granular flows. Since then, several different authors have contributed significantly to the development of the models and some of those will be mentioned later in this chapter. In kinetic theory the hard-sphere model is used for particle collisions and the particles are assumed to be smooth and the collisions binary. (Gidaspow, 1994, pp. 239-240.)

If it is assumed that the oscillations of instantaneous particle velocity, $\boldsymbol{u}$', with a mean velocity of zero behave in chaotic manner, the velocity distribution follows the normal distribution, Equation 4.21. Here μ is the mean value and σ^2 is the variance as defined in Equation 4.22. Assuming that the energy of the small scale random motion is divided equally between the coordinate directions in three-dimensional space, the variance is related to the instantaneous velocities through Equation 4.23, where $\boldsymbol{u}'^2 = u_x'^2 + u_y'^2 + u_z'^2$. (Gidaspow, 1994, p. 241.)

$$f_N(x) = \frac{1}{\sqrt{2\pi\sigma^2}} e^{\left[-\frac{(x-\mu)^2}{2\sigma^2}\right]} \tag{4.21}$$

$$\sigma^2 = \langle (x-\mu)^2 \rangle = \int_{-\infty}^{\infty} (x-\mu)^2 f_N dx \tag{4.22}$$

$$\sigma_c^2 = n\langle \boldsymbol{u}'^2 \rangle = \int\int\int \boldsymbol{u}'^2 f_x f_y f_z d\boldsymbol{c} \tag{4.23}$$

The concept of conserved energy of random particle motion is analogous to temperature and random motion of molecules in dense gases. Jenkins and Savage labelled the energy of random particle motion in granular flow as *granular temperature*, with Θ as the symbol. It is defined as one third of the mean square of the particle velocity, Equation 4.24. The normal distribution for the particle velocities, called Maxwellian distribution, can now be written as Equation 4.25, with $\overline{\boldsymbol{u}}$ being the mean velocity. (Gidapow,1994, p. 242.)

$$\Theta = \frac{1}{3}\langle \boldsymbol{u}'^2 \rangle \tag{4.24}$$

$$f_c = \frac{n}{(2\pi\Theta)^{3/2}} e^{\left[-\frac{(\boldsymbol{u}'-\overline{\boldsymbol{u}})^2}{2\Theta}\right]} \tag{4.25}$$

A common approach is to assume a local equilibrium between the production and dissipation of granular temperature. The granular temperature can then be described with an algebraic model. A more general approach is to solve a transport equation for the granular temperature, Equation 4.26 (Gidaspow, 1994, p. 315). It is derived by writing the Boltzmann integral-differential conservation equation for the probability distribution of random particle motion. Descriptions of the derivation can be found in Gidaspow (1994, pp. 256-294) and Passalacqua (2008, pp. 17-31).

$$\frac{3}{2}\left[\frac{\partial}{\partial t}(\alpha_s \rho_s \Theta) + \nabla \cdot (\alpha_s \rho_s \widetilde{\boldsymbol{u}}_s \Theta)\right] = (-P_s \boldsymbol{I} + \tau_s) : \nabla \widetilde{\boldsymbol{u}}_s + \nabla \cdot (\kappa_s \nabla \Theta) - \gamma_s - J_{vis} + J_{slip}$$

		(4.26)
Production	$(-P_s \boldsymbol{I} + \tau_s) : \nabla \widetilde{\boldsymbol{u}}_s$	
Granular energy diffusion flux	$+\nabla \cdot (\kappa_s \nabla \Theta)$	
Dissipation due to inelastic collisions	$-\gamma_s$	
Dissipation due to fluid viscosity	$-J_{vis}$	
Production due to fluid turbulence	$+J_{slip}$	

The solids shear viscosity, μ_s, includes both the collisional and kinetic components, Equation 4.27. The collisional part is described by Equation 4.28 and the kinetic by Equation 4.29 (Gidaspow, 1994, p. 303, 314). The Equation 4.31 for the bulk viscosity of the solids phase closely resembles the collisional shear viscosity equation.

$$\mu_s = \mu_{s,col} + \mu_{s,kin} \tag{4.27}$$

$$\mu_{s,col} = \frac{4}{5}\alpha_s^2 \rho_s d_p g_0 (1 + e_s)\sqrt{\frac{\Theta}{\pi}} \tag{4.28}$$

$$\mu_{s,kin} = \frac{2\mu_{s,dilute}}{g_0(1+e_s)}\left[1+\frac{4}{5}(1+e_s)\alpha_s g_0\right]^2 \quad (4.29)$$

$$\mu_{s,dilute} = \frac{5\sqrt{\pi\Theta}}{96}\rho_s d_p \quad (4.30)$$

$$\lambda_s = \frac{4}{3}\alpha_s^2\rho_s d_p g_0(1+e_s)\sqrt{\frac{\Theta}{\pi}} \quad (4.31)$$

In these equations e_s is the coefficient of restitution for the solids and g_0 is the radial distribution function. The radial distribution function describes the probability of particle collisions and becomes infinite at the packing limit. This behaviour limits the maximum volume fraction of the particle phase as the last term of solids pressure, Equation 4.34, as proposed by Lun et al. (1984) is proportional to g_0. Ogawa et al. (1980) suggested Equation 4.32 for the radial distribution function, but Equation 4.33 suggested by Lun and Savage (1986) is used in the CFD simulations of this thesis. Gidaspow (1990) suggested multiplying Equation 4.32 by 0.6 for a better fit with numerical data, but Peirano and Leckner (1998) consider the suggestion invalid. (Peirano and Leckner, 1997, p. 273.)

$$g_0 = \frac{1}{1-\left(\frac{\alpha_s}{\alpha_{s,max}}\right)^{1/3}} \quad (4.32)$$

$$g_0 = \frac{1}{\left(1-\frac{\alpha_s}{\alpha_{s,max}}\right)^{2.5\alpha_{s,max}}} \quad (4.33)$$

$$P_s = \rho_s\alpha_s\Theta + 2\alpha_s^2 g_0\Theta(1+e_s) \quad (4.34)$$

The diffusion of the granular energy flux term is analogous to the conduction of heat. The diffusion coefficient, κ_s, is called the conductivity of the granular energy and is defined as Equations 4.35-36 (Gidaspow, 1994, p.315).

$$\kappa_{dilute} = \frac{75}{384}\sqrt{\pi\Theta}\rho_s d_p \quad (4.35)$$

$$\kappa_s = \frac{2}{(1+e_s)g_0}\left[1+\frac{6}{5}(1+e_s)g_0\alpha_s\right]^2\kappa_{dilute} \quad (4.36)$$

$$+2\alpha_s^2\rho_s d_p g_0(1+e_s)\sqrt{\frac{\Theta}{\pi}}$$

The inelasticity of collisions is included in the models using the coefficient of restitution. The dissipation of the granular energy due to inelastic collisions is modelled with Equation 4.37 (Gidaspow, 1994, p. 315). The dissipation caused by viscous fluid effects is modelled with the simple Equation 4.38.

$$\gamma_s = 3(1-e_s^2)\alpha_s^2\rho_s g_0\Theta\left(\frac{4}{d_p}\sqrt{\frac{\Theta}{\pi}} - \nabla\cdot\widetilde{\boldsymbol{u}}_s\right) \tag{4.37}$$

$$J_{vis} = 3K_d\Theta \tag{4.38}$$

Many authors, including Gidaspow (1994), neglect the fluid turbulence, or particle-fluid velocity correlation, production term, but Koch (1990) derived Equation 4.39 to describe it in a monodispersed, dilute, gas-solid suspension of elastic particles. The equation has been used since by Agrawal et al. (2001) and Huilin et al. (2003; 2006). It was later extended by Koch and Sangani (1999) to form Equation 4.40. (Passalacqua, 2008, p. 33-34.)

$$J_{slip} = \frac{d_p\rho_s}{4\sqrt{\pi\Theta}}\left(\frac{18\mu_g}{d_p^2\rho_s}\right)^2\left|\widetilde{\boldsymbol{u}}_g - \widetilde{\boldsymbol{u}}_s\right|^2 \tag{4.39}$$

$$J_{slip} = \frac{81\alpha_s\mu_g}{g_0 d_p^3\rho_s\sqrt{\pi\Theta}}\left|\widetilde{\boldsymbol{u}}_g - \widetilde{\boldsymbol{u}}_s\right|\varphi$$

$$\varphi = \frac{R_d^2}{1+3.5\sqrt{\alpha_s}+5.9\alpha_s}$$

$$R_d = \begin{cases} \dfrac{1+3\sqrt{\frac{\alpha_s}{2}}+\frac{135}{64}\alpha_s ln(\alpha_s)+17.4\alpha_s}{1+0.681\alpha_s-8.48\alpha_s^2+8.16\alpha_s^3}, & \alpha_s < 0.4 \\ \dfrac{10\alpha_s}{(1-\alpha_s)^3}+0.7, & \alpha_s \geq 0.4 \end{cases} \tag{4.40}$$

4.4.3. Frictional Stresses

In the derivation of the kinetic theory for granular flow, it was assumed that collisions between the particles are binary and instantaneous. While these are reasonable assumptions at low particle volume fractions, they do not apply in densely packed regions where particles are in extended contact with several particles. In these regions, most of the particle energy is dissipated by the surface friction between sliding particles, instead of in inelastic collisions. (Tardos, 1997, p. 61.)

Coulomb suggested a simple model where powder is modelled as a rigid, totally plastic continuum flowing on a plane by yielding with a critical shear stress, τ_f, as given by Equation 4.41. Here the normal stress, σ_N, and the angle of internal friction, φ_f, are material properties, and k_f is the cohesive force between the particles. For non-cohesive powders k_f is zero. When the shear stress exceeds the critical value, the material becomes infinitely deformable. In effect, the model describes simple sliding friction that is proportional to the normal force and the coefficient of friction represented by $tan(\varphi_f)$. (Tardos, 1997, p.62.)

$$\tau_f = \sigma_N \tan(\varphi_f) + k_f \tag{4.41}$$

Johnson and Jackson (1987) suggested frictional, $\tau_{s,f}$, and kinetic, $\tau_{s,kt}$, stresses can be considered as additive, Equation 4.42, with the frictional stress defined by Equation 4.43. $P_{s,f}$ is the normal force, called frictional pressure, and $\mu_{s,f}$ is the frictional viscosity representing the sliding friction between the particles. They proposed that the frictional pressure is zero below an experimental threshold solids volume fraction value, $\alpha_{s,f,min}$, and calculated by a correlation above it, Equation 4.44. Here F, r and s are experimental parameters. Johnson and Jackson (1987) suggested values: $\alpha_{s,f,min} = 0.5$, $F = 0.05$ $r = 2$ and $s = 5$. For the frictional viscosity they used the simple Equation 4.45, which is valid for their chute application.

$$\tau_s = \tau_{s,kt} + \tau_{s,f} \tag{4.42}$$

$$\tau_{s,f} = P_{s,f}\boldsymbol{I} + \mu_{s,f}(\nabla\tilde{\boldsymbol{u}}_s + (\nabla\tilde{\boldsymbol{u}}_s)^T) \tag{4.43}$$

$$P_{s,f} = \begin{cases} 0, & \alpha_{s,} < \alpha_{s,f,min} \\ F\dfrac{(\alpha_s - \alpha_{s,f,min})^r}{(\alpha_{s,max} - \alpha_s)^s}, & \alpha_{s,} \geq \alpha_{s,f,min} \end{cases} \tag{4.44}$$

$$\mu_{s,f} = P_{s,f}\sin(\varphi_f) \tag{4.45}$$

A similar, but more general, model was proposed by Schaeffer (1987), Equation 4.46. Here $\boldsymbol{S}$ is the rate of deformation tensor, Equation 4.47. Equation 4.46 reduces to Equation 4.41 in two-dimensional cases (Tardos, 1997, Appendix B), and also satisfies both the von Mises yield condition (Tardos, 1997, Appendix C) and the co-axiality condition, which states that directions of stress and deformation are parallel (Tardos, 1997, Appendix A). Like the Johnson and Jackson (1987) model, Schaeffer uses a threshold solids volume fraction below which the frictional stresses are zero. (Tardos, 1997, p. 63; Srivastava and Sundaresan, 2003, pp. 74-75.)

$$P_{s,f} = \begin{cases} 0, & \alpha_{s,} < \alpha_{s,f,min} \\ 10^{25}\alpha_s\left(\alpha_s - \alpha_{s,f,min}\right)^{10}, & \alpha_{s,} \geq \alpha_{s,f,min} \end{cases}$$

$$\mu_{s,f} = P_{s,f}\frac{\sqrt{2}sin(\varphi_f)}{2\sqrt{\boldsymbol{S}:\boldsymbol{S}}} \tag{4.46}$$

$$\boldsymbol{S} = \frac{1}{2}[(\nabla\tilde{\boldsymbol{u}}_s + (\nabla\tilde{\boldsymbol{u}}_s)^T)] - \frac{1}{3}(\nabla\cdot\tilde{\boldsymbol{u}}_s) \tag{4.47}$$

Syamlal et al. (1993) proposed a sharp switch between the kinetic and frictional stresses at a threshold solids volume fraction value, Equation 4.48, instead of the additive approach of Johnson and Jackson (1987), Equation 4.42.

$$\tau_s = \begin{cases} P_{s,kt}\boldsymbol{I} + \mu_{s,kt}, & \alpha_{s,} < \alpha_{s,f,min} \\ P_{s,f}\boldsymbol{I} + \mu_{s,f}, & \alpha_{s,} \geq \alpha_{s,f,min} \end{cases} \tag{4.48}$$

Srivastava and Sundaresan (2003) combined the frictional pressure model and additive approach of Johnson and Jackson (1987) with the frictional viscosity model of Schaeffer (1987). Following Savage's (1998) findings, they included the stress reducing effect of particle fluctuations as a granular temperature term in the frictional viscosity model. The result is the model of equation set 4.49. As this is the physically most complete of the models in this chapter, it has been used in the CFD simulations of this thesis. (Srivastava and Sundaresan, 2003, pp. 74-75.)

$$\tau_s = \tau_{s,kt} + \tau_{s,f}$$

$$\tau_{s,f} = P_{s,f}\boldsymbol{I} + \mu_{s,f}(\nabla\widetilde{\boldsymbol{u}}_s + (\nabla\widetilde{\boldsymbol{u}}_s)^T)$$

$$P_{s,f} = \begin{cases} 0, & \alpha_{s,} < \alpha_{s,f,min} \\ F\dfrac{(\alpha_s - \alpha_{s,f,min})^r}{(\alpha_{s,max} - \alpha_s)^s}, & \alpha_{s,} \geq \alpha_{s,f,min} \end{cases} \tag{4.49}$$

$$\mu_{s,f} = P_{s,f}\frac{\sqrt{2}sin(\varphi_f)}{2\sqrt{\boldsymbol{S}:\boldsymbol{S} + \frac{\Theta}{d_p^2}}}$$

4.4.4. Wall Boundary Conditions

Johnson and Jackson (1987) derived equations for the stresses and dissipation of granular temperature caused by particle-wall interaction. They equated the frictional, $P_{s,f}\tan(\varphi_f)$, and collisional, $\mathbf{S}_c^b$, stresses on the wall to the bulk stress of the particle phase in the direction of the slip velocity between the particles and the wall, $\widetilde{\boldsymbol{u}}_{slip}$. For the granular temperature, they wrote an energy balance, Equation 4.51, between the granular energy flux, $\mathbf{q}_\Theta$, the dissipation, $\gamma_{s,w}$, and the collisional stress in the direction of the slip velocity. The relations they found are described by Equations 4.50-53. (Passalacqua, 2008, pp. 38-40.)

$$\frac{\widetilde{\boldsymbol{u}}_{slip}\cdot(\tau_c + \tau_f)\cdot\boldsymbol{n}_w}{|\widetilde{\boldsymbol{u}}_{slip}|} + \mathbf{S}_c^b + P_{s,f}\tan(\varphi_f) = 0 \tag{4.50}$$

$$\boldsymbol{n}_w \cdot \mathbf{q}_{\Theta,w} = \gamma_{s,w} + \boldsymbol{u}_{slip}\cdot\mathbf{S}_c^b \tag{4.51}$$

$$\mathbf{S}_c^b = \frac{\pi\phi_{spec}\rho_s|\widetilde{\boldsymbol{u}}_{slip}|\sqrt{3\Theta^2}}{6\alpha_{s,max}\left[1 - \left(\frac{\alpha_{s,max}}{\alpha_s}\right)^{1/3}\right]} \tag{4.52}$$

$$\gamma_{s,w} = \frac{1}{4}\pi\rho_s\Theta(1 - e_w^2)\frac{\sqrt{3\Theta}}{\left(\frac{\alpha_{s,max}}{\alpha_s}\right)^{2/3}\left[\left(\frac{\alpha_{s,max}}{\alpha_s}\right)^{1/3} - 1\right]} \tag{4.53}$$

Here ϕ_{spec} is a specularity coefficient that describes the diffuseness of the particle collisions caused by the roughness of surfaces. Its value is 1 for perfectly diffuse collisions and 0 for perfectly specular ones. In practice, the specularity coefficient is often used in CFD simulations as a fitting parameter to get the correct wall velocities. If the frictional contribution to the wall stress is ignored, the relations can be written in the form of Equations 4.54-55 with g_0 from Equation 4.32. (Passalacqua, 2008, pp. 38-40.) These are the forms which are used as boundary conditions in the CFD simulations carried out in this thesis.

$$\tau_{s,w} = -\frac{\pi}{6}\frac{\alpha_s}{\alpha_{s,max}}\phi_{spec}\rho_s g_0\sqrt{3\Theta}\tilde{\boldsymbol{u}}_{slip} \tag{4.54}$$

$$\begin{aligned}\mathbf{q}_{\Theta,w} = &\frac{\pi}{6}\frac{\alpha_s}{\alpha_{s,max}}\phi_{spec}\rho_s g_0\sqrt{3\Theta}\left|\tilde{\boldsymbol{u}}_{slip}\right|^2 \\ &-\frac{\pi}{4}\frac{\alpha_s}{\alpha_{s,max}}(1-e_w^2)\rho_s g_0\sqrt{3\Theta^3}\end{aligned} \tag{4.55}$$

Peirano and Leckner (1997, pp. 287-288) dispute Johnson and Jackson's boundary conditions for the use of the specularity coefficient, and prefer models based on work by Jenkins and Louge (Jenkins, 1992; Louge, 1994; Jenkins and Louge, 1997).

4.5. Turbulence Models

The standard method for turbulence modelling in single-phase flows is the Reynolds decomposition. Here the fluid velocity, $\mathbf{u}$, is divided into mean, $\bar{\mathbf{u}}$, and fluctuating, $\mathbf{u}'$, components, Equation 4.56. When the decomposed velocity is placed into Navier-Stokes equations and averaged over time, the results are the Reynolds Averaged Navier-Stokes (RANS) equations, Equation 4.57 for the momentum of incompressible Newtonian flow. These differ from the original by including an additional stress, $\boldsymbol{\tau}_{Re}$, the Reynolds stress, which has to be modelled. Descriptions of common turbulence modelling approaches and their background can be found, for example, in the book by Pope (2000).

$$\mathbf{u} = \bar{\mathbf{u}} + \mathbf{u}' \tag{4.56}$$

$$\begin{aligned}\rho\frac{\partial\bar{\mathbf{u}}}{\partial t} + \rho\bar{\mathbf{u}}\cdot\nabla\bar{\mathbf{u}} &= -\nabla p + \nabla\cdot(\boldsymbol{\tau} + \boldsymbol{\tau}_{Re}) + \mathbf{f} \\ \boldsymbol{\tau} &= \mu\left[(\nabla\bar{\mathbf{u}} + (\nabla\bar{\mathbf{u}})^T) - \frac{2}{3}(\nabla\cdot\bar{\mathbf{u}})\mathbf{I}\right] \\ \boldsymbol{\tau}_{Re} &= \rho\overline{\mathbf{u}'\mathbf{u}'}\end{aligned} \tag{4.57}$$

Several different models have been suggested for the Reynolds stress. Most common approaches are similar to what Launder and Spalding (1974) proposed. Here, transport equations are solved for the kinetic energy of turbulence, k, and the dissipation of the turbulent kinetic energy, ε. The Reynolds stress is assumed to be isotropic and is modelled as increased effective viscosity. The effective viscosity, μ_{eff}, is the sum of the molecular, μ, and turbulent (i.e. eddy), μ_t, viscosities. The turbulent viscosity is related to the turbulent kinetic energy and dissipation by Equation 4.59, where C_μ is a model constant.

$$\mu_{eff} = \mu + \mu_t \tag{4.58}$$

$$\mu_t = \rho C_\mu \frac{k^2}{\varepsilon} \tag{4.59}$$

$$\boldsymbol{\tau} + \boldsymbol{\tau}_{Re} = (\mu + \mu_t)\left[(\nabla\bar{\mathbf{u}} + (\nabla\bar{\mathbf{u}})^{\mathrm{T}}) - \frac{2}{3}(\nabla\cdot\bar{\mathbf{u}})\mathbf{I}\right] \tag{4.60}$$

Another approach is to solve filtered Navier-Stokes equations with transient simulations. Here the turbulent motion in scales larger than the filter size is resolved directly, and only the smaller scales have to be modelled. Hence, the method is commonly referred to as Large Eddy Simulation (LES). A residual [or Sub-Grid Scale (SGS)] stress tensor similar to the Reynolds stress in the RANS is also present in the filtered momentum equations and requires modelling. Otherwise the equations are of the standard form. The SGS stress, $\boldsymbol{\tau}_{SGS}$, can be divided into isotropic and anisotropic, $\boldsymbol{\tau}_r$, components. Residual kinetic energy is the trace of the SGS stress tensor divided by two, Equation 4.61. The anisotropic stress component can be obtained by subtracting the isotropic component, Equation 4.62. (Pope, 2000, pp. 581; 558-559.)

$$k_r = \frac{1}{2}\mathrm{tr}(\boldsymbol{\tau}_{SGS}) \tag{4.61}$$

$$\boldsymbol{\tau}_r = \boldsymbol{\tau}_{SGS} - \frac{2}{3}k_r\boldsymbol{I} \tag{4.62}$$

Approaches similar to single phase flows, RANS and LES, are used for multiphase flows to describe the continuous phase turbulence. Several authors (including Samuelsberg and Hjertager (1996), Huilin and Gidaspow (2003), Huilin et al. (2006) Ibsen et al. (2000; 2004) and Passalacqua (2008)) have used models based on algebraic the closure suggested by Smagorinsky (1963) for $\boldsymbol{\tau_r}$ in simulations of gas-solid risers (Passalacqua, 2008, p.44). In the model, $\boldsymbol{\tau}_r$ is proportional to the rate of strain tensor through the kinematic eddy viscosity, ν_r This is modelled with Equation 4.64, where $\overline{\boldsymbol{S}}$ is the filtered rate of strain tensor and l_s is the Smagorinsky length scale. It is assumed

to be proportional to the filter size, Δ, and the Smagorinsky coefficient, C_s. Filter size is calculated by taking a cube root of the product of the computational cell dimensions, Equation 4.65. (Pope, 2000, pp. 587.)

$$\boldsymbol{\tau}_r = -2\nu_r\overline{\boldsymbol{S}} \tag{4.63}$$

$$\nu_r = l_s^2\overline{\boldsymbol{S}} = (C_s\Delta)_s^2\overline{\boldsymbol{S}} \tag{4.64}$$

$$\Delta = \sqrt[3]{\Delta x \Delta y \Delta \mathrm{z}} \tag{4.65}$$

In the CFD simulations for this thesis the Smagorinsky SGS stress closure was used for continuous phase turbulence with $C_s = 0.16$. It should be noted that the physical background of LES turbulence modelling is not valid in 2D simulations as carried out in this thesis. However, it does serve to demonstrate the effects of including a turbulent viscosity for the fluid. In addition, the model neglects the turbulence modulation effects caused by the presence of the particles.

5. NUMERICAL METHOD

The three most common methods for numerically solving partial differential equations are the Finite Difference (FDM), Finite Element (FEM) and Finite Volume (FVM) Methods. Common to all of these is that the computational domain is divided into smaller regions with a computational grid, and the differential equations are approximated at discrete points using algebraic equations. Different schemes can be used for approximation and interpolation, usually trading complexity and computational costsfor accuracy. (Ferziger and Peric, 2002, pp. 31; 35-37.) Discretization schemes are often classified as being *n*th order. This implies that the scheme includes *n* first terms of the Taylor series expansion, which can be used to express any continuous differentiable function.

FDM is the oldest and simplest method, but still perfectly usable for simple geometries. Its development is credited to Leonhard Euler (1707-1783) in the 18th century. The higher order discretization schemes are easiest to implement with FDM, but the enforcement of conservation requires special care. FEM is the standard method in structural analysis and many other fields. The major advantage of FEM is its easy and flexible mesh generation, making it suitable for deformations and other such phenomena. It differs from the other methods by using weight functions. (Ferziger and Peric, 2002, pp. 35-37.)

For CFD the standard method is FVM, which is rarely used for other purposes. In FVM the domain is divided into control volumes (CV) and the integral form of the conservation equations are applied to each of them. The variables are defined at the centres of the CVs and are interpolated to the CV boundaries. Importantly for CFD, conservation is built into the method. Other reasons for its popularity are that it can be applied to any kind of computational mesh, as the mesh only defines the boundaries of the CVs – instead of the computational nodes as in FDM – and all the variables have a clear physical meaning. (Ferziger and Peric, 2002, p. 36, 70.)

Once the chosen discretization has been applied to the Navier-Stokes equations, the result is a coefficient matrix, describing a system of non-linear algebraic equations. Because of the non-linearity of the equations an iterative solution method is used, where the equations are successively linearized with the results of the previous iteration. Once the equations are linearized they can be solved either directly or iteratively. There are several mathematical methods for both approaches. With the iterative methods, the

convergence of the solution has to be verified. As the exact solutions are not known in CFD, the convergence has to be checked by numerical experiments i.e. by comparing successive iterative solutions. A common practice is to monitor the residual, $\boldsymbol{\epsilon}$, of the iterative solution. This is defined as the imbalance in the algebraic equation system, Equation 5.1, where $\boldsymbol{A}$ is the coefficient matrix, $\boldsymbol{x}$ the variable vector and $\boldsymbol{b}$ the source term vector.

$$\begin{aligned} \boldsymbol{Ax} &= \boldsymbol{b} \\ \boldsymbol{\epsilon} &= \boldsymbol{Ax} - \boldsymbol{b} \end{aligned} \tag{5.1}$$

It should be noted that the residual may not be a reliable indicator of convergence and it is often useful to monitor some integrated variables as well. Often the residual is scaled with some algorithm in an attempt to make it more representative.

5.1. Open Source CFD: OpenFOAM

Open source software is an attractive tool for academic and research purposes. Unrestricted access allows detailed insight into the algorithms used and limitless customization for specific purposes. In CFD applications, the lack of licensing fees makes massively parallel computations economically feasible, provided that the parallelization of the solver is efficient. For these reasons a feasibility study using OpenFOAM (OpenCFD Ltd., 2003-2009) to simulate the pilot-scale CFB was conducted.

OpenFOAM is an open source code library for the solution of field problems found in mathematics, physics and engineering. It uses the finite volume method, with unstructured mesh, and comes with a wide variety of pre-built solvers and model libraries. The main application for OpenFOAM has been CFD. Recent OpenFOAM releases include a solver called twoPhaseEulerFoam, which provides a promising starting point for the simulation of a CFB.

5.2. Solver: twoPhaseEulerFoam

TwoPhaseEulerFoam is a two-fluid, Euler-Euler method solver for incompressible two-phase turbulent flows. It has been included in OpenFOAM releases since verion 1.3 with small variations. This thesis concentrates on the version in release 1.5, but is also largely applicable to the current release, 1.6.

The twoPhaseEulerFoam is based on a solver called bubbleFoam, which is a result of Henrik Rusche's work for his PhD thesis "Computational Fluid Dynamics of Dispersed

Two-Phase Flows at High Phase Fractions" (2002) and on further development (Weller, 2002, 2005) of the algorithm developed for the BRITE II project at Imperial College. TwoPhaseEulerFoam differs from bubbleFoam by the addition of models for particle-particle interaction. Two alternative approaches are included. Firstly, with a particle normal force, i.e. a powder modulus model as suggested by Gidaspow et al. (1983; 1985) and Bouillard et al. (1989) and secondly, using the kinetic theory for granular flow (KTGF) model.

On initial inspection the solver provides most of the sub-models commonly used in Eulerian simulation of gas-solid flows. A notable shortcoming is the lack of a turbulence model that would include the turbulence modulation caused by the presence of the particle phase. The models included are listed in Table 5.1.

5.2.1. Solution Algorithm

In the equations of this chapter the phases are distinguished by the letters a and b in the same way that they are used in the twoPhaseEulerFoam solver. In gas-solid simulation, phase a is the solid phase and phase b the gas phase. Velocities and pressures in this chapter are ensemble averaged, unless stated otherwise.

To avoid singularities at zero volume fractions, twoPhaseEulerFoam employs phase-intensive momentum Equations 5.2-3, as suggested by Weller (2002; 2005 pp. 15-16), where the momentum equations are divided by the volume fraction and density. Thus, A_d, A_l and A_{vm} are momentum transfer coefficients for the drag, lift and virtual mass forces respectively. The formulations of the coefficients are presented in Equations 5.6-5.9. For gas-solid simulations, Equation 5.7 is used for drag instead of the blended Equation 5.6. For the pilot-scale CFB the lift and virtual mass terms are neglected.

$$\frac{\partial \boldsymbol{u}_b}{\partial t} + \boldsymbol{u}_b^{\boldsymbol{T}} \cdot \nabla \boldsymbol{u}_b - \nabla \cdot \left(\nu_{eff,b} \nabla \boldsymbol{u}_b\right) + \nabla \cdot \tau_b + \frac{\nabla \alpha_b}{\alpha_b} \cdot \tau_b = -\frac{\nabla p}{\rho_b} + \boldsymbol{g} - \frac{\alpha_a}{\rho_b}\left(A_d(\boldsymbol{u}_b - \boldsymbol{u}_a) + A_l + A_{vm}\left(\frac{d\boldsymbol{u}_b}{dt} - \frac{d\boldsymbol{u}_a}{dt}\right)\right) \tag{5.2}$$

$$\frac{\partial \boldsymbol{u}_a}{\partial t} + \boldsymbol{u}_a^{\boldsymbol{T}} \cdot \nabla \boldsymbol{u}_{\boldsymbol{a}} - \nabla \cdot \left(\nu_{eff,a} \nabla \boldsymbol{u}_a\right) + \nabla \cdot \tau_a + \frac{\nabla \alpha_a}{\alpha_a} \cdot \tau_a = -\frac{\nabla p}{\rho_a} + \boldsymbol{g} - \frac{\alpha_b}{\rho_a}\left(A_d(\boldsymbol{u}_a - \boldsymbol{u}_b) + A_l + A_{vm}\left(\frac{d\boldsymbol{u}_a}{dt} - \frac{d\boldsymbol{u}_b}{dt}\right)\right) \tag{5.3}$$

$$\boldsymbol{u}_c = \alpha_a \boldsymbol{u}_a + \alpha_b \boldsymbol{u}_b \tag{5.4}$$

$$\boldsymbol{u}_r = \boldsymbol{u}_b - \boldsymbol{u}_a \tag{5.5}$$

Table 5.1. *Sub models included in the twoPhaseEulerFoam solver, OpenFOAM 1.5.*

Turbulence	Two-equation, k-ε continuous phase turbulence model, with transfer of turbulence kinetic energy to the dispersed phase by coefficient C_t.
Drag	Gibilaro (1985)
	Ergun (1952)
	Shciller, Naumann (1935)
	Wen, Yu (1966)
	Gidaspow (1994)
	Syamlal, O'Brien (1988)
Particle normal force	As proposed by Gidaspow (1983; 1985) and Bouillard et al. (1989)
Kinetic Theory for Granular flow, KTGF:	
KTGF: Granular pressure	Lun et al. (1984)
	Syamlal, Rogers, O'Brien (1993)
KTGF: Radial Distribution	Gidaspow (1990)
	Lun-Savage (1986)
	"Sinclair-Jackson" (Ogawa et al. 1980)
	Carnahan-Starling (1969)
KTGF: Bulk Viscosity	Lun et al. (1984)
KTGF: Viscosity	Gidaspow (1994)
	Syamlal (1993)
	Hrenya-Sinclair (1997)
KTGF: Frictional Stress	Johnson-Jackson (1987)
	Schaeffer (1987)
KTGF: Granular Temperature	Local equilibrium
	Transport equation

$$A_d = \frac{3}{4}\left(\alpha_b \frac{C_{D,a}\rho_b}{d_a} + \alpha_a \frac{C_{D,b}\rho_a}{d_b}\right)|\boldsymbol{u}_r| \tag{5.6}$$

$$A_d = \frac{3}{4}\frac{C_{D,a}\rho_b}{d_a}|\boldsymbol{u}_r| \tag{5.7}$$

$$A_l = \left(\alpha_b C_{l,a}\rho_b + \alpha_a C_{l,b}\rho_a\right)\boldsymbol{u}_r \times \nabla \times \boldsymbol{u}_\varphi, \qquad \varphi = a, b \tag{5.8}$$

$$A_{vm} = \alpha_b C_{vm,a}\rho_b + \alpha_a C_{wm,b}\rho_a \tag{5.9}$$

The continuity equation is written for the conservation of volume instead of mass, in order to improve the conservation in simulations with large density ratios. In the continuity equation, the velocity is decomposed into the mixture velocity, $\boldsymbol{u}_c$, and the relative velocity, $\boldsymbol{u}_r$, between the phases as shown in Equations (5.4-5; 5.10-11). In this form, all the terms are in conservative form; α can be bounded at both ends and the coupling of the phase fluxes is more implicit due to the presence of the relative flux. The problem with the formulation is that the equation is non-linear in FVM and, as such, the boundedness can only be guaranteed if the equation is solved fully implicitly. (Rusche, 2002, p. 108, 118; Weller, 2005, pp. 16-17.)

$$\frac{\partial \alpha_a}{\partial t} + \nabla \cdot (\boldsymbol{u}_c \alpha_a) + \nabla \cdot (\boldsymbol{u}_r \alpha_a \alpha_b) = 0 \tag{5.10}$$

$$\alpha_b = 1 - \alpha_a \tag{5.11}$$

OpenFOAM uses a collocated variable arrangement, which means that special care has to be taken with the pressure-velocity coupling. To avoid the problem, Weller (2002, 2005) formulated a solution method that mimics a staggered variable arrangement. The solution algorithm uses a momentum predictor, pressure correction loop (Pressure-Implicit Split-Operator, PISO) and a correction of momentum based on the change in pressure. The difference is that the velocities are obtained from the pressure corrected flux fields through a reconstruction method. With this method the flux is the primary variable instead of the velocity, and the pressure-velocity decoupling is not possible. The flux field is defined on the cell boundaries, resembling a staggered variable arrangement. (Weller, 2005, pp. 17-22; Rusche, 2002, p. 126.)

The flux predictor is the discretized momentum equation, with the difference that the buoyancy and the explicit part of the drag terms are included on the cell-faces, with the values determined by interpolation with central differencing. (Rusche, 2002, p. 126.) The coefficient matrix of the linear equations system, $\mathcal{A}_\varphi$, does not include these terms.

In twoPhaseEulerFoam the same treatment is used for particle normal force, granular pressure and frictional pressure terms. All these terms appear as apparent pressure in the particle phase momentum equation. The semi-discretized momentum equation for phase "a" is shown in Equations 5.12-13. The operators $(\mathcal{A}_a)_D$and $(\mathcal{A}_a)_H$ are respectively the diagonal and off-diagonal elements of the coefficient matrix $\mathcal{A}_a$. A detailed description of the method can be found in Rusche's PhD thesis (2002, p. 95, 96, 126) and in Weller's (2005) report.

$$(\mathcal{A}_a)_D \boldsymbol{u}_a = (\mathcal{A}_a)_H - \frac{\nabla p}{\rho_a} - \frac{\mathrm{G_{pp}} \nabla \alpha_a}{\alpha_a \rho_a} - \frac{\nabla P_s}{\alpha_a \rho_a} + \frac{A_d \boldsymbol{u}_b}{\alpha_a \rho_a} \tag{5.12}$$

$$\boldsymbol{u}_a = \frac{(\mathcal{A}_a)_H}{(\mathcal{A}_a)_D} - \frac{\nabla p}{\rho_a (\mathcal{A}_a)_D} - \frac{\mathrm{G_{pp}} \nabla \alpha_a}{\alpha_a \rho_a (\mathcal{A}_a)_D} - \frac{\nabla P_s}{\alpha_a \rho_a (\mathcal{A}_a)_D} + \frac{A_d \boldsymbol{u}_b}{\alpha_a \rho_a (\mathcal{A}_a)_D} \tag{5.13}$$

For the particle normal force model, an approach suggested by Weller (2002) for the turbulent stress term is adopted, as both terms are proportional to $\nabla \alpha_\phi$. Again, a detailed description of the approach can be found in Rusche's PhD thesis (2002, pp. 118-120). The turbulent stress term itself is neglected both in bubbleFoam and twoPhaseEulerFoam.

In this approach, the term proportional to $\nabla \alpha_\phi$ is treated as a diffusion term in the transport equation for dispersed phase volume fraction. Before adding the diffusion term to the equation, the mixture and relative velocities are corrected for the contribution of the term to be added. The treatment of the particle normal force term in twoPhaseEulerFoam and the turbulent drag term treatment suggested by Weller differ slightly, as the particle normal force only applies to the dispersed phase velocity field. The treatment as found in the twoPhaseEulerFoam is presented in Equations 5.14-23. The Equation 5.14 for powder modulus, G_{pp}, has the form suggested by Gidaspow et al. (1983; 1985) and Bouillard et al. (1989) that was presented earlier, in Equation 4.20.

$$G_{pp} = G_0 e^{\kappa(\alpha_a - \alpha_0)} \tag{5.14}$$

$$\boldsymbol{u}_\varphi^* = \boldsymbol{u}_\varphi + \frac{G_{pp}}{\rho (\mathcal{A}_\varphi)_D} \nabla \alpha_\varphi \tag{5.15}$$

$$\boldsymbol{u}_r^* = \boldsymbol{u}_a^* - \boldsymbol{u}_b \tag{5.16}$$

$$\boldsymbol{u}_c^* = \boldsymbol{u}_a^* + \boldsymbol{u}_b \tag{5.17}$$

$$\begin{aligned} \frac{\partial \alpha_a}{\partial t} + \nabla \cdot (\boldsymbol{u}_c^* \alpha_a) + \nabla \cdot \left(\boldsymbol{u}_r^* \alpha_a (1 - \alpha_a)\right) \\ -\nabla \cdot \left(\frac{G_{pp}}{\rho_a (\mathcal{A}_a)_D} \nabla \alpha_a\right) = 0 \end{aligned} \tag{5.18}$$

In semi-discretized form, evaluated on the cell faces and written with the flux field variable, ϕ, instead of velocities, the equations are of the form

$$\begin{aligned} \frac{\partial \alpha_a}{\partial t} + \nabla \cdot (\phi_c^* \alpha_a) + \nabla \cdot \left(\phi_r^* \alpha_a (1 - \alpha_a)\right) \\ -\nabla \cdot \left(\upsilon_{pp} \nabla \alpha_a\right) = 0 \end{aligned} \tag{5.19}$$

where the diffusion coefficient υ_{pp} is defined as

$$\upsilon_{pp} = \left(\frac{G_{pp}}{\rho_a (\mathcal{A}_a)_D}\right)_f \tag{5.20}$$

and the corrected fluxes are

$$\phi_a^* = \phi_a + \frac{\upsilon_{pp}}{\alpha_{af} + \delta} |\mathbf{S}_\mathrm{f}| \nabla_\mathrm{f}^\perp \alpha_a \tag{5.21}$$

$$\phi_r^* = \phi_a^* - \phi_b \tag{5.22}$$

$$\phi_c^* = \alpha_a \phi_a^* + \alpha_b \phi_b \tag{5.23}$$

The solution procedure as used in twoPhaseEulerFoam is described in Figure 5.1. The solver employs the Weller pressure-velocity coupling with optional corrections for the dispersed phase volume fraction transport equation, or α-equation, within the PISO-loop. The equations of turbulence and the kinetic theory models are solved at the end of a time step as shown in Figure 5.1.

5.2.2. Initial Testing

There are number of tutorials in the official release of OpenFOAM. Promisingly for twoPhaseEulerFoam, two of these tutorials represent a small bubbling bed. The first tutorial, named “bed”, uses the particle normal force model and the second one, “bed2”,

the kinetic theory model for the particle-particle interaction. The packing limit is set $\alpha_{s,max} = 0.62$ in the kinetic theory.

In the tutorial "bed2" with the kinetic theory, the dispersed phase volume fraction quickly reaches unphysical, large values with the default parameters. This situation can be improved by setting $\alpha_{s,minFriction}$ to 0.5 as suggested by Johnson and Jackson (1987) in the frictional stress model. With this change the behaviour of the volume fraction is more stable, but the peak volume fraction, max (α_s), is consistently above 0.64 with values reaching up to 0.73. Reducing the time step to $5 \cdot 10^{-7}$ s did not eliminate the problem, but it did lengthen the simulation time considerably. Switching to the particle normal force model with a time step of 10^{-4} s eliminated the overpacking.

1. Solve the dispersed phase continuity equation (α-equation)
2. Construct the flux predictor, $\mathcal{A}_\varphi$
3. PISO-loop
    a. Predict fluxes
        i. Flux predictor, $\mathcal{A}_\varphi$
        ii. Buoyancy, explicit drag and granular phase apparent pressure
    b. Construct and solve pressure equation
    c. Correct fluxes
    d. Reconstruct velocities
    e. Correct α-equation
4. Correct substantive derivatives
5. Solve turbulence equations
6. Solve kinetic theory equations

Figure 5.1. *Diagram of the Weller (2002; 2005) solution procedure as found in twoPhaseEulerFoam.*

Similar results were obtained when attempting to simulate the pilot-scale CFB with the kinetic theory approach: The volume fraction exceeds the maximum packing limit set in the kinetic theory model. With the particle normal force model enabled – using parameters suggested by Gidaspow and Syamlal (1985) – and a short time step, ~10^{-6} s, the over-packing was avoided.

The reason the kinetic theory model fails to prevent over-packing is found in the implementation of the model. The volume fractions given as the input for the radial distribution model (Equations 4.32-3) are limited to $\alpha > \alpha_{s,max} - 0.01$ and the Johnson-Jackson (1987) frictional pressure model (Equation 4.44) implementation has a

built-in limiter for volume fractions higher than $\alpha > \alpha_{s,max} - 0.05$ in the denominator. The reason for the addition of these limiters is the explicit handling of the kinetic theory model. The radial distribution and frictional pressure models have a singularity at $\alpha = \alpha_{s,max}$ and they rise extremely rapidly near the packing limit. As the kinetic theory is only updated at the end of each time step, very short time steps are needed to avoid decoupling the kinetic theory and momentum equations. The strict limiters eliminate the excessive frictional and granular pressure values caused by the decoupling, but with limiters as strict as those implemented, the forces generated by the models are inadequate to prevent over-packing.

In contrast to the kinetic theory, the particle normal force is included as a diffusion term in the α-equation and is updated after every solution of the α-equation, instead of only once per time step. This more implicit implementation and non-singular behaviour of the model at $\alpha = \alpha_{s,max}$ allows longer time steps without the decoupling of the equations. However, the particle normal force model is very simple and is inadequate to model the complex particle-particle interactions in a CFB. In addition, even with the longer time step length achieved with the model, the computational times required for valid averages were still unfeasibly long.

Less strict limiters and linearization of the granular and frictional pressure models near the packing limit were experimented with, together with various adaptive time stepping schemes, but no satisfactory combination was found. The solids pressure's proportionality to the gradient of the particle phase volume fraction makes setting appropriate limiters difficult. The particle normal force has to be large enough to limit packing, regardless of the local gradient of the particle volume fraction. In the case of the pilot-scale CFB, even a time step of $2 \cdot 10^{-7}$ s was found to be too large and the computational time unfeasibly long. Clearly a better solution was needed.

5.3. Modified Solver

A number of modifications were introduced to the solver: firstly to eliminate the over-packing discussed in the previous section and to improve the general stability of the solver near the packing limit, and, secondly, to introduce additional physical sub models for the simulation of a CFB. Sections 5.3.1 and 5.3.2 concentrate on the handling of the packing limit and related stability issues, while sections 5.3.3-5 concentrate on the addition of new sub models.

5.3.1. Adaptive Under-Relaxation and Iterations within a Time Step

The first attempt to stabilize the solution of the α-equation was to introduce under-relaxation and iterations within a time step needed by an under-relaxed transient solver for converged, time-accurate results. The under-relaxation was implemented by weighting the coefficient matrix with a built-in OpenFOAM function. An adequate number of iterations is ensured by re-solving the equation on each correction loop, until the residual reaches a set limit. This limit has been set at 10^{-5} in most cases. If the residual is still below the set limit after a pressure-velocity correction, no further α-equation corrections are carried out on that time step.

As the level of under-relaxation required for convergence varies depending on the instantaneous flow field, an adaptive scheme was adopted for the under-relaxation factor. If – on each solution of the α-equation and within the same correction loop – the residual increases compared to the previous solution of the equation, the under-relaxation factor is reduced by 20 %. The factor is reset to the value chosen by the user at the beginning of each time step.

The under-relaxation improved the stability and the handling of the packing limit. However, uninterrupted simulation runs which were long enough for representative average fields still proved impossible with the kinetic theory model.

5.3.2. Handling of the Frictional Pressure

As the implementation of the particle normal force model offered benefits compared to the implementation of the kinetic theory, the obvious choice was to use a similar approach for the kinetic theory. The kinetic theory is a complicated model and updating the whole model after each solution of the α-equation would take too much computational time. Two kinetic theory sub-models are responsible for limiting the packing: the granular and frictional pressures. Of these, the frictional pressure only depends on the volume fraction field and it can be updated with a low computational cost. The granular pressure also depends on the granular temperature. At high volume fractions the dissipation of the granular temperature is high, which leads to low granular temperature values and makes frictional pressure the dominant term near the packing limit.

The flux corrections for frictional and granular pressure were separated from each other and the frictional pressure was added to the α-equation as a diffusion term as described in Equations 5.14-23. The only difference in implementation compared to the particle normal force model is that the powder modulus, G_{pp}, is replaced with frictional pressure modulus, G_{pf}, which is defined as

$$G_{pf} = \frac{dP_f}{d\alpha_s} \tag{5.24}$$

In practice, the equations used in particle normal force and frictional pressure models are quite similar being functions of the dispersed phase volume fraction which grow quickly as the volume fraction approaches the packing limit. A comparison plot of G_{pp} and G_{pf} , with different models suggested in literature, is shown in Figure 5.2. The major difference between the particle normal force model and the frictional pressure models similar to Johnson and Jackson (1987) is the existence of a singularity at the packing limit.

Together with the adaptive under-relaxation the modification reduced the tendency of the solver to over-pack, but at the same time it introduced a new problem: while the packing limit held for most of the time, the occasional decoupling of the equations caused "explosions" in the dispersed phase velocity field. Close to the packing limit, even small changes in the volume fraction field can cause very large increases in frictional pressure, which – due to the explicit treatment of the G_{pf} – can create extremely large instantaneous velocities once the frictional pressure model is updated and applied.

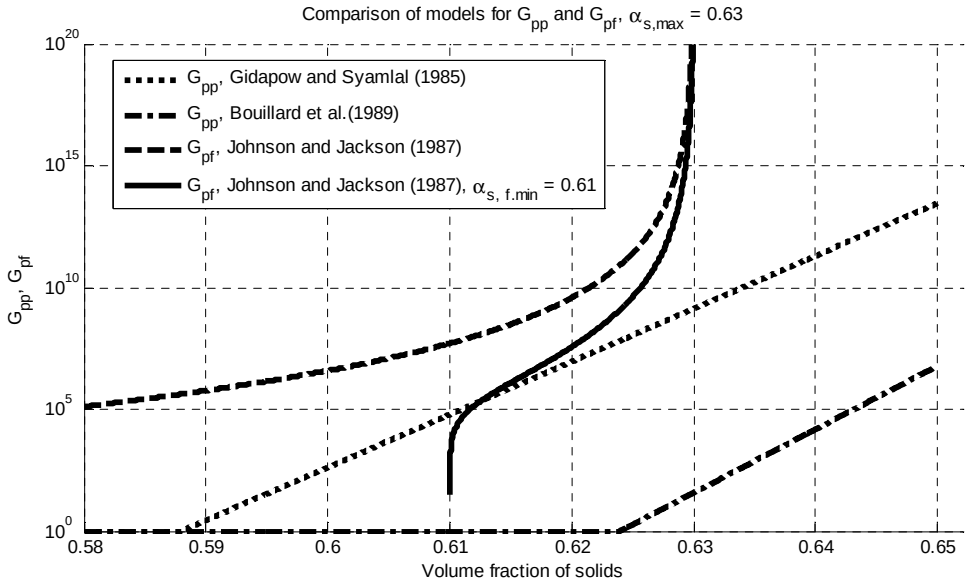

Figure 5.2. *Comparison of G_{pp} as suggested by Gidaspow and Syamlal (1985) and Bouillard et al. (1989) and G_{pf} as suggested by Johnson and Jackson (1987) and with modified minimum frictional volume fraction parameter.*

Depending on the magnitude of the unphysical velocities, the time step length and the under-relaxation factors used, the result is either a divergence of the solution due to

excessively large Courant numbers or an unphysical source of momentum. The problem is especially severe in tight geometries, because – with no room for the particle phase to expand into – even a slightly too large frictional pressure value may cause a chain reaction. The overestimated local frictional pressure pushes the volume fraction into adjacent cells which are already close to the packing limit, thus creating even higher frictional pressure values. Although the same problems apply to the particle normal force model, it is less sensitive to them because of the models used for the G_{pp}.

To eliminate the problem, a correction coefficient, C_{pf}, was introduced to the frictional pressure term. The C_{pf} is defined as the ratio (Equation 5.26) of the net flux of α_a into the cell caused by the corrected flux field (Equation 5.27) and the net flux of $\alpha_a$out of the cell due to the flux caused by the frictional pressure (Equation 5.28). The net flux in this case is defined as the sum of the cell face fluxes (Equation 5.29).

$$G_{pf}^{*} = C_{pf} G_{pf} \tag{5.25}$$

$$C_{pf} = \frac{\phi_{a,net,cell,in}^{*}}{\phi_{pf,net,cell,out}} \tag{5.26}$$

$$\phi_a^{*} = \phi_a + \frac{\nu_{pf}}{\alpha_{af} + \delta} |\mathbf{S}_\mathrm{f}| \nabla_\mathrm{f}^{\perp} \alpha_a \tag{5.27}$$

$$\phi_{pf} = \frac{\nu_{pf}}{\alpha_{af} + \delta} |\mathbf{S}_\mathrm{f}| \nabla_\mathrm{f}^{\perp} \alpha_a \tag{5.28}$$

$$\phi_{net,cell} = \sum_{cell\ faces} \phi \tag{5.29}$$

The C_{pf} is calculated for each cell separately based on the volume fraction field of the previous iteration and its magnitude is limited to 0.001...1. This treatment effectively limits the magnitude of the frictional pressure to such an extent, that it can prevent any additional packing but without causing a net flux out of the cell. Assuming the particles are hard this limitation is physically sound for frictional pressure. For granular pressure this would not be the case.

The introduction of the correction coefficient greatly improved the stability of the solver and eliminated the over-packing, as long as an appropriately chosen combination of the frictional pressure model and the under-relaxation factor are used. An adaptive time stepping set to maintain a maximum Courant number of 0.6-0.9 and α-equation under-relaxation factors in the range 0.2–0.4 – depending on the frictional stress model – have been used with good success. The modest increase in computational cost per solution

for the α-equation is easily outweighed by the faster convergence, longer time steps and uninterrupted simulation runs afforded by the improved stability.

5.3.3. Kinetic Theory

In addition to modifications needed to improve the speed and stability of the solution, small changes were made in other parts of the kinetic theory model. alternative Koch (1990) and Koch-Sangani (1999) models were added to the granular temperature transport equation (4.26) for the fluid turbulence production term. The divergence of particle velocity, $-\nabla \cdot U_s$, was added to the term for the granular temperature dissipation arising from inelastic collisions, according to Equation 4.37. For frictional stresses, the Srivastava-Sundaresan (2003) model was added. For particle phase velocity field and granular temperature field, Johnson and Jackson (1987) boundary conditions were added. The additions in this section are mostly based on the source code of Passalacqua (2008).

5.3.4. SGS-Models for Continuous Phase Turbulence

For the continuous phase turbulence, a filtered SGS-closure was introduced. The OpenFOAM 1.4 based source code of Passalacqua (2008) was used as an example while implementing the models. The models are implemented as a separate model library and can be added to any OpenFOAM solver. The library is very similar to the OpenFOAM built-in single phase SGS-model library, with only small differences in code structure and variable definitions.

5.4. Parallel Efficiency

To evaluate the feasibility of strong parallelization of the solver, a test of parallel efficiency was conducted. For the testing, a 3D mesh with 292542 elements of the pilot scale CFB geometry was created. The testing was done with two sets of computers: 5 x 4 processor core (5 x ProLiant DL145G2, 2 x 2.6 GHz, AMD Opteron) and 3 x 8 processor core (3 x ProLiant DL145G5 2 x 3 GHz, Intel Quad-Core Xeon) with gigabit Ethernet interconnects. For each datapoint, 0.05 s of simulated time was calculated with the same initial field, boundary conditions and solver settings.

OpenFOAM uses domain decomposition method for parallelization. The mesh is geometrically divided into smaller portions and each processor solves one of these portions. The adjacent portions, i.e. processor cores, are seen as boundary conditions. In the case of the pilot scale CFB, the domain was decomposed vertically into the required number of spaced portions.

The results of the tests are listed in Table 5.2. In the first set of 5 x 4 core 2.6 GHz AMD processors, reasonably good scaling was achieved using up to 16 cores, but almost no speed-up was gained by increasing the number of cores from 16 to 20. The probable cause of this is that the bandwidth of the gigabit Ethernet connecting each of the 4 core nodes became the limiting factor. The second set of 3 x 8 core 3 GHz Intel cores proved significantly faster overall and parallelization efficiency remained good over the whole tested range. These nodes are also connected with gigabit Ethernet but, as each node contains 8 cores, fewer Ethernet connections are needed. One interesting result is that a single 8 core node running only 4 threads is almost as fast as the same node running 8 threads, with much better performance per core. This suggests that the performance of the processors is limited by memory access bandwidth on the motherboard.

Overall the parallel efficiency was good and the results demonstrate the importance of memory and interconnect bandwidth for computational clusters used for CFD.

Table 5.2. *Parallel efficiency test results*

Processor cores			**Efficiency**	**Speed-up**	**Clock time for 1s of simulated time**
5 x ProLiant DL145G2, 2 x 2.6 GHz, AMD Opteron					
Ref.	1 x 4 =	**4**	100%	**4**	**62 h**
	2 x 4 =	**8**	99.0%	**7.92**	**31.3 h**
	3 x 4 =	**12**	89.3%	**10.7**	**23.3 h**
	4 x 4 =	**16**	85.2%	**13.6**	**18.33 h**
	5 x 4 =	**20**	70.5%	**14.1**	**18.05 h**
3 x ProLiant DL145G5, 2 x 3 GHz, Intel Quad-Core Xeon					
	1 x 4/8 =	**4**	166%	**6.6**	**21.4 h**
Ref.	1 x 8 =	**8**	100%	**8**	**17.6 h**
	2 x 8 =	**16**	97.2 %	**15.6**	**9.1 h**
	3 x 8 =	**24**	84.5 %	**20.3**	**7.0 h**

5.5. CFD-Modelling Setup

The pseudo-2D geometry of the pilot-scale CFB was partly chosen to enable comparison with two-dimensional simulations. The 2D-simulation allows for variations in of several model parameters without unreasonable computational costs, which would not be the case with 3D-simulations. However, the long averaging periods required mean that even the 2D-simulations take several days, even for simple averages.

The two-dimensional computational domain for simulation of the pilot scale CFB consists of a 0.4 x 3.0 m rectangle, representing the riser section, and a 0.3 m long tilted section of the solids return tube. The rest of the solids recirculation system – from the top of the riser to the loop seal – is not included in the domain. The computational domain together with the mesh is shown in Figure 5.3.

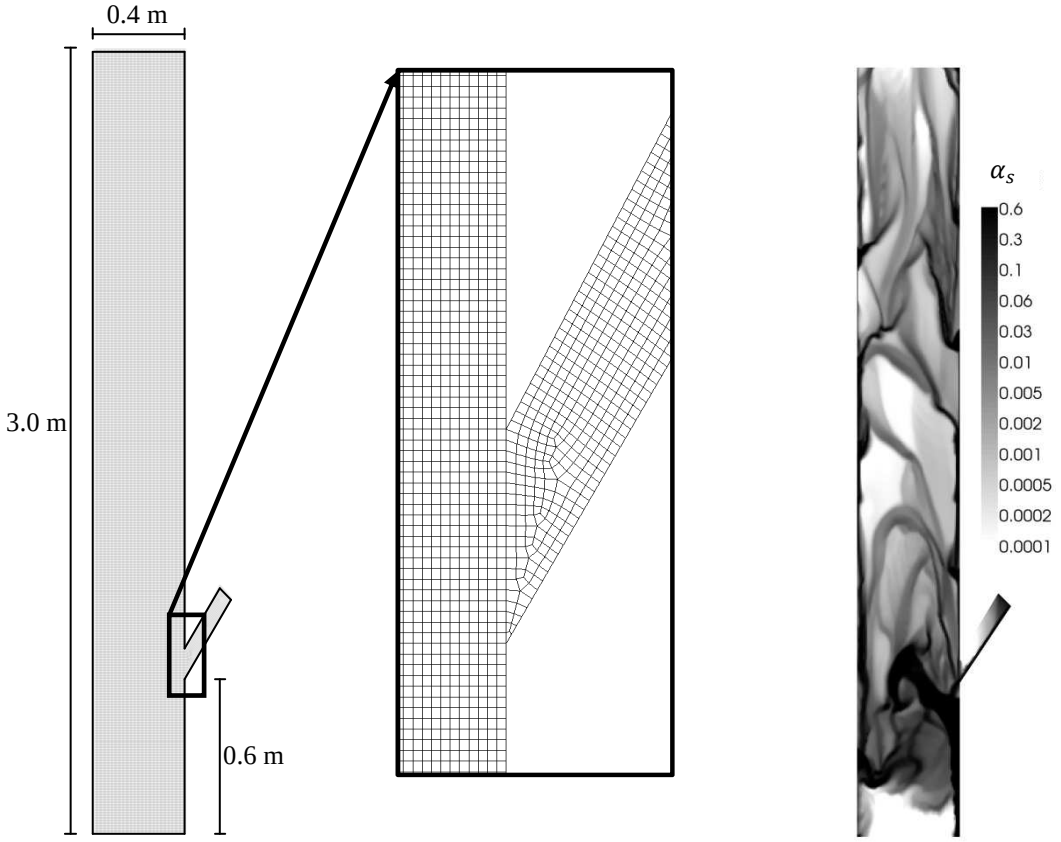

Figure 5.3. *Computational domain and mesh, together with the initial volume fraction field used to initialize the simulations. The initial field is obtained from earlier simulations.*

The solids return is modelled with a transient inlet boundary condition. It varies the particle phase inlet velocity magnitude between 0 and 0.7 m/s, trying to maintain a mean solids volume fraction of $\alpha_s = 0.069$ in the domain. This corresponds to 3.08 kg of glass beads in the riser section of the experimental device. The solids return inlet

volume fraction was set to 0.5, with zero velocity magnitude for air. The fluidization air injectors were modelled with a non-uniform velocity profile, Figure 5.4, for the fluidization air inlet. The profile was scaled to match the desired fluidization velocity. Ambient air properties were used.

For the simulations, a two-dimensional computational mesh with 48757 elements was created. The riser section has a hexahedral mesh, with square elements of 5 x 5 mm size, and the solids return tube has a quadrilateral unstructured mesh of similar resolution. A detail picture of the mesh at the connection point of the riser and solids return tube is shown in Figure 5.3. The models, parameters and boundary conditions used are listed in Table 5.3. Limited central differencing was used for all the convection terms, least-squares interpolation for the gradients and the implicit-Euler scheme was adopted for the time derivatives. All the selected schemes are – at least conditionally – second order accurate. More information on limited convection schemes can be found in the PhD thesis of Jasak (1996). Convergence criteria were set at a residual below 10^{-7} for pressure and 10^{-6} for other equations. An under-relaxation factor of 0.25 was used for the particle phase transport equation. The other equations were not under-relaxed.

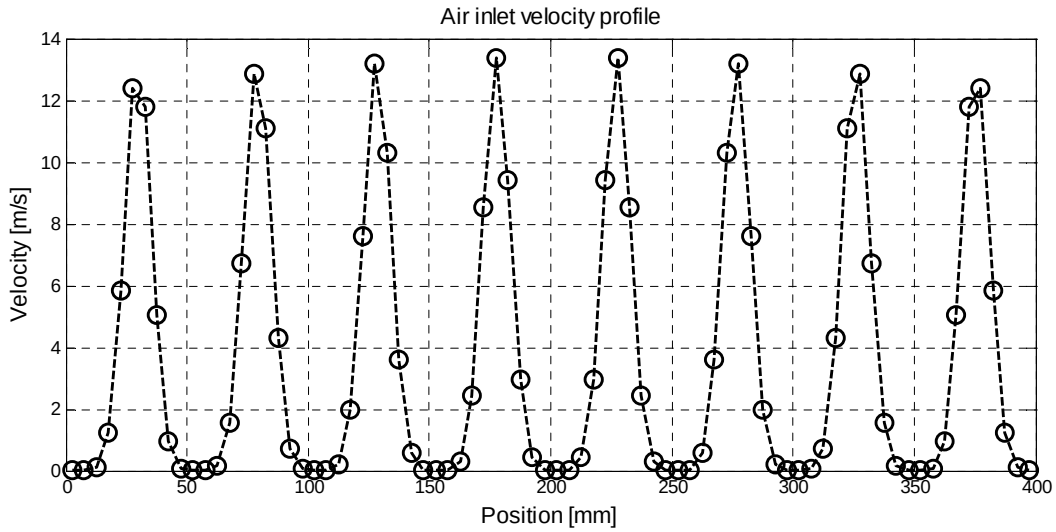

Figure 5.4. *The non-uniform velocity profile used to model the fluidization air injectors.*

Simulations were carried out in four different cases: with fluidization velocities of 3.25 m/s and 3.75 m/s and both with and without the Smagorinsky SGS turbulence model. Each of the simulations was initialized with variable fields from an earlier simulation and ran for 5 seconds of simulated time before the averaging was started. The initial volume fraction field is shown in Figure 5.3. The simulations were then run for a further 30 seconds to generate the average fields.

Table 5.3. *Physical models and boundary condition for the CFD-simulations*

Fluidization velocity	3.25 m/s		3.75 m/s	
Mean particle VOF, α_s	6,9%			
Particle diameter, d_p	442 μm			
Particle density, ρ_s	2480 kg			
Drag model	Gidaspow (1994), Ergun, Wen & Yu			
Gas turbulence model	none	Smagorinsky SGS, $C_s = 0.16$	none	Smagorinsky SGS, $C_s = 0.16$

Kinetic theory for granular flow: Transport equation			
$\alpha_{s,f,max}$	0.625	**Conductivity, κ_Θ**	Gidaspow
Coefficient of restitution, e_s	0.9	**Viscosity, $\mu_{s,kt}$**	Gidaspow
Granular pressure, $P_{s,kt}$	Lun	**Radial distribution, g_0**	Lun & Savage

Frictional stress:			
Model	Srivastava & Sundaresan	$\alpha_{s,f,min}$	0.61
Angle of internal friction, φ_f	28º	r	2
F	0.05	s	5

Boundary conditions:					
	u_g	u_s	α_s	p	Θ
Walls	[0,0,0]	Johnson & Jackson, $e_w = 0.8$, $\phi_{spec} = 0.2$	$\nabla\alpha_s = 0$	$\nabla p = 0$	Johnson & Jackson, $e_w = 0.8$, $\phi_{spec} = 0.2$
Outlet	$\nabla u_g = 0$	$\nabla u_s = 0$	$\nabla\alpha_s = 0$	$p = 0$	$\nabla\Theta = 0$
Air inlet	Non-uniform fixed value	slip	$\alpha_s = 0$	$\nabla p = 0$	$\nabla\Theta = 0$
Solids return inlet	[0,0,0]	Transient fixed value	$\alpha_s = 0.5$	$\nabla p = 0$	$\Theta = 0.001$

6. IMAGE-BASED MEASUREMENT METHODS

The easy optical access provided by the pilot scale CFB enables the use of image based measurement methods. High-speed imaging gives an excellent visualization of the structures of the particle phase and their interaction. Furthermore, if the recorded image frames have a short enough time delay between them, it is possible to calculate a two dimensional displacement field for the solid particles using *Particle Image Velocimetry*, PIV. PIV is a commonly used method in flow measurements. As the time delay between the frames is known, the velocity is easily calculated from the displacement. With adequate spatial and time resolution, as well as visibility, it is possible to use *Particle Tracking Velocimetry*, PTV, where individual particles can be detected and their velocity determined, possibly together with the size and other properties of the particles. The local void fraction can be estimated by correlating the recorded light intensity with the volume fraction of the particles.

6.1. Grey-Scale Volume Fraction Estimate

When particles in the riser are illuminated from behind and the light penetrating the suspension is recorded with a digital camera, it is possible to estimate the volume fraction of the particles from the intensity of the recorded light. Grasa and Abanades (2001) compared several correlation functions, and their calibration, and found out that a logarithmic function as presented in Equation 6.1 gives a good quality estimate, without the need for any fitting constants. In the Equation 6.1 I is the local mean light intensity, I_{max} and I_{min} are the light intensities obtained from calibration reference images and C is the concentration of the particles.

$$C = \frac{log \frac{I}{I_{min}}}{log \frac{I_{max}}{I_{min}}} \tag{6.1}$$

When this equation is applied to the backlit CFB images to determine the volume fraction of the particles it is written as Equation 6.2, where $\alpha_{s,ref}$ is the volume fraction of the particles at the minimum intensity reference, $I_{\alpha_{s,ref}}$and $I_{\alpha_{s,0}}$ is the light intensity corresponding with the zero particle volume fraction.

$$\alpha_s = \alpha_{s,ref} \frac{log\frac{I_{\alpha_{s,ref}}}{I}}{log\frac{I_{\alpha_{s,0}}}{I_{\alpha_{s,ref}}}} \tag{6.2}$$

Figure 6.1 shows a digital image of the CFB riser cross-section and the particle volume fraction field calculated by applying the Equation 6.2. The zero volume fraction reference intensity was determined from a time-averaged picture of the empty riser and the fully packed reference from the minimum intensities found in recorded datasets along with variations in the zero volume fraction reference. The local average intensity was calculated from a 64 x 64 pixel sample.

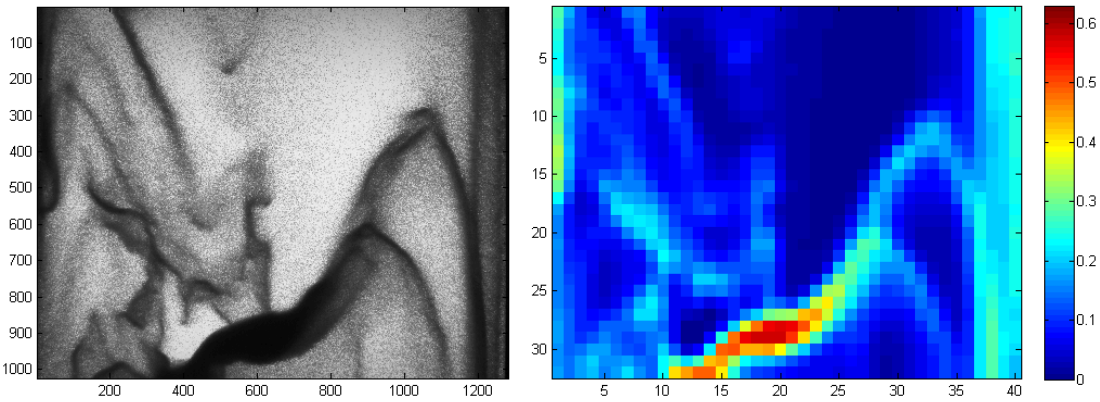

Figure 6.1. *Sample of a raw image of a section of the CFB riser and the volume fraction field calculated from it with Equation 6.2. The minimum intensity reference volume fraction is* $\alpha_{s,ref} = 0.63$ *in this example.*

The problems with this method are: the generation of an adequately powerful, evenly distributed backlight, the determination of the correct reference intensities with corresponding volume fractions and the inability to resolve volume fractions above the lowest volume fraction where the light penetrating the suspension can be reliably detected by the camera. In the case of the pilot-scale CFB, the highest measurable volume fraction was approximately 0.35 with fluorescent lighting. This limit is based on a comparison of the integrated grey-scale estimated particle mass with the actual mass of the bed material and comparison of results between the two light sources. As a result, the reference volume fraction was set at $\alpha_{s,ref} = 0.35$. These limitations should be kept in mind when interpreting the results. The absolute values may not be very accurate, but the results are useful for qualitative comparison between different portions of the riser and different fluidization velocities.

There is a significant underestimation of mean volume fraction at the bottom of the riser – where packed regions are commonly found – as the maximum measurable volume fraction is the reference $\alpha_{s,ref} = 0.35$. The maximum underestimation error in the mean volume fraction field can be evaluated by replacing all measured volume fractions

exceeding a limit set for reliable measurement, $\alpha_{s,meas} > \alpha_{s,valid} = \alpha_{s,ref} - \varepsilon$, where ε is a tolerance from the reference value. In the results, a tolerance of $\varepsilon = 0.02$ was used. A mean volume fraction field calculated from the modified volume fraction field represents what the mean volume fraction would be if all areas where the measured light intensity is less than the limit of reliable measurement are assumed to be fully packed, instead of having a volume fraction close to the reference value.

The major benefit of this method is that the volume fraction fields are recorded simultaneously with the velocity fields, which is vital for the calculation of volume fraction weighted averages, i.e. Favre averages, and Reynolds stresses in a multiphase flow. It would be beneficial to combine the grey-scale VOF estimate with another – more accurate – method to measure the mean volume fraction. The non-time resolved mean VOF-field could then be used to calibrate and validate the grey-scale estimate, and the VOF values given by the grey-scale estimate could be used as a weighting factor in the calculation of the derived quantities.

6.1.1. Light Intensity Correction

Any suitable light source can be used for the back lighting. However, common light sources connected to the alternating current electrical grid have tendency to pulse at the grid's frequency. If a pulsing light source, such as halogen or fluorescent is used the varying light intensity has to be compensated for. If uncorrected, the pulsing light source creates unphysical fluctuations in the calculated volume fraction field. The optimal solution would be to use matching reference images for each frame. However it proved difficult to consistently match the frequency and phase of the measurement and reference images.

In the mean light intensity graph in figure 6.2 of the whole frame, with a time resolution of 1/300 s, the high frequency fluctuations caused by the pulsing backlight can be seen clearly. If it is assumed that the mean light intensity, i.e. the bulk density, of the whole measurement window doesn't change much over a time period of 1/100 s the lighting related fluctuations can be removed by applying a 100Hz low-pass filter to the recorded intensity fields. With the measurement window over the whole width of the pilot scale CFB riser, this is a very reasonable assumption.

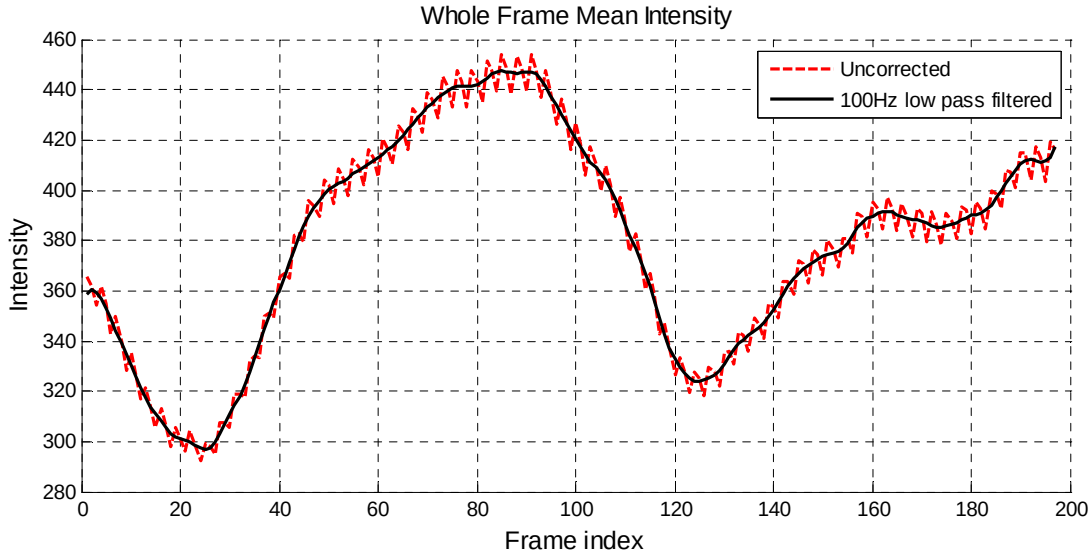

Figure 6.2. *Uncorrected and 100Hz low-pass filtered graph of whole frame mean light intensity with a time resolution of 1/300s.*

The low pass filter removes the unphysical fluctuation, but also reduces the time resolution of the measurement. The lost time resolution can be recovered by scaling the light intensity of individual frames so that the mean intensity of the whole frame matches the low-pass filtered mean intensity, and calculating the VOF-field from the scaled, unfiltered images. The unphysical fluctuations of the uncorrected images can be seen in the sample profiles of Figure 6.3. The variation between the frames is reduced in the corrected profiles and importantly, in the areas where there are differences, the changes are consistent with the order of the imaging sequence.

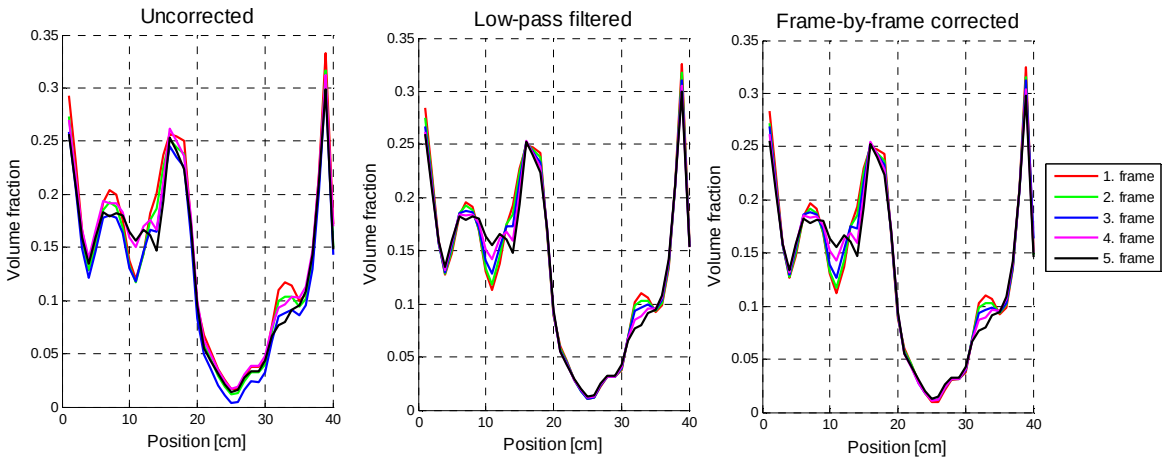

Figure 6.3. *A sample sequence of volume fraction profiles calculated from five consecutive uncorrected, 100Hz low-pass filtered and frame-by-frame intensity corrected images.*

6.1.2. Measurement of Cluster Size Distribution

As the glass beads appear as shadows in the recorded grey-scale image, it is possible to determine the sizes of the clusters and flow structures from the images. One way to do this would be to apply a grey-scale threshold value and gradient based segmentation to the image to detect and track the flow structures. While this is definitely possible to realize, problems may arise in the definition of cluster boundaries and tracking of the continuously deforming, string-like, structures. Another method for characterization of the local cluster size distribution would be to calculate a frequency power spectrum from horizontal and vertical cross-sections of the recorded images. However, the calculation of cluster sizes is beyond the scope of this thesis although it would be an interesting subject for further investigation.

6.2. Particle Image Velocimetry

When PIV is applied to the measurement of fluid flow, images of a flow seeded with small particles are recorded with a short time delay between individual frames. The images are then divided into smaller interrogation areas, and the interrogation area intensity fields are cross-correlated between the consequent frames. The displacement of the particles can be calculated from the displacement of the correlation peak. In fluid velocity measurements small seeding particles, with a small Stokes number, that consistently follow the fluid flow are used.

In gas-solid flow the solid particles are visible to the camera and their velocity can be measured similarly to the seeding particles used in traditional PIV measurements. In this case the measured velocities don’t represent the fluid velocity, but the local expected, most probable velocity of the particle phase in the measurement volume.

One problem with applying PIV to the particle phase velocities in a device such as the CFB is that the large particles do not travel with the surrounding fluid and, as such, don’t behave like a continuum. In dilute shear layers the particles occupying the same measurement volume may have large velocity differences – or even opposite velocities – without affecting each other significantly. In such areas, the statistical analysis of cross-correlation cannot determine a consistent particle velocity. Another limitation is the penetration of light in dense regions, which makes the use of a sideways light sheet impossible and also limits the maximum volume fraction where velocities can be determined with backlighting.

Interrogation areas used for the cross-correlation (CC) are typically squares with sizes ranging from 32 to 256 pixels, although other choices are possible. The choice of interrogation area size depends on the number of particles in the measurement volume,

the camera resolution and the desired spatial resolution. Overlapping interrogation area can be used to provide a denser results vector field but results still only represent the velocities in scales larger than the interrogation area size. The adjacent data points share a portion of the intensity field and thus are not independent from each other. The increased vector density however, helps with validation of the results.

Often some level of image pre-processing is applied to the particle images before the correlation. In the case of the backlit particle shadow images, they were inverted so that the particle shadows are seen as the intensity peaks, and locally normalized to even out the differences between the different particle volume fractions.

6.2.1. Cross-Correlation and Vector Calculation

Cross-Correlation (CC) is a commonly used method in signal processing in order to compare the similarity of two signals. When evaluating the similarity, it can be useful to compare the CC-result to the result of correlating the signal with itself. This is called Auto-Correlation (AC).

In PIV cross-correlation the intensity profiles, i.e. the signal of the corresponding K x L pixel interrogation areas of consequent image frames are correlated with each other, Equation 6.3. The displacement with the strongest correlation represents the most probable displacement for the particles in the measurement volume. In practice the correlation is calculated by applying Fast Fourier Transforms (FFT) with Equation 6.4 to speed up the calculation.

$$\boldsymbol{R}(x,y) = \sum_{i=-K}^{K} \sum_{j=-L}^{L} \boldsymbol{I}_1(i,j)\boldsymbol{I}_2(i+x,j+y) \tag{6.3}$$

$$\boldsymbol{R} = FFT^{-1}[FFT(\boldsymbol{I}_1) \circ FFT(\boldsymbol{I}_2)^*] \tag{6.4}$$

The correlation weakens towards the edges of the interrogation area, as smaller and smaller portion of the interrogation areas overlap. Thus, if the real displacement of the particles is large compared to the interrogation area, the correlation function will underestimate the displacement. This effect can be corrected by applying a weighting factor to the correlation field. Excessively large particle displacement can be compensated by offsetting the placement of the interrogation areas either by a known displacement, a known velocity, or by applying a multi-pass correlation algorithm. Multi-pass means the correlation is repeated multiple times and the results of the previous correlation are used to offset the interrogation areas for the next correlation.

With high speed imaging, the final result of the previous image pair can be used to provide the initial offset for the interrogation areas.

The accuracy of the displacement measurement can exceed the pixel resolution of the source images by fitting an interpolation function on the detected correlation maximum. This is called *peak fitting*. Usually the normal distribution, or a simplified parabolic approximation of it, is used as the fitting function. Most commercial PIV software use a three point fit, where only the points adjacent to the maximum are utilized for the fit. This method works well if the particles are small, i.e. in the range of 2-5 pixels, but accuracy reduces as the particle size increases because of the wider correlation peak of the larger particles. In fluidization experiments with modern digital cameras, particle images larger than this are commonly found. Dijkhuizen et al. (2007, p. 111-112) demonstrated how the accuracy with large particles can be improved utilizing more of the correlation field by applying a least squares fit. They found that with the least-squares fit, the accuracy of the peak detection only improved with increasing particle size.

6.2.2. Vector Field Validation and Post-processing

While the cross correlation algorithm used on PIV is generally quite robust, it can find non-valid correlation peaks due to camera sensor noise, lighting variation, out-of-plane particle movement and particle rotation, too long a time delay between the pictures or other problems in the imaging. These non-valid correlation peaks result in erroneous velocity vectors that have to be filtered from the results.

In this thesis four postprocessing steps were applied to the velocity fields calculated with the high speed PIV. Firstly the velocity vectors were validated by requiring that if the magnitude of the vector exceeds 0.1 m/s, its direction, Equation 6.5, has to be within ± 60º of the local median direction, Equation 6.6. This median is calculated from a 3x3x3 (x-direction, y-direction and time) 3D-sample.

$$\varphi = tan^{-1}\left(\frac{u_x}{u_y}\right) \tag{6.5}$$

$$|\varphi - \varphi_{median}| < \frac{\pi}{3} \quad \text{or} \quad |\varphi - \varphi_{median}| > 2\pi - \frac{\pi}{3} \tag{6.6}$$

Secondly, the change in the velocity magnitude between consecutive temporal measurement points had to be less than 3 m/s, Equation 6.7.

$$|\boldsymbol{u}_{t=i} - \boldsymbol{u}_{t=i+1}| < 3 \text{ m/s} \tag{6.7}$$

Thirdly, the deviation of the velocity vector had to be less than 1.6 times the local standard deviation from the local median velocity. The standard deviation and the local median velocity, Equation 6.8, were also calculated with a 3x3x3 3D-sample from the velocity field validated with the two previous steps.

$$|\boldsymbol{u} - \boldsymbol{u}_{median}| < 1.6\boldsymbol{u}_{RMS} \tag{6.8}$$

As the last post-processing step, the disqualified velocity vectors were interpolated by replacing them with a 3D local median velocity to preserve the correct velocity distribution in the results. If the local median sample included less than 9 valid velocity vectors, the interpolation was not carried out. Without this interpolation, the highest velocities would be under-represented in the velocity distribution as they are more prone to non-valid correlation results due to the larger displacements.

In the small scale, laser lit, non-high-speed measurements the quality of the raw vector fields was such that the vector validation and interpolation were considered unnecessary.

6.3. Particle Tracking Velocimetry

As particle tracking velocimetry concentrates on measuring the properties of individual particles, it not only has the highest possible spatial resolution but also all the measured quantities correspond with an actual particle, as opposed to the statistical approach adopted by PIV. In addition to velocity, simultaneous measurement of particle size, shape and the orientation of individual particles is possible, allowing multivariate analysis of the results. The viability of PTV as a measurement method depends on the reliable and accurate detection of particles and reliable matching of particle pairs in consecutive image frames.

Three basic approaches for image based particle size and velocity measurements are glare point velocimetry and sizing, GPVS; interferometric particle imaging, IPI; and shadowgraphy. Of these GPVS and IPI rely on the scattering of parallel coherent light beams from the surfaces of a transparent spherical particle. For both these methods the light has to be directed from the side at a non-orthogonal angle compared to the direction of the imaging. The main difference between the methods is that in GPVS the camera is focused on the measurement volume, while in IPI the camera is out-of-focus. With GPVS, the particle is seen as two light intensity peaks (glare points) and with IPI as an interference pattern. The spacing of the glare points and the interference pattern depend on the angle between the light source and the camera, as well as the size of the

particle. GPVS and IPI represent indirect imaging of particles, while shadowgraphy is a form of direct imaging. (Putkiranta 2007. p. 44.)

In shadowgraphy, the light is directed to the measurement volume from behind, and the particles create a shadow image on the camera sensor. The recorded images are then processed with an algorithm that can detect the particles and their edges from the recorded images. The strengths of shadowgraphy are its spatial resolution, its capacity to study transient phenomena and its applicability to a wide range of particle sizes and shapes (Putkiranta, 2007, p. 39). The density of particle suspension in the pilot scale CFB means that penetration of light is often the limiting factor for image based methods. Given the pseudo-2D geometry of the device and the non-uniformity of the particle suspension, the shortest suspension penetration depth for light is achieved with backlighting. This – together with limited transparency of the glass beads – makes shadowgraphy the method of choice.

6.3.1. Particle Detection in Shadowgraphy

For the backlit grey-scale shadowgraphy images, two basic particle detection approaches can be used. If it is possible to define a typical intensity profile, i.e. a particle mask for the particle to be detected, the intensity profile can be correlated with the recorded images, and the correlation peaks are detected as particles. This method is called particle mask correlation, PMC. The benefits of this method are that it is algorithmically simple and robust. The downside is that unless the particles are uniformly shaped and sized, multiple masks have to be used, which increases the computational cost of the analysis. Size distribution measurements also require a number of masks to be used, as the size measurement requires a mask for each measured particle size range.

The other method is based on the detection of particle edges from the images. The edges can be detected by thresholding the grey scale values of the image or by detecting the peak grey-scale gradient magnitudes. The maxima of grey-scale gradient magnitude in shadowgraphy is located on the edge of the particle shadow, although there are still uncertainties in the sub pixel location of the edge. For the particle size distribution measurement, a two-step algorithm similar to the one used by Putkiranta (2007) for spray characterization was chosen. In this algorithm, the image is first segmented with a constant grey-scale threshold. Then the segmented area is enlarged by 4 pixels and the magnitude of the grey-scale gradient is calculated for the segmented area. A threshold with a chosen value in then applied to the gradient magnitude values, thus isolating the focused edges of the particle. The mean grey-scale value of the focused area is set as the new threshold value, optimized individually for each particle, and the area is re-segmented. (Putkiranta 2007. p. 44.)

Sub-pixel accuracy for the edge detection is achieved by an interpolation routine in the form of ellipse fitting. The sub-pixel location of the perimeter is found with a low-pass FFT-filter as shown by Honkanen and Marjanen (2007). Overlapping object recognition to eliminate ellipses fitted over several near-by particles is carried out based on the perimeter curvature as described by Honkanen and Marjanen (2007).

6.3.2. PTV algorithm

While the measurements for the results shown in Figure 2.3 were obtained with stationary particles, the same particle detection algorithm can be applied to images recorded in the dilute areas of the pilot scale CFB riser. To determine the velocity of the particles, the detected particles from consecutive frames have to be matched correctly. Such matching is achieved by comparing particle sizes and locations based on an initial guess for the velocity. In the case of the water jet measurements conducted by Putkiranta (2007), determination of the initial guess velocity is relatively straightforward, as the flow has a clear mean flow direction i.e. temporal velocity fluctuations are small compared to the droplet mean velocity. In a CFB riser it is impossible to define a constant initial velocity guess which would be valid for particle matching, as the magnitude of instantaneous velocity fluctuations is often larger than the magnitude of the flow mean velocity. However, a very good initial guess for the particle velocities can be obtained by first calculating a PIV velocity field for each image pair and then using that result as the initial guess for the PTV particle matching. The good initial guess also acts as an efficient validation step, as only detection pairs closely following the PIV velocity field are accepted as valid. However, the validation fails if the random motion of particles is large compared to the local mean displacement given by PIV.

6.3.3. Application to the Pilot Scale CFB

The major limitation of shadowgraphy PTV when applied to the pilot scale CFB is that it can only be used in the dilute areas. As the volume fraction of the particle phase increases, the detection of individual particles quickly becomes challenging, or even impossible. Another issue concerns the particle size measurements. To penetrate as dense a suspension as possible, a powerful light source has to be used, which – with the cameras used in this thesis – inevitably leads to overexposure in areas with no particles. The overexposure causes an underestimation of the particle diameter as this depends on the focal sharpness of the particle.

If absolute measurement of particle sizes is needed – instead of just comparing the particle size in different portions of the CFB – a correction function for the measured particle diameter is required. A calibration study was conducted using calibration plate

PS20 (manufactured by PYSER-SGI) which has circular dot sizes from 3.5 μm to 1.2699 mm. Reasonably good results were achieved by correcting the measured diameter based on the mean grey-scale gradient of the particle perimeter, $|\nabla I_p|$. The correction function is of the form presented in Equation 6.9, where d^* is the uncorrected particle diameter, $|\nabla I_{ref}|$ is a reference grey-scale gradient for a perfectly focused particle, Δ_x is the image scale (length unit per pixel) and C_f, C_d and n are constants that have to be determined by calibration for each measurement setup.

$$d_p = \left(\frac{\overline{|\nabla I_{ref}|}}{\overline{|\nabla I_p|}} \right)^n C_f \Delta_x + C_d d^* \tag{6.9}$$

The results of applying the Equation 6.9 with $C_f = 2.4$, $C_d = 1.003$ and $n = 0.5$ to the calibration plate dot size measurements are shown in Figure 6.4. The large depth of field (15 mm) needed to cover the depth of the riser causes a projection error that depends on the size of the measurement window, the focal length of the lens used and the size of the camera sensor. With a 34mm measurement window and 105mm focal length lens on the ImperX Lynx 2M30 with a 11.8 x 8.9mm CCD-sensor, the projection error is ±3%. If a symmetrical distribution of particles in the riser is assumed, the projection error does not affect the measured mean diameter, but it does widen the measured size distribution. Sub-pixel accuracy is generally achieved, but the relative error increases for particles of less than 20 pixels in diameter.

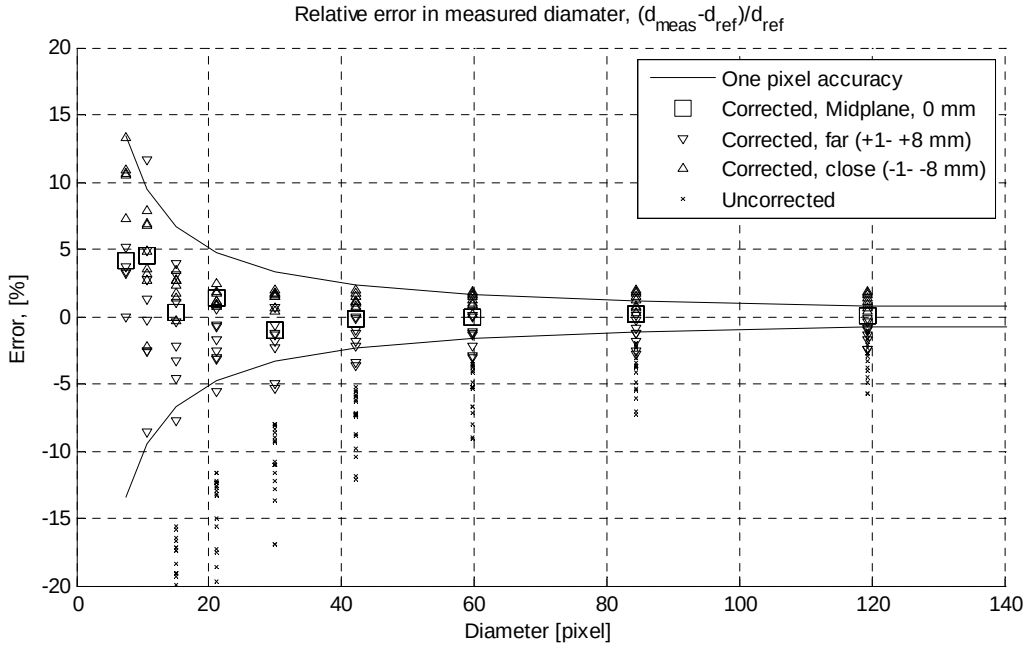

Figure 6.4. *The measured diameter correction function, Equation 6.9, applied to measurement of calibration plate dot size.*

The measured particle diameter and grey-scale gradient values can also be used to determine the location of the particles in direction normal to the measurement plane by comparing them with the depth-of-field (DOF) of the imaging setup. The DOF based segmentation of particle location will not be nearly accurate enough for the determination of the third velocity component, but it should allow statistical separation of particles located near the walls and in the middle of the channel. Such study would be important to determine how much the three-dimensionality of the flow in the pilot scale CFB affects the measurement results. The segmentation could also be used to isolate the projection error from the measured size distributions. The problem with both the the diameter correction and DOF segmentation is that a careful calibration is needed for each measurement setup, and they are still only applicable in the dilute regions of the CFB riser.

In principle PTV is the most accurate and detailed method for the measurement of particle properties. It allows direct simultaneous measurement and matching of several particle qualities: velocity, location (in three dimensions with focus segmentation), size, shape and orientation (rotation) for non-spherical particles. However, successful detection and matching of particles places great demands on image quality and detection algorithms. The complex algorithms mean that the computational cost of the analysis can be significant, especially with the long unsteady timescales of the CFB. The unsteady behaviour and wide range of volume fractions further complicates application PTV to CFBs. Despite these challenges, accurate measurement of particle velocities and sizes in the dilute regions of the pilot scale CFB is possible with the algorithms and methods presented in this chapter.

6.4. Measurement of Small-Scale Random Motion

As explained in section 4.3, Granular temperature, Θ, is defined as the energy of small-scale random velocity fluctuations of the particle phase, or one third of the mean square of the particle velocity, Equation 4.19. This random movement is an important parameter in kinetic theory based particle-particle interaction models.

The direct method of measuring the granular temperature is to measure the velocity of individual particles in the measurement volume in the same way as with the PTV-method described in section 6.3; and then use the results to calculate the granular temperature. If reliable PTV has been accomplished, this direct calculation of the granular temperature is obviously the best method. However, the same limitations as with the PTV velocity measurement apply: the method requires high spatial resolution; it is computationally relatively slow; and reliable detection and tracking of the particles is algorithmically challenging – especially when dealing with non-dilute suspensions.

Another option is to apply a cross-correlation based, statistical approach as suggested by Dijkhuizen et al. (2007). With this method a statistical variance of the particle movement in scales smaller than the PIV interrogation area is directly calculated from the variation in the PIV correlation peak width between auto- and cross-correlations. This method allows measurement of the random motion of particles on scales below the spatial resolution of PIV. The results can be combined with velocity variance calculated from a suitably filtered velocity field to describe the energy of the random motion below a desired spatial scale.

If all the particles in the measurement volume have the same uniform velocity, U_0, the position of a particle relative to the other particles will be exactly the same in consecutive image frames recorded with a small time delay, Δt. The whole particle pattern however, will shift a distance, $\Delta x = \Delta t U_0$, corresponding with the velocity of the particles and the length of the time delay. When two of these images are cross-correlated, the correlated peak is displaced by Δx and the width – or the variance of the normal distribution function fitted on the correlation peak – is the same as it would be if one of the frames were to be auto-correlated i.e. correlated with itself.

The vertical and horizontal component of random particle displacement in the interrogation area can be evaluated with Equation 6.10, where σ_d is the standard deviation of particle displacement. σ_{CC}, σ_{AC} are the standard deviations of the Gaussian distribution function fitted on the correlation peaks. As the width of the auto-correlation peak can be different for the first and second frames, σ_{AC} is defined as the mean of the first and second frame values, Equation 6.11. (Dijkhuizen at al., 2007, p.110)

$$\sigma_{d,i}^2 = \sigma_{CC,i}^2 - \sigma_{AC,i}^2 \ , \quad i = x, y \tag{6.10}$$

$$\sigma_{AC} = \frac{\sigma_{AC,1} + \sigma_{AC,2}}{2} \tag{6.11}$$

Dijkhuizen at al. used white spherical particles on a black background, which create an approximately Gaussian intensity profile in the recorded images. When an image of particles with Gaussian intensity distribution with standard deviation σ_I is correlated the result is a Gaussian correlation field with a standard deviation of $\sqrt{2}\sigma_I$. (Dijkhuizen at al., 2007, p.112.) In the case of the shadow images of the glass beads used in the pilot scale CFB, their intensity profile is obviously not Gaussian, as can be seen in Figure 6.5, but more of a toroidal shape. However, the profile from the centre to the edge of the particle shadow is approximately Gaussian and the $\sqrt{2}\sigma_I$ relation can be regarded as a reasonable assumption. Thus the Equation 6.12 is used to calculate the standard deviation of the particles in the interrogation area. However, it should be noted that for overlapping particles the assumption of Gaussian intensity profile no longer holds good.

$$\sigma_{d,i} = \sqrt{\left(\frac{\sigma_{CC,i}}{\sqrt{2}}\right)^2 - \left(\frac{\sigma_{AC,i}}{\sqrt{2}}\right)^2} \ , \quad i = x, y \tag{6.12}$$

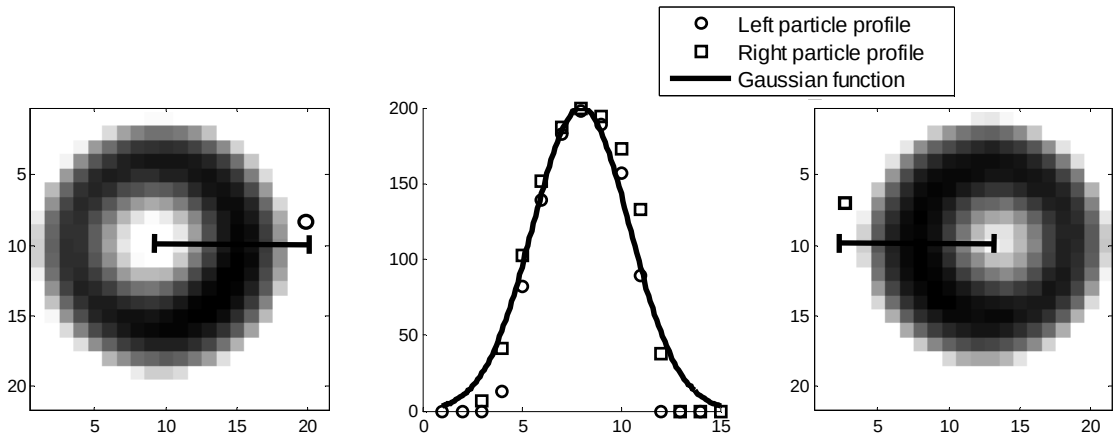

Figure 6.5. *Typical single particle intensity profiles with pulsed light imaging and a comparison with Gaussian function.*

The correlation calculations were carried out in the frequency domain by applying FFTs. Samples of auto- and cross-correlation fields, as well as the fitted normal distribution functions are shown in Figure 6.7.

6.4.1. Implementation in MATLAB

For use with the pilot scale CFB the correlation peak width based method was implemented in MATLAB (The MathWorks, Inc), together with PIV interrogation area mean displacement calculation. The basic procedure for the calculation is:

1. Load an image pair.
2. Parse the images to interrogation areas with a given initial shift.
3. Load an interrogation area pair
4. Invert and normalize the interrogation areas.
5. Calculate AC for both frames and CC.
6. Find the CC-field maximum.
7. Least-squares fit normal distribution on CC and AC maximum to locate the peak.
8. Validate the fitting.
9. Calculate mean displacement.
10. Calculated random displacement, Equation 6.11.
11. Repeat from 3.
12. Repeat from 1.

The Initial shift can be an expected mean velocity profile or an earlier PIV velocity field in multi-pass calculation. In this thesis, a velocity field calculated with LaVision Davis 7.2 (*LaVision* GmbH, Göttingen, Germany), a commercial PIV-software, was used to provide the initial shift.

The inversion and normalization of the images was carried out by consecutive application of Equations 6.13-16, where I is the intensity matrix and $I_{localMean}$ is the local mean intensity – calculated by resizing the image twice with bicubic interpolation. Thresholding with the local mean intensity is used to improve the correlation at high volume fractions, where very little light penetrates the suspension. Although the source images had very little noise, median filtering with a 3x3 kernel was carried out as a noise-reduction procedure. A sample of an interrogation area before and after inversion and normalization are shown in Figure 6.6. As can be seen from the sample **B**, the normalization and thresholding can reveal a signal in quite dark regions. The correlation results and the fitted normal distribution functions in Figure 6.7 show that the darkness of the source image has little effect on the cross-correlation. Of course, if the signal is completely non-existent, as is the case in fully packed areas of the pilot scale CFB and areas with no particles, the correlation cannot work.

$$\boldsymbol{I} = I_{max} - \boldsymbol{I} \tag{6.13}$$

$$\boldsymbol{I} = \boldsymbol{I} - I_{min} \tag{6.14}$$

$$\boldsymbol{I} = \max(\boldsymbol{I}, \boldsymbol{I}_{localMean}) - \boldsymbol{I}_{localMean} \tag{6.15}$$

$$\boldsymbol{I}(x,y) = \frac{\boldsymbol{I}(x,y)}{I_{max} - \boldsymbol{I}_{localMean}(x,y)} \tag{6.16}$$

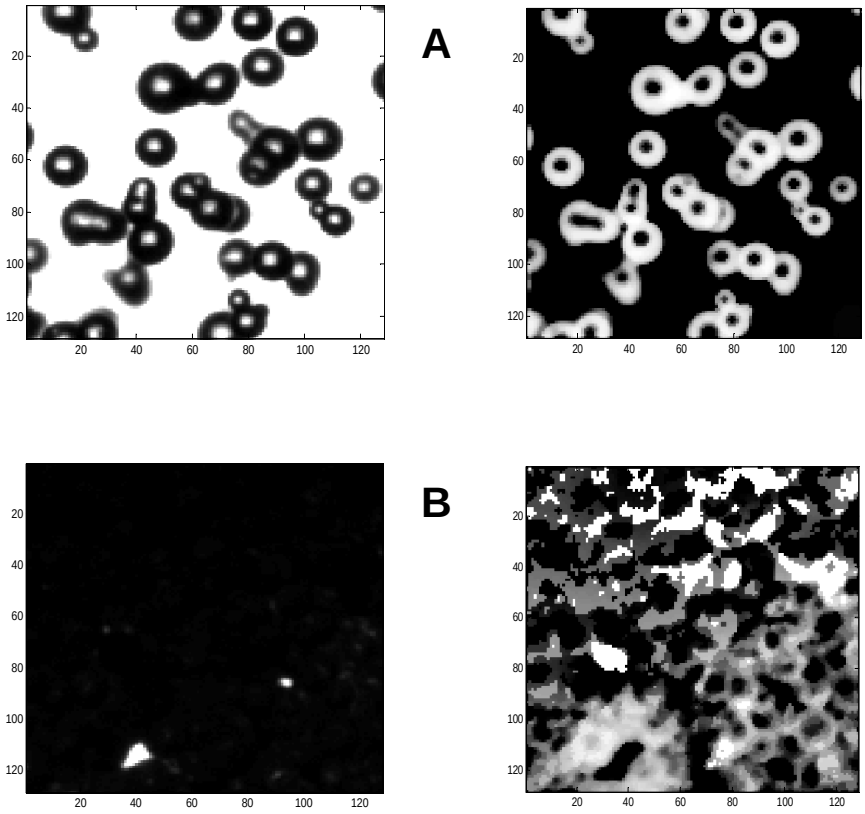

Figure 6.6. *Samples of original and inverted and normalized interrogation areas at different particle volume fractions.*

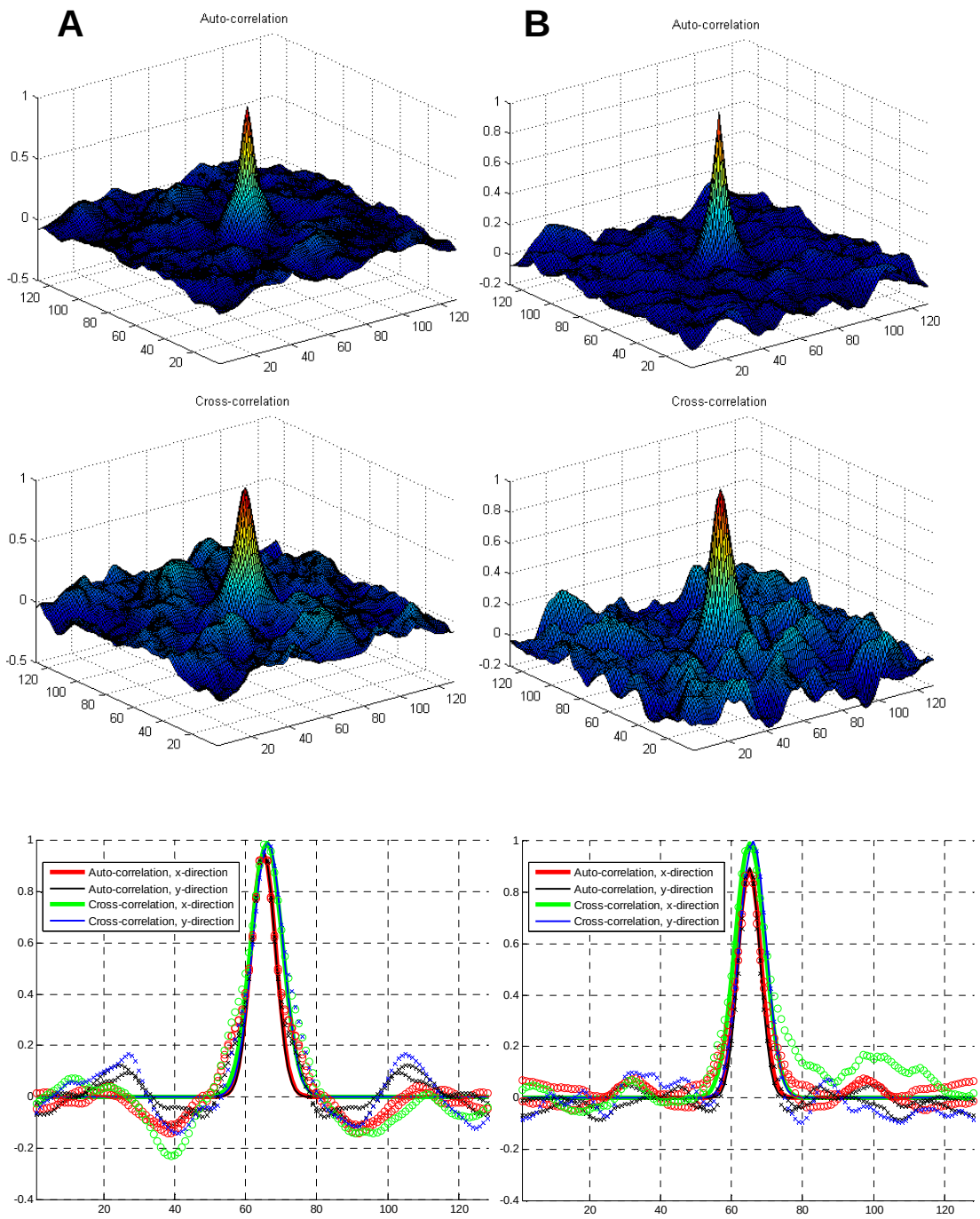

Figure 6.7. *Auto- and cross-correlation fields and the fitted normal distribution functions for the interrogation areas* **A** *and* **B** *shown in Figure 6.6.*

6.4.2. Testing and validation

For testing and validation of the method and implementation, a MATLAB function to generate synthetic particle images was written. The function generates a grey-scale image with the desired resolution, particle count, particle mean displacement and a random displacement along with normal probability distribution and a desired standard deviation. 20 different single particle intensity profiles which were isolated from actual measurement data are used to simulate the particles. Samples of the generated synthetic particle images with differing particle counts are shown in Figure 6.8. The profile and location of each particle is chosen randomly and independently of each other. Particles were added one-by-one by multiplying the chosen location of the existing intensity matrix by the ratio of the particle profile and the maximum intensity. With such a method, overlapping particles affect the measured intensity profiles, as is the case in the real measurement images.

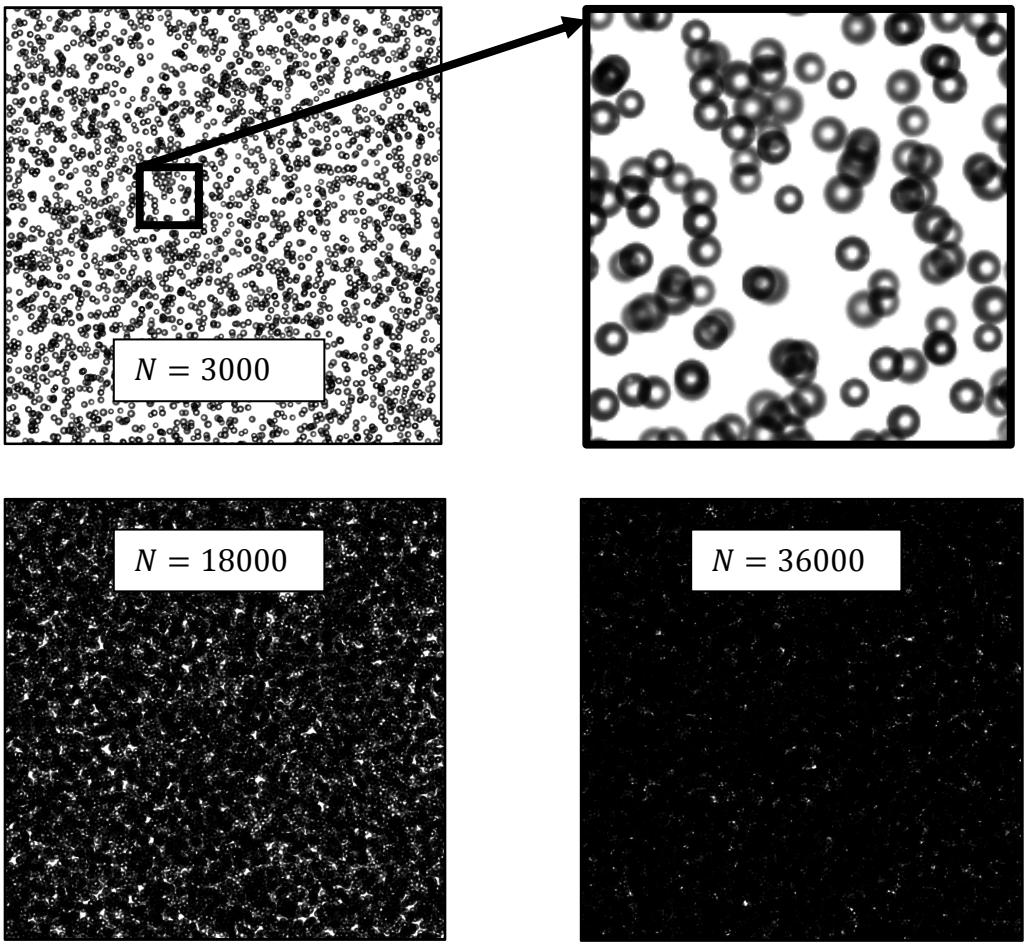

Figure 6.8. *Samples of synthetic 1000 by 1000 pixel particle images with particle counts of 3000, 18000 and 36000.*

Synthetic images of 1000x1000 pixels were generated with a particle mean displacement of 10 pixels both vertically and horizontally, and varying particle counts, 3000-36000, and particle displacement standard deviations of 0-6 pixels. The image sets were first analyzed with DaVis 7.2 using two correlation passes and an interrogation area of 128x128 pixels with a 50% overlap. A third correlation pass was carried out with the Matlab implemented PIV function that includes sub-interrogation-area scale particle random motion calculation based on the correlation peak width.

The results in Figure 6.9 show that the accuracy of the mean displacement proved to be excellent, even with the three-point peak fitting algorithm employed by DaVis, while the MATLAB implemented PIV function showed a slight improvement both in mean and standard deviation values. The improvement is explained by the additional correlation pass, the least-squares peak fit and differences in particle image inversion and normalization. Overall these differences are minor.

Of course the interesting part of the results is the sub-interrogation-scale motion results. With particle standard deviations of less than two pixels the measured values match the reference values closely. At a standard deviation of three pixels the measured value is slightly below the reference value. However, as the random component of the particle displacement is increased up to six pixels, the measured values level off at 3.6 pixels. At the same time, the standard deviation of the PIV displacement field – which represents the motion of particles in scales larger than the interrogation area size – increases, despite the measured mean displacement remaining correct and unchanged.

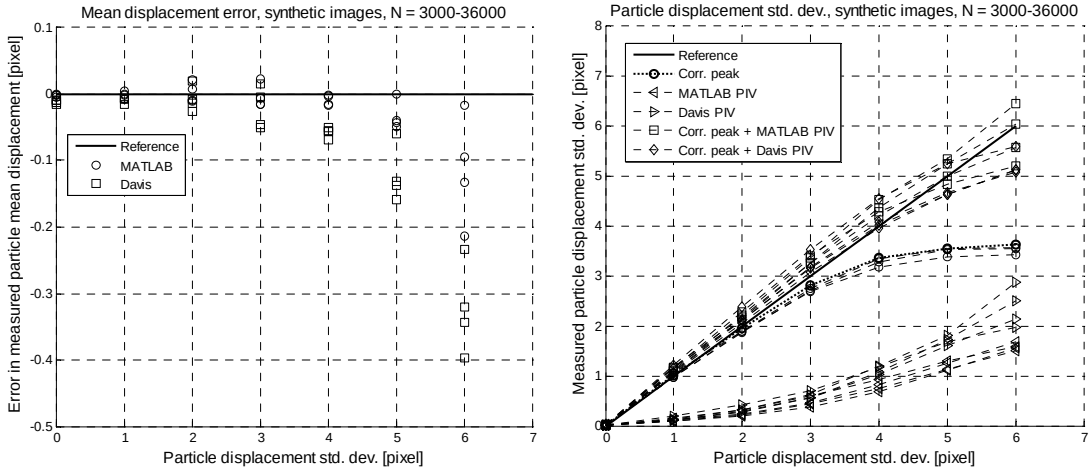

Figure 6.9. *Comparison of measured mean displacement and standard deviation values with reference values of the synthetic images. Includes PIV velocity fields calculated in DaVis 7.2 and Matlab, together with sub-interrogation-area scale random motion calculated from the MATLAB PIV-correlation results.*

There are at least two different mechanisms that can explain the above behaviour. Firstly, as the standard deviation of the particles increases, an increasing portion of the random particle motion can be seen in scales larger than the interrogation area size. This mechanism represents the physical scale difference of the motion and the measurements. Secondly, as the random particle motion increases it becomes increasingly difficult for the PIV-algorithm to detect the correct correlation peak, and the number of detected displacements decreases, the random error of the method increases, which explains the increase in the standard deviation of the measurements. The PIV-algorithm tries to find the displacement that has the best correlation, meaning the sharpest correlation peak, so it naturally favours areas with lowest levels small scale random movement, explaining the lowest levels of small scale random motion.

Which – if either – of these mechanisms dominates the behaviour is unknown. If it is the first one, the method can be said to be valid as long as the mean displacement calculation succeeds. If it's the second one, the method is only valid up to standard deviation of less than three pixels. The strong correlation between the sum of the standard deviations of PIV and the sub-interrogation-area scale displacements with the reference values suggests the first option is the dominant mechanism.

The effect of the possible rotation of asymmetrical particles and a velocity component in the direction normal to the measurement plane was evaluated by randomly choosing the particle profile for each particle in the second frame of the synthetic image pair. These images represent a situation where non-spherical particles are randomly displaced over the whole depth, 15 mm, of the riser. As a result, the PIV displacement measurement was not significantly affected, but the correlation peak method gave a standard deviation of ~0.9 pixels with no random motion. At reference std. deviation of one and above pixels, the values were overestimated by 0.4 and 0.2 pixels respectively. In reality this is a worst case scenario. Typically, the vertical displacement of particles between the consequent image frames is less than 1.5 mm, and the horizontal one less than 0.5 mm. It is reasonable to assume that displacements in the riser in the direction normal to the measurement plane are even less. That would mean that the displacement is much smaller than the ~7 mm in the synthetic images and that the effect of the third velocity component on the standard deviation measurement is insignificant.

The method also displayed significant variations around the measured mean value, and it is recommended that a degree of local averaging or median filtering is applied to the results. The variations increase as the particle density decreases and as the statistical sample becomes smaller. It is recommended that the method is only applied to interrogation areas with more than ten particles, depending on the level of randomness in the motion of the particles. For these low particle-density areas PTV and direct calculation of particle random motion could be applied. It would be possible to write an algorithm that automatically chooses between CC-peak based and direct measurement

methods based on the particle density and the quality of the cross-correlation. Implementation of such an algorithm is however outside the scope of this thesis, but has potential for further research.

It should also be remembered that the measured particle standard deviation includes all the particles in the measurement volume and the results include both the small scale random motion and possible mean velocity gradients. With shadowgraphy the measurement volume covers the whole depth of the riser and it is very possible that overwhelming proportion of the measured particle standard deviation is caused by mean velocity gradient across the depth of the riser. In this case the measured value is more representative of the three dimensionality of the flow, instead of the random particle fluctuations as defined in kinetic theory.

6.5. Measurement Setup and Sampling

For comprehensive results, the measurements were divided into two categories with differing imaging setups. The first setup used high-speed single frame imaging, a measurement window over the whole width of the rise and a continuous fluorescent backlight illumination. These measurements provide time-resolved visualization, and with the application of PIV and grey-scale VOF estimate, provide a good overall characterization of the flow in the CFB riser. Nevertheless, there is room for improvement in the spatial resolution, the quality of lighting and the sampling. The amount of data generated by the high speed imaging places constraints on what can be analyzed with reasonable time and computational costs.

More accurate and detailed data is captured with the second setup. Here the illumination is provided by a pulsed laser and time-resolution is sacrificed in exchange for longer sampling periods. With this setup the measurement window size is limited to approximately 40 mm. This means that only a small portion of the riser can be covered with reasonable effort. The sampling positions and periods are presented in Figure 6.10. At the height of 155-160 cm a structural support prevents optical access.

Continuous Light	
Height [cm]	**Sampling period [s]**
6-38	28
25-57	28
50-82	28
75-107	28
100-132	28
125-157	28
160-192	28

Pulsed Light	
Height [cm]	**Sampling period [s]**
20	3 x 200
40	10 x 200
80	10 x 200
120	10 x 200

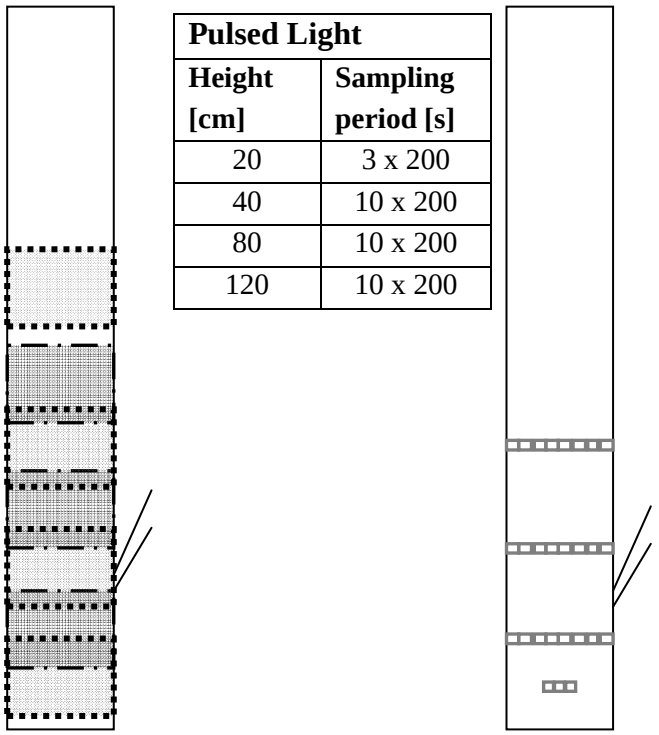

Figure 6.10. *Measurement windows and sampling periods used for each fluidization velocity in continuous and pulsed light source measurements.*

6.5.1. Continuous Light Source

To get a larger measurement area than the available laser could provide, high frequency fluorescent tubes were used to provide the backlight. The fluorescent tube stack and diffuser can be seen behind the CFB riser section in Figure 6.11 and a sample frame recorded with this setup is shown in figure 6.12, together with the corresponding particle velocity vector field. A continuous light source means that the single frame imaging mode has to be used to achieve a controlled exposure with the camera used. As the minimum time delay between the images is now limited by the maximum recording frequency of the camera, the measurement window size has to be scaled according to the relative displacement of the particles in the images.

Figure 6.11. *Continuous lighting setup. The CFB riser and loop seal lit by a pack of high frequency fluorescent tubes.*

For good average fields, the data has to be collected over a long period of time owing to the unsteady nature of the CFB. Based on preliminary measurements and CFD calculations, it was estimated that ~30 s worth of data would be needed for adequate average fields. The camera, LaVision ImagerPro HS, is capable of recording up to 638 single frame images per second, but it was decided that 300 Hz imaging frequency gives a reasonable compromise between a sufficiently small relative displacement of the particles, the sampling period and the amount of data to be analyzed. 8400 images with a resolution of 1280x1024 pixels were recorded per riser height and fluidization velocity, which gives a sampling period of 28s. A Nikkor 50mm f/1.2 lens was used on the camera.

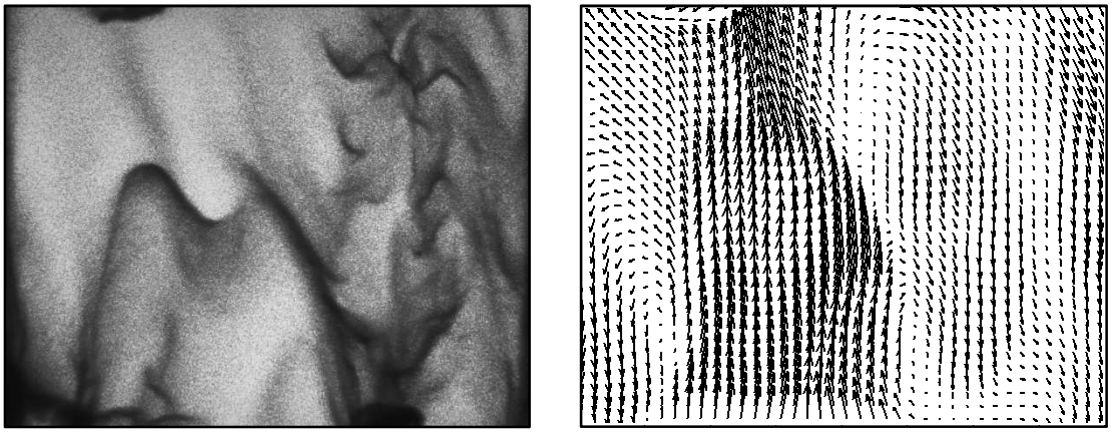

Figure 6.12. *Sample image recorded with continuous backlight and velocity vectors calculated with PIV.*

6.5.2. Pulsed Light Source

To control the exposure in the double frame mode of the camera, a pulsed light source is needed. For PIV, a pulsed laser is normally used to create a laser sheet perpendicular to the imaging direction. However, in the case of the CFB this is impossible, as the light sheet wouldn't penetrate the suspension deeply enough, and - in the case of the current experimental CFB - the access from the side is blocked by the CFB frame structure. Due to these limitations, the light can only be directed from the front or the behind.

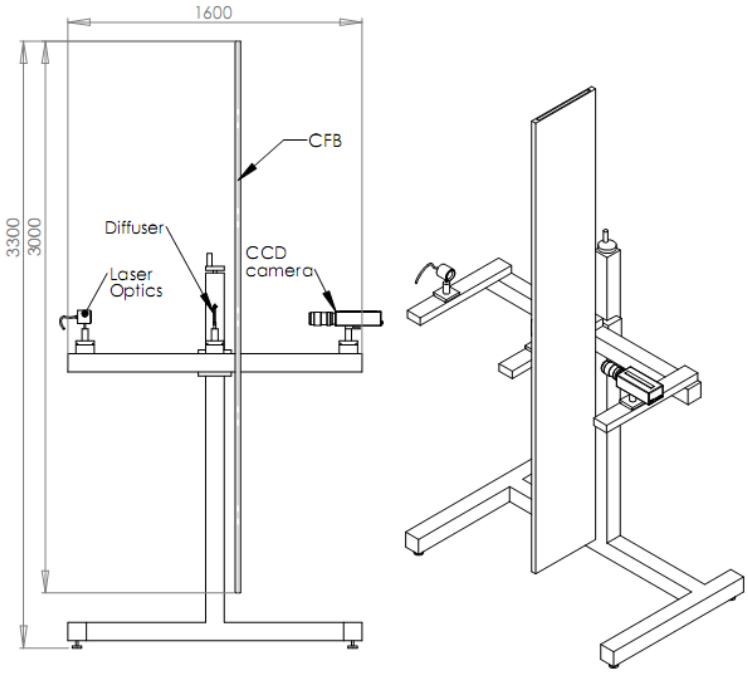

Figure 6.13. *The measurement setup for the pulsed light measurements.*

Backlighting, i.e. directing the light from behind, creates a shadow image with the particles in the focus plane appearing sharp while those outside of it appear blurred. The cross-correlation algorithm of PIV displacement measurement weights the sharpest particles, as they create the highest intensity peaks in the inverted image. However, the velocities can only be determined if the light can penetrate the suspension. In the CFB this is does not happen at the lowest void fractions, which locally affects even the average fields. With the non-dilute suspensions found in the CFB, it is vital that the focal plane is as thick (Depth-Of-Field, DOF) as the riser, so that unfocused particle shadows don't drown out the measurement signal. Figure 6.14 shows a sample of the recorded images and Figure 6.15 shows the velocity vector field, the volume fraction and the sub-3.3mm scale particle random motion energy calculated from it based on the PIV correlation peak widths.

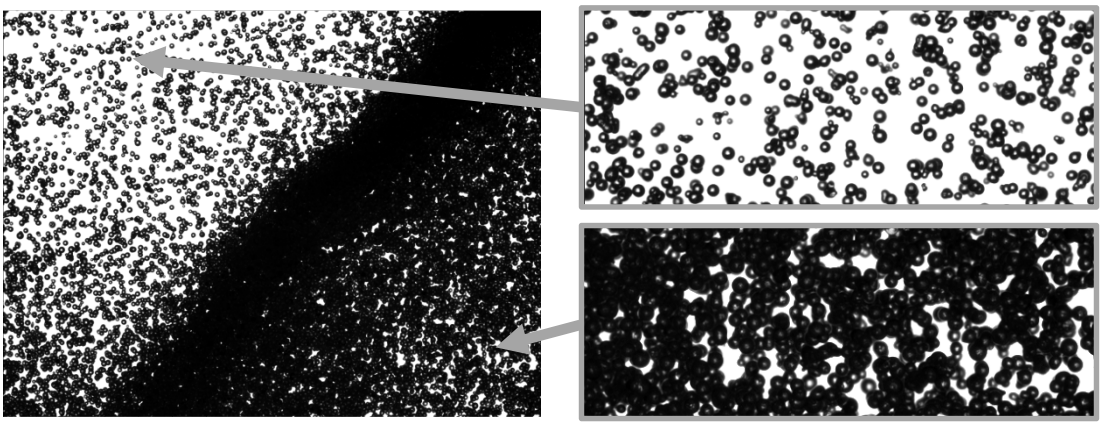

Figure 6.14. *Sample image recorded with pulsed diode-laser backlight.*

For the backlit image, the grey-scale volume fraction estimate is used to determine the local particle volume fraction. Because it is important to penetrate as dense suspensions as possible, an overexposed image background in areas with no particles is unavoidable given the cameras used. In this case, the large DOF mentioned earlier also helps with the volume fraction estimate: as all the particles are in reasonable focus they create a sharp shadow image, and are visible even against the overexposed background.

If front lighting were to be used, the light would be directed from the direction of the camera. In this type of lighting, the intensity peaks are generated by the particles closest to the front wall. The velocities of these particles can be determined at any void fraction, but these velocities only represent the particles right next to the wall. Another drawback is that there is no easy way to estimate the void fraction. The front-lit method could be used to study those regions where the backlighting fails, because of low void fractions. In the present study front-lighting was merely tested and no valid measurements were carried out. Even for backlight illuminated images it might be beneficial to add a low-powered light source to the front. This light could be used to

provide just enough light to extend PIV velocity measurement to the densely packed regions. However, this would slightly further compromise the grey-scale volume fraction estimate. Testing of the setup is outside the scope of this thesis, but further investigation of the approach might be useful.

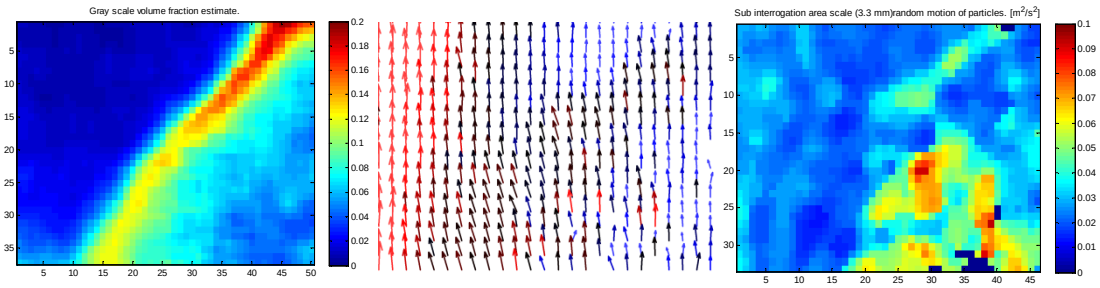

Figure 6.15. Particle v*olume fraction, PIV velocity vectors and sub 3.3 mm scale particle random motion energy calculated from the sample image shown in Figure 6.13.*

In this study, a Cavitar CaviLux Smart diode-laser was used because of its portability. The laser and optics were connected with an optical fibre and an aluminium stand was constructed to support the camera and laser optics. The power of the laser limits the size of the usable measurement window to around 40 mm, owing to the small lens aperture needed for the large DOF. The smaller the window, the shorter the time delay between the images has to be, while the displacement of the particles relative to the measurement window increases. This image size necessitates the use of double frame imaging in order to achieve a sufficiently brief time delay. The maximum pulse length of the laser also decreases as the triggering frequency increases. These limitations make it impossible to achieve time resolution with the equipment used, and the calculated fields have to be considered as discrete samples. The spatial resolution of the method is around 1.65 mm with the 40 mm measurement window used.

As time resolution cannot be achieved – and is not required for statistical results – the imaging frequency can be chosen freely. Thus, the sampling can be spread over a long period of time, without collecting an unwieldy amount of data, making the calculation of a representative average field more convenient. With a suitably low triggering frequency, the number of recorded frames is only limited by the hard drive capacity, instead of the camera buffer. At least 1000 double frame 1600x1200 pixel images were recorded with a Sigma 105mm f/2.8 lens and ImperX Lynx 2M30 CCD-camera set at animaging frequency of 5 Hz and aperture of f/16, giving a minimum sampling period of 200 s for each measurement point.

7. RESULTS AND DISCUSSION

In the measurements, a considerable amount – over 500 GB – of image data was recorded. Because of time constraints and computational cost of the data analysis, the small-scale measurement results presented in this thesis include only the riser cross-section profiles at heights of 0.8 m and 1.2 m. The application of PTV to measure particle velocities and size distributions in dilute regions has also been left outside the scope of this thesis, although the algorithmic framework for the purpose exists.

In this chapter the simulation results are briefly presented in section 7.1, and in section 7.2 they are compared to the measurements. The measurement results and their interpretation are also discussed in this section. In all plotted graphs of this chapter, red and black marker colours are used to denote the fluidization velocities 3.25 m/s and 3.75 m/s respectively.

7.1. Simulations

The instantaneous sample fields of Figure 7.1 have similar, complicated flow structures as the experimental device. The particles collect on the walls as clusters and fall down. However, the smallest clusters seen in the experimental device are missing because of the 5x5 mm control volume size used. Also, there are large particle clusters in the top portion of the riser that are not commonly found in the experimental device. The low granular temperatures in dense regions are caused by strong dissipation at high particle volume fractions. At the bottom a large cluster forces the fluidization air up along the left wall as a high speed jet. The highly unsteady nature of the CFB means that quantitative comparison of instantaneous fields is difficult and average fields are better suited for quantitative comparison.

The simulated average fields in Figures 7.2 and 7.3 display physically correct behaviour, but it is evident from the mean velocity and volume fraction fields, that the 30 second averaging period is inadequate to generate stable average fields. This makes detailed comparison between the results inappropriate, although they are adequate for qualitative comparison in the context of a feasibility study.

In the mean results, particles travel upwards in the middle of the riser, downwards on the walls and move outwards from the middle towards the walls, as expected. Particles falling down by the walls move back to the middle of the riser at the bottom and are

blown up again by the air inlet. The solids return tube at the height of 0.6 m on the right side creates an asymmetrical flow field in the lower portion of the riser. This is most evident in horizontal velocities above the solids return where the particles move towards the wake of the returning solids on the right.

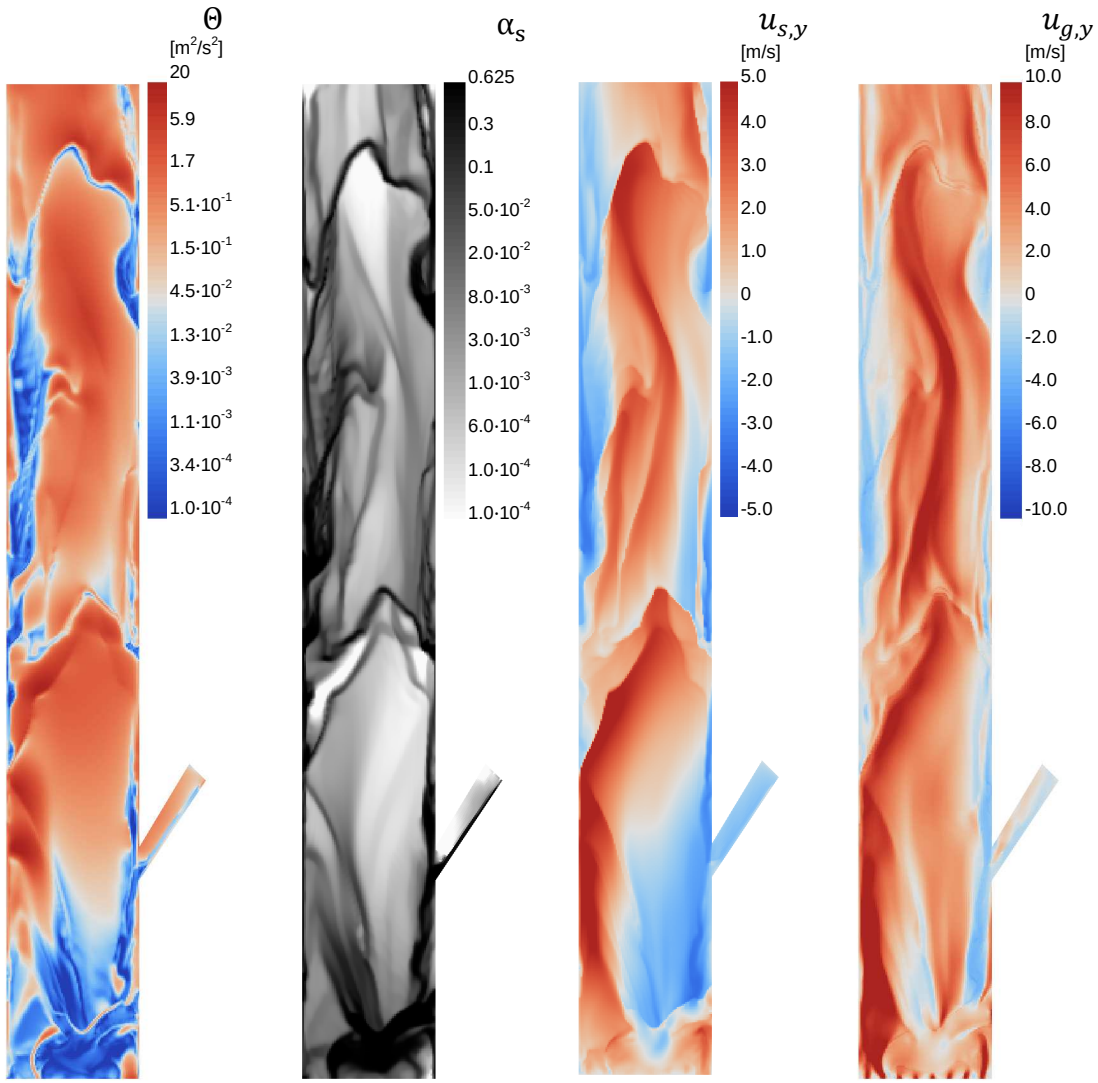

Figure 7.1. *Instantaneous samples of simulated granular temperature, particle volume fraction and vertical velocity and gas vertical velocity fields. Fluidization velocity is 3.75 m/s and without a turbulence model.*

An increase in fluidization velocity increases vertical particle velocities as expected. The introduction of the SGS-turbulence model has the expected smoothing effect on the average fields, caused by the increased diffusion. The turbulence model also decreases the particles' upwards velocity at the fluidization velocity of 3.75 m/s. In the mean volume fraction fields of Figure 7.3 the turbulence model has little effect. Overall the volume fraction fields appear physically correct, with particles collecting on the walls and at the bottom. Increased fluidization velocity also has the expected effect: increased

circulation with particles spreading out more vertically i.e. with more solids at the top and less at the bottom.

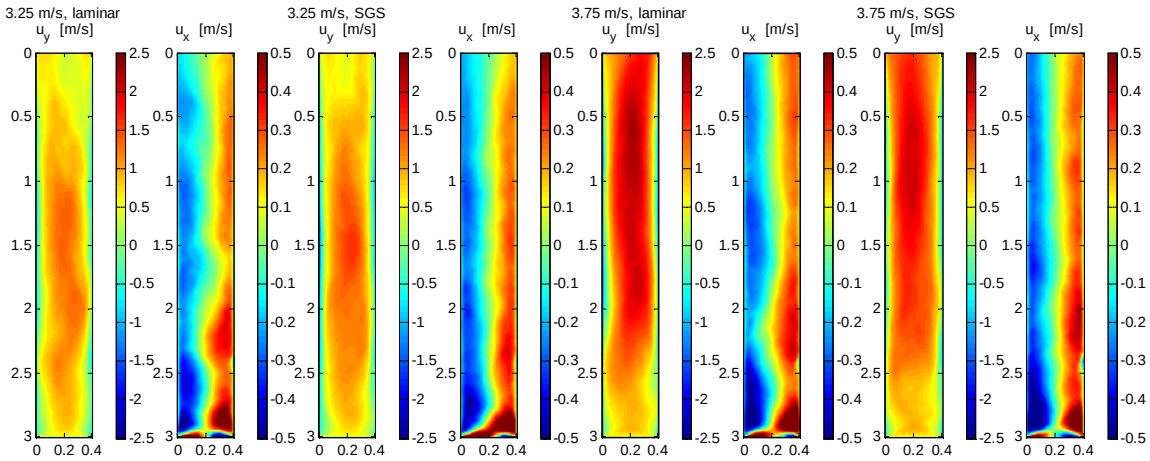

Figure 7.2. *Simulated vertical and horizontal particle mean velocity fields for fluidization velocities 3.25 m/s and 3.75 m/s, both with and without the Smagorinsky sub-grid scale turbulence model. Simulated time period is 30 s.*

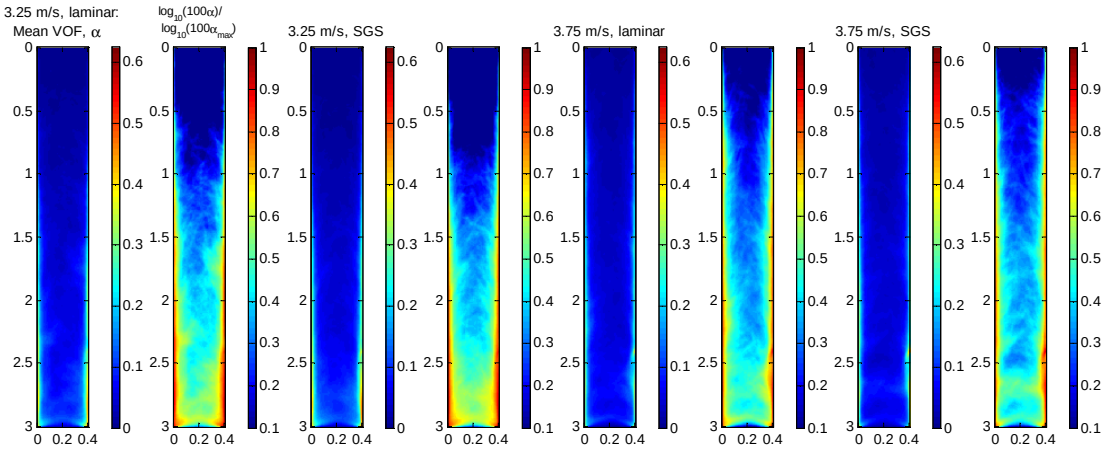

Figure 7.3. *Simulated particle mean volume fraction fields for fluidization velocities 3.25 m/s and 3.75 m/s, both with and without the Smagorinsky sub-grid scale turbulence model. The averaged time period is 30 s.*

7.2. Measurements, Comparison and Discussion

This section begins with an analysis of the large-scale behaviour of the pilot-scale CFB, based on the results of time-resolved PIV measurements and comparison with the simulations. In section 7.2.2 a more detailed comparison of the large-scale time resolved PIV measurements and simulations with riser cross-section profiles measured with

pulsed laser illumination is carried out. The good resolution and long sampling period of these pulsed light measurements allow calculation of meaningful derived quantities. Section 7.2.3 presents the results for volume-fraction-weighted i.e. Favre-averages and Reynolds stresses. These quantities are important for time-averaged modelling of a CFB. In the last section, 7.2.4, particle small scale random motion results are presented and their interpretation is discussed.

7.2.1. Large-Scale Behaviour

As was the case with the CFD-simulation results, it is evident from Figure 7.4 that the 28 second sampling period used in the continuous light (i.e. large scale, time-resolved) measurements is inadequate for averaging. A positive note is that the simulations and the experimental device seem to have similar chaotic time-scales. At the violent and rapidly changing bottom these time-scales are shorter than in the rest of the riser, resulting in smoother average fields with the sampling period used.

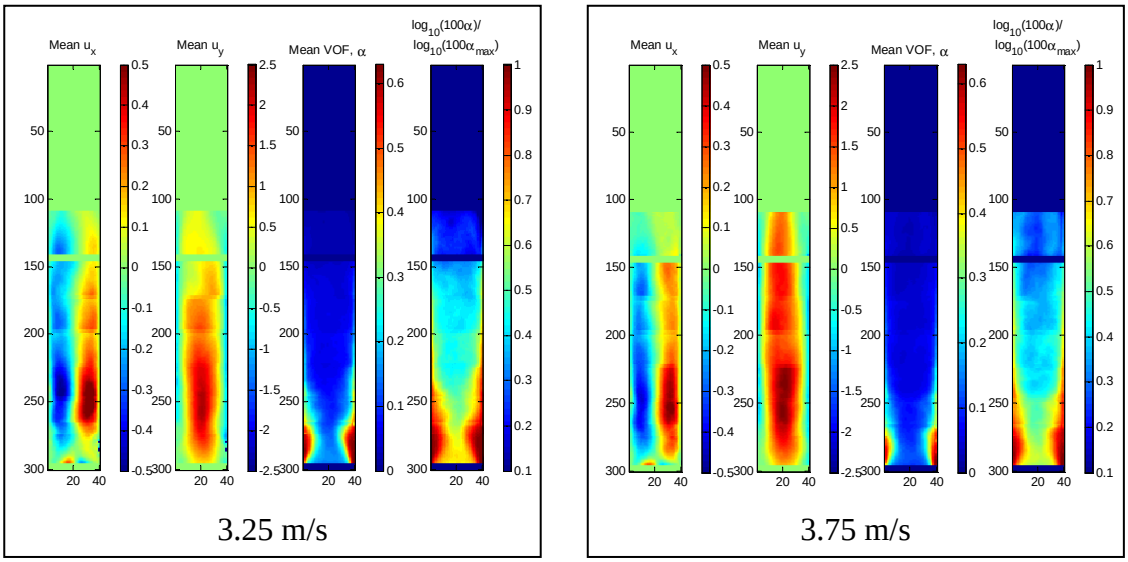

Figure 7.4. *Experimental mean horizontal, u_x, and vertical, u_y, velocities and mean particle volume fraction, α_s, fields measured with time-resolved PIV at fluidization velocities of 3.25 m/s and 3.75 m/s. The whole cross-section of the riser is included in the fields and areas with no measurement data are padded with zeros.*

However – again from a qualitative perspective – there are clear differences between the measured and simulated mean flow fields. In the experimental device, large chunks of packed or almost-packed particles collect on the side walls at heights below 0.5 m. These chunks are not present in the simulated mean fields. The packed particles effectively funnel the fluidization air up through the middle of the riser as a high speed jet, as shown by the instantaneous samples in Figure 7.6, with the rapid acceleration of

particles caught in the jet. The effects of the chunks and central air jet continue up the riser with wide, descending wall layers.

The difference in particle distributions is also clearly demonstrated in the graph of the horizontal mean particle volume fraction over the height of the riser in Figure 7.5. In the experimental device, a large portion of the particles are in the lowest 0.7 m of the riser, meaning there are less of them higher up.

The differences between the simulations and measurement could be explained by several uncertainties and approximations in the modelling, but one possible cause for the differing behaviour is friction on the front and back walls of the pseudo-2D experimental device. This friction is not present in the 2D-simulations. In the lower 0.7 m of the riser, packed clusters often extend wall-to-wall across the riser depth. For these clusters, it is reasonable to assume that the friction on the front and back walls is significant. The effect should be evaluated with measurements using less bed material and with 3D-simulations that include the wall friction.

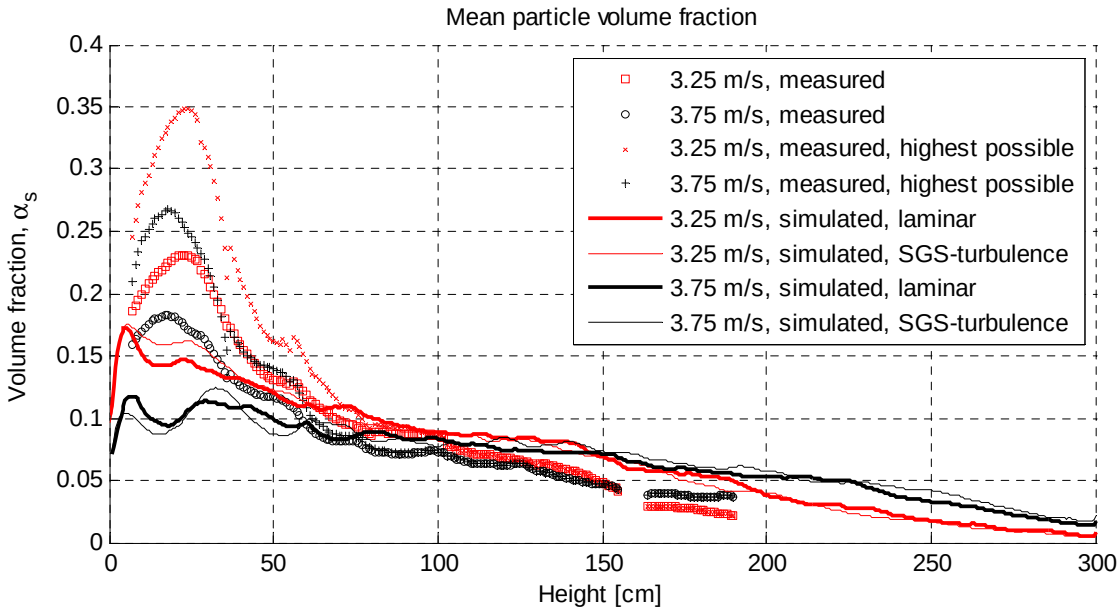

Figure 7.5. *Measured and simulated vertical mean volume fraction profiles. For the measurements an estimate of the highest possible mean volume fraction is included owing to the limitations of the grey-scale volume fraction estimate at high particle volume fractions.*

The densely packed clusters at the bottom also highlight the limitations of the grey-scale volume fraction estimate. As the highest reliably measurable volume fraction is 0.35, the mean volume fraction is underestimated in these regions. The upper limit for the possible mean particle volume fraction was calculated – as explained in section 6.1– and

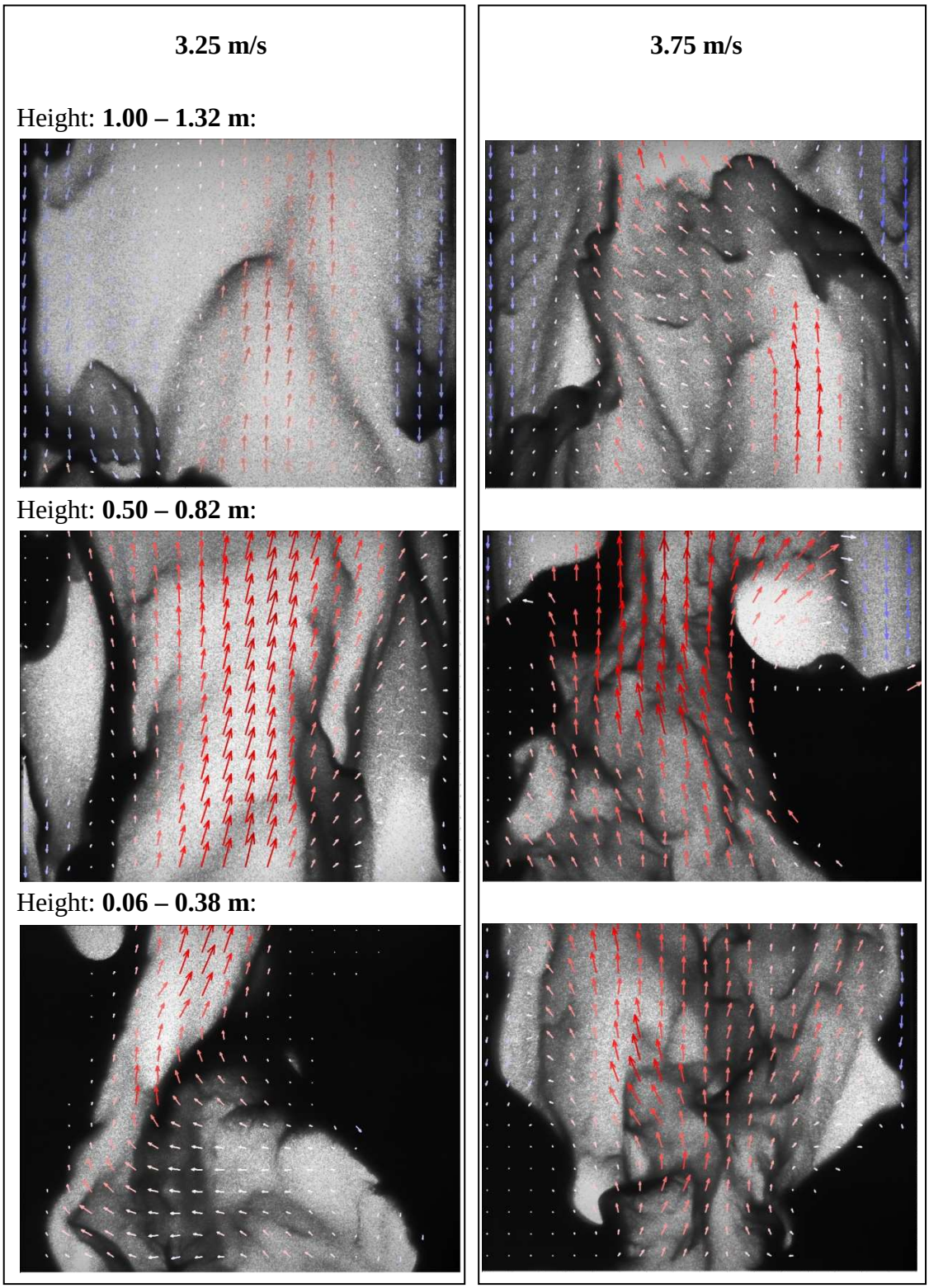

Figure 7.6. *Sample frames recorded with high speed camera of the CFB riser at heights 0.06-0.38m, 0.50-0.82m and 1.0-1.32m. The recorded images are overlaid with particle velocity vectors calculated with time-resolved PIV. 25% of the calculated vectors are shown. The dark regions on left and right edges of the 0.06-0.38 m and 3.75 m/s 0.50-0.82 m pictures are glass beads packed wall-to-wall.*

is included in Figure 7.5 as the highest possible measured volume fraction. At heights below 0.5 m, the actual values are probably closer to the upper limit and above 0.5 m closer to the unmodified measurement. Further up, the difference between the two vanishes, as packed clusters no longer occur.

7.2.2. Simulated and Measured Mean Cross-Sections

While the large scale, time-resolved measurements provide a good overall view for qualitative analysis, their resolution and accuracy – as well as the sampling period mentioned earlier – leave room for improvement. This is particularly so close to the walls, where the velocity gradients are sharp. Figures 7.7 and 7.8 display the mean volume fraction and mean vertical velocity profiles across the riser cross-section at heights of 0.8 and 1.2 m. Results are included from pulsed light (small scale) measurements, continuous light measurements and CFD-simulations.

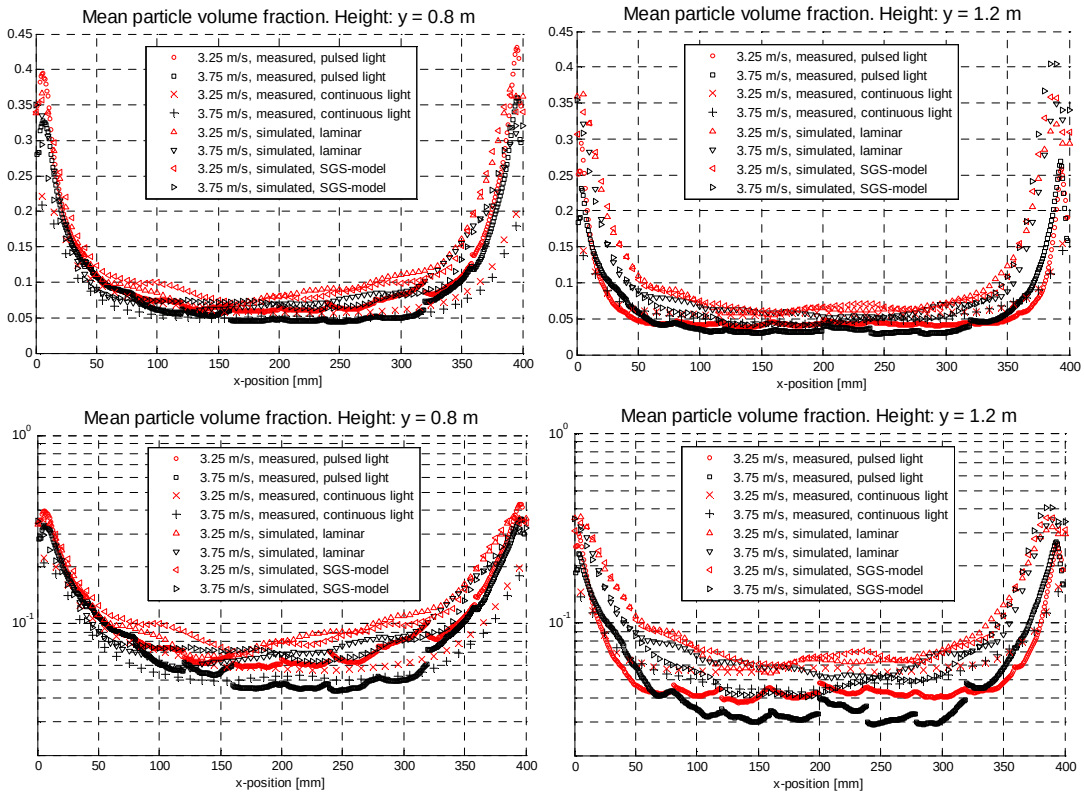

Figure 7.7. *Measured and simulated horizontal mean volume fraction profiles at heights of 0.8 m and 1.2 m, and fluidization velocities of 3.25 m/s and 3.75 m/s.*

The pulsed light measurements have a sampling period of 3 min 20 s as opposed to the periods of 28 s and 30 s in the continuous light measurements and CFD-simulations respectively. The longer sampling period produces more stable average fields, as demonstrated by the largely good match between the individual small scale

measurement windows. In large scale measurements and CFD the profiles are drawn from a single averaging window, but the inadequacies of sampling cause uneven and asymmetric profiles.

The velocity profiles in Figure 7.8 clearly show how the sharp velocity gradient close to the wall, seen in the small scale measurements, cannot be captured by the large scale measurements. The simulated and measured velocities also differ, but comparison is mostly meaningless because of the different bottom bed behaviour mentioned earlier. Here the good overall look provided by the large scale measurements shows its value: it would have been difficult to notice the differences in the large scale behaviour of the experimental device and the simulations from the few cross-section profiles gained from the small scale measurements. Large scale measurements provide general qualitative (and quantitative to a degree) information, while the small scale ones provide accurate numerical data in limited areas.

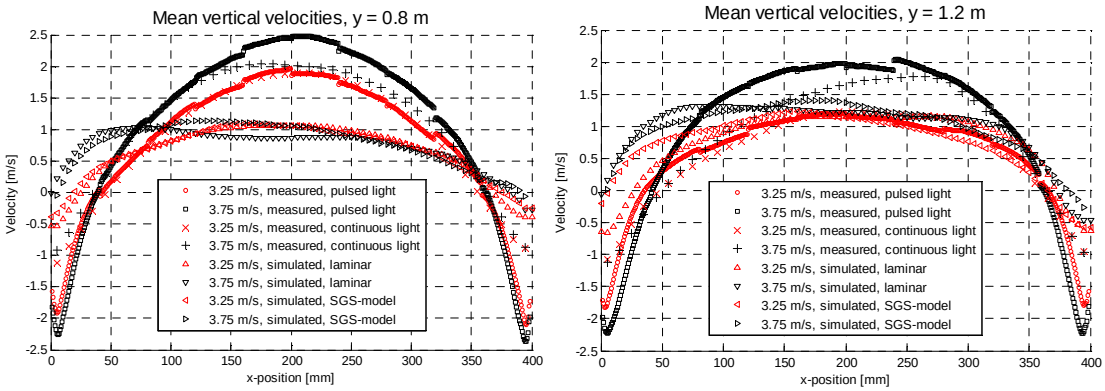

Figure 7.8. *Measured and simulated horizontal particle mean vertical velocity profiles at heights of 0.8 m and 1.2 m, and at fluidization velocities of 3.25 m/s and 3.75 m/s.*

The velocity standard deviation, $u_{i,RMS}\ i = x, y$, profiles in Figure 7.9 were calculated according to Equation 7.1 over time period T with time step of Δt. They display strong anisotropy between the vertical and horizontal components, and an increase in the vertical component which is roughly proportional to the increase in fluidization velocity. There is no change in the horizontal component. Overall the velocity fluctuations decrease slightly between the heights of 0.8 and 1.2 meters. The fluctuation quantities have only been calculated from the small-scale measurements, as the 28 s and 30 s sampling periods of CFD simulations and time-resolved PIV measurements are not long enough to generate valid results.

$$\bar{u}_i = \frac{1}{T}\sum_{t=0}^{T} u_i \, \Delta t, \quad i = x, y$$
$$u_{i,RMS} = \sqrt{\frac{1}{T}\sum_{t=0}^{T} [u_i - \bar{u}_i]^2 \, \Delta t}, \quad i = x, y \tag{7.1}$$

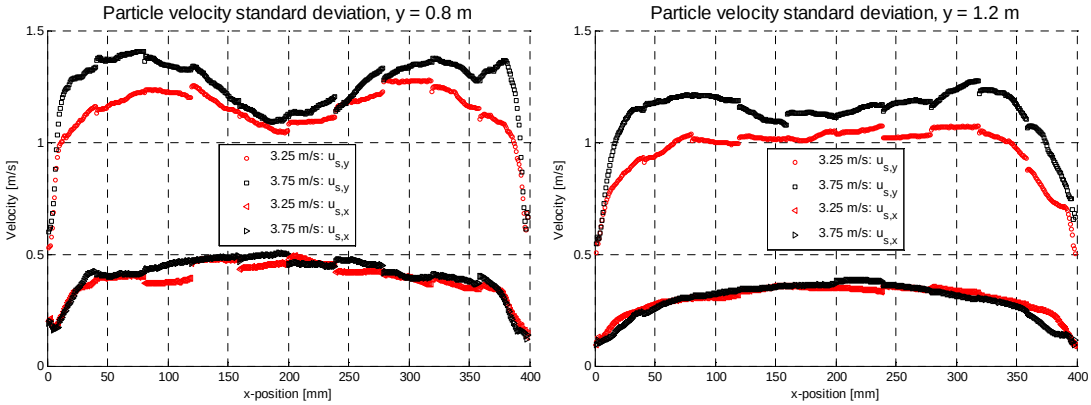

Figure 7.9. *Measured velocity standard deviations across the riser at heights of 0.8 and 1.2 m, and fluidization velocities of 3.25 m/s and 3.75 m/s.*

7.2.3. Favre-averages and Reynolds Stresses

The simultaneous velocity and volume fraction measurements allow calculation of derived quantities such as Favre-averaged velocities, $\tilde{u}_i, \; i = x, y$, and Reynolds stresses, $RS_{ij}, \; i = x, y$, as defined in Equation 4.5. From the discrete measurement data they were calculated with Equations 8.2-8.4. Figures 7.10 - 7.12 show these averaged over a time period of 3 min 20 s at heights of 0.8 and 1.2 meters. The uneven profiles mean that an even longer sampling period would be beneficial. The volume fraction weighting of the Favre-averages reduces the magnitude of particle velocities, as the particle clusters with the slower response times are weighted more and dilute areas where the peak velocities occur less.

$$\tilde{u}_i = \frac{1}{T}\sum_{t=0}^{T} \frac{u_i \alpha_s}{\bar{\alpha}_s} \Delta t, \quad i = x, y \tag{7.2}$$

The Reynolds stresses in Figures 7.11 and 7.12 are strongly anisotropic. The vertical component is of an order of magnitude larger than the horizontal and cross components. The non-normalized stresses in Figure 7.11 show similar changes in magnitude to the velocity standard deviations: they increase with fluidization velocity and decrease with

height. Close to the walls, the vertical stress component grows rapidly, while the horizontal component decreases. The maxima of the vertical component of the Reynolds stress roughly coincides with the minimum vertical particle mean velocity close to the wall.

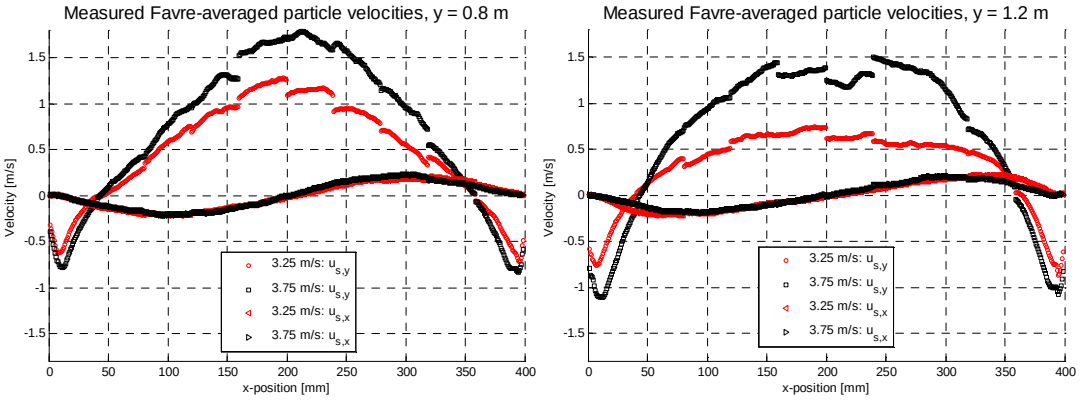

Figure 7.10. *Measured Favre-averaged particle velocities across the riser at heights of 0.8 and 1.2 m, and fluidization velocities of 3.25 m/s and 3.75 m/s.*

$$\overline{RS}_{ij} = \rho_s \frac{1}{T} \sum_{t=0}^{T} \left[\alpha_s u_i u_j - \bar{\alpha}_s \tilde{u}_i \tilde{u}_j \right] \Delta t, \quad i,j = x,y \tag{7.3}$$

$$\widetilde{RS}_{ij} = \overline{RS}_{ij} \Big/ \bar{\alpha}_s \rho_s, \quad i,j = x,y \tag{7.4}$$

In Figure 7.12 the Reynolds stresses are normalized by dividing them with mean particle volume fraction and particle density, as per Equation 7.4, to eliminate the effect of mean volume fraction. At the height of 0.8 m, the stresses are fairly similar at both fluidization velocities. The vertical components are highest in the middle of the riser and large values are also found in the 20 mm closest to the walls. As the fluidization velocity increases, the vertical stress component shows a slight increase, and the minima and maxima of the cross component move closer to the walls. At a riser height of 1.2 m, the stresses are generally lower and the wall regions are thinner. There is a larger difference in the vertical components between the fluidization velocities: at the higher fluidization velocity the low vertical component regions near the walls disappear. The magnitude of the cross component is roughly halved.

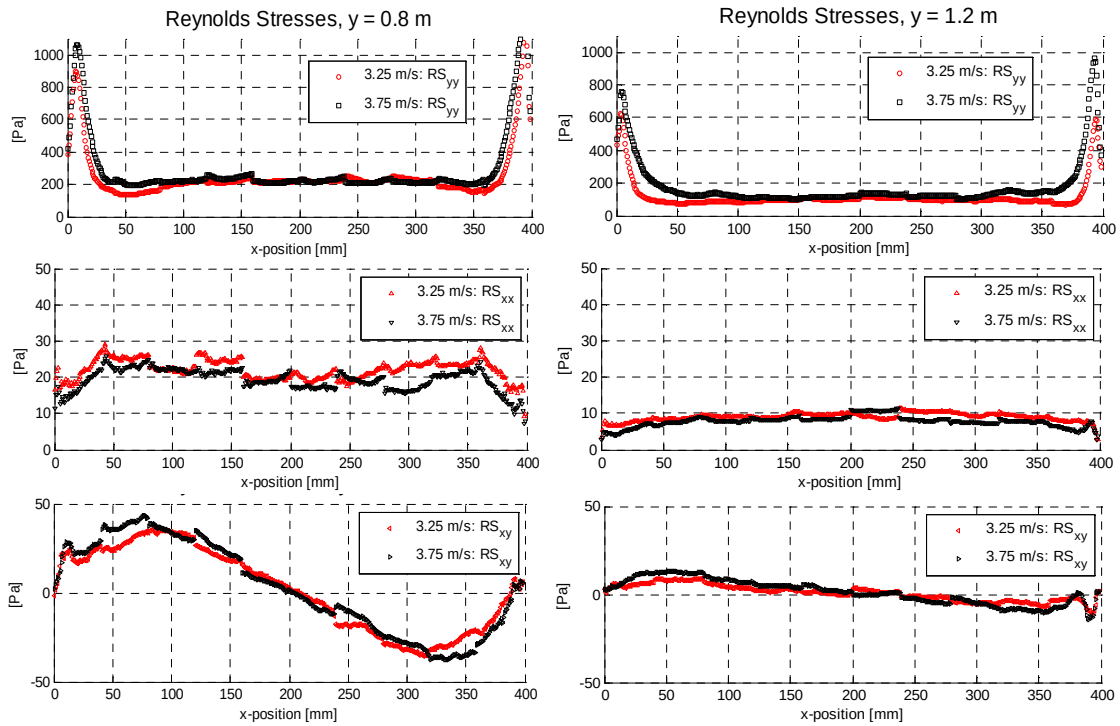

Figure 7.11. *Particle phase Reynolds stresses across the riser calculated with Equation 7.3 from measurements with pulsed laser illumination at heights of 0.8 and 1.2 m, and fluidization velocities of 3.25 m/s and 3.75 m/s.*

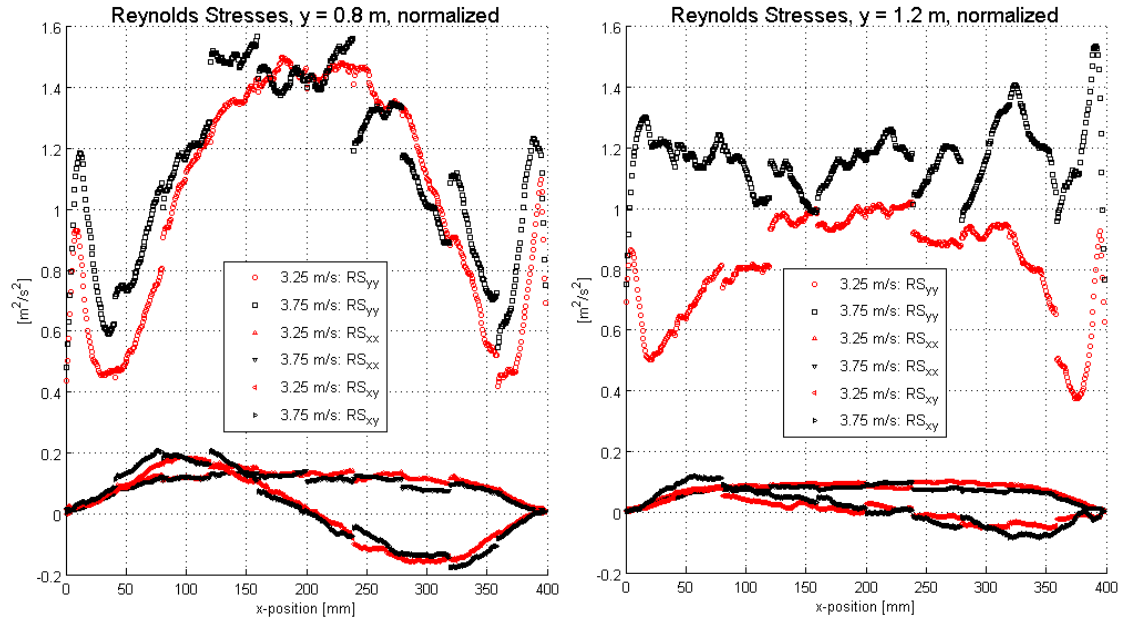

Figure 7.12. *Normalized particle phase Reynolds stresses, Equation 7.4, across the riser cross-section calculated from measurements with pulsed laser illumination at heights of 0.8 and 1.2 m, and fluidization velocities of 3.25 m/s and 3.75 m/s.*

7.2.4. Small-scale Particle Random Motion

Based on the testing described in Section 6.4.2, it can be said that the PIV correlation peak based method gives reliable results for particle random motion in a measurement volume. Relating the measurement results from the pilot scale CFB to granular temperature in the kinetic theory for granular flow is troublesome though, as the measurement volume (3.3x3.3x15.0 mm) includes the whole depth of the riser. As a result, the measurement of random particle motion includes any possible velocity gradients in the depth direction. In the case of the pilot scale CFB, these gradients probably represent the majority of the measured sub-3.3 mm random particle motion. As such, the highly anisotropic results of Figure 7.13 most likely tell more about the three dimensionality of the particle motion in the experimental device, than they do about the granular temperature as defined in the kinetic theory for granular flow. In the same Figure 7.13, the length scales used in the measurements of this section are illustrated by overlaying them on an instantaneous particle image and a corresponding PIV velocity vector field.

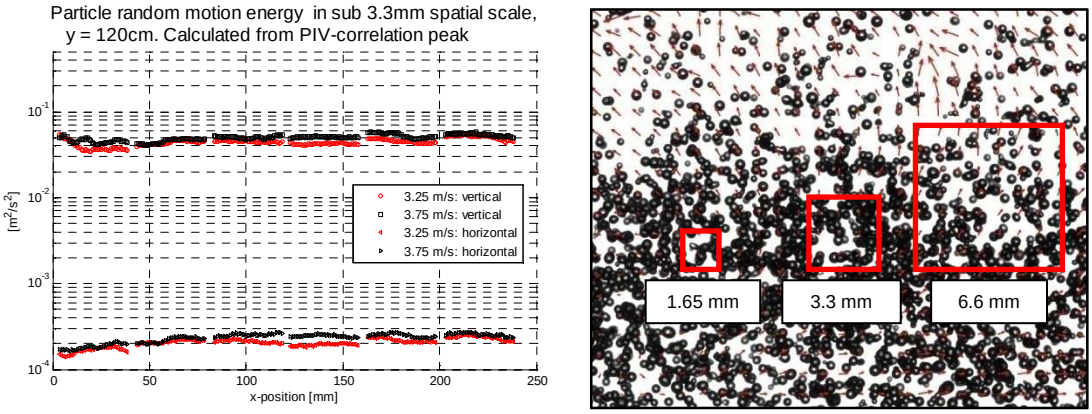

Figure 7.13. *Particle random motion energy in a measurement volume of 3.3x3.3x15 mm (HxWxD) calculated from the PIV correlation peak width. Fluidization velocities are 3.25 m/s and 3.75 m/s, and riser height is 1.2 meters. Length scales 1.65, 3.3 and 6.6 mm are illustrated with a sample picture. Particle velocity vectors measured with PIV are drawn in red. 1.65x1.65 mm interrogation area and 50% overlap was used for the correlation.*

The three-dimensionality shouldn't affect the PIV velocity measurements as much. The PIV gives a mean, or most probable, particle velocity for the whole measurement volume, subsuming any gradient inside the measurement volume. However, in dilute areas, where the measurement volume only includes a few particles, the three-dimensionality still has an effect. This effect can be seen in the erratic vector field of the top portion of the sample image in figure 7.14. In this dilute area, many of the 1.65x1.65

mm interrogation areas only include one or two particles. As the depth-wise location of the particle is unknown, possible depth-wise velocity differences appear as random particle motion in the measurement results.

The mean values for instantaneous particle random motion energy, $\overline{u'_{s,6.6mm,i}{}^2}, i = x, y$, in scales from 1.65 to 6.6 mm of Figure 7.14 also display significantly anisotropic behaviour. The results are calculated with Equation set 8.4 from PIV results. The PIV correlation used a 1.65x1.65 mm interrogation area and a 50% overlap. In Equation set 7.5, the ±3 spatial coordinates cover a 6.6x6.6 mm measurement area with $7^2 = 49$ datapoints. These results should be more comparable to the granular temperature, but they lack the smallest flow scales, and the upper limit of 6.6 mm is large enough to include a portion of large-scale particle fluctuations. This can also be seen in the scale illustration of Figure 7.13.

$$\bar{u}_{s,6.6mm,i} = \frac{1}{49}\sum_{x=x-3}^{x+3}\sum_{y=y-3}^{y+3} u_i\,, \quad i = x, y$$

$$u'_{s,6.6mm,i}{}^2 = \frac{1}{49}\sum_{x=x-3}^{x+3}\sum_{y=y-3}^{y+3}\left[u_{s,i} - \bar{u}_{s,6.6mm,i}\right]^2, \quad i = x, y \tag{7.5}$$

$$\overline{u'_{s,6.6mm,i}{}^2} = \frac{1}{T}\sum_{t=0}^{T} u'_{s,6.6mm,i}{}^2\,\Delta t, \quad i = x, y$$

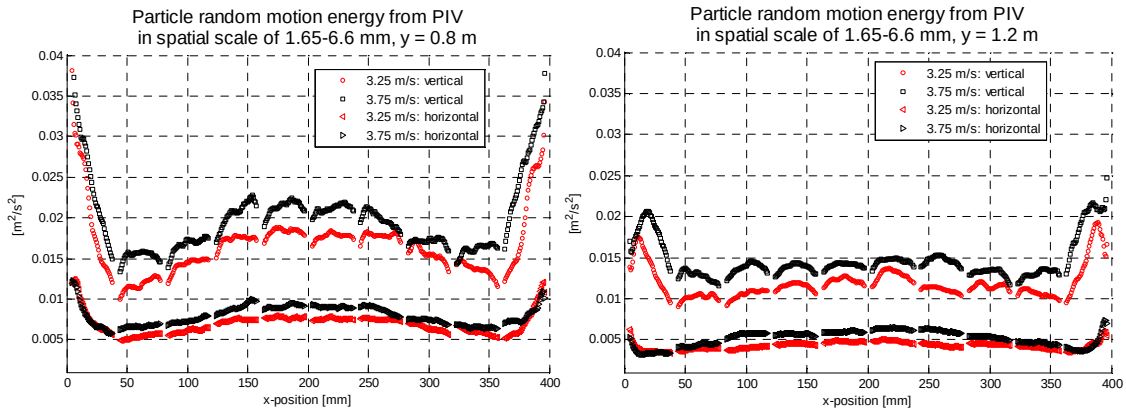

Figure 7.14. *Particle random motion energy in scale between 1.65 and 6.6 mm. Calculated from instantaneous PIV velocity fields. Riser heights are 0.8 and 1.2 m, and fluidization velocities are 3.25 m/s and 3.75 m/s.*

The effect of depth-wise velocity gradients on both the above measurement methods could – in dilute areas – be evaluated by applying PTV and depth-wise focus segmentation to the image data. Limiting the evaluation to dilute suspension could be

justified by the reduction of velocity differences in a dense suspension because of increased particle-particle friction. The PIV velocity measurement is also insensitive to depth-wise velocity gradients in which there is a large number of particles in the measurement volume. All in all, relating the measured small-scale random motion to the modelling parameters still requires further work.

8. CONCLUSIONS

The thesis concentrates on a pilot scale CFB located at Åbo Akademi, Turku, Finland. This device and its operating parameters are presented in Chapter 3, while the basic theoretical background of gas-solid flow and fluidization were reviewed in Chapter 2 to familiarize the reader with the concepts and principles discussed later in the thesis. The behaviour of the gas and particles in the CFB was studied both with simulations and experiments. The reduced pilot scale of the experimental device allows the application of refined methods that would not be feasible in an industrial scale CFB.

The Eulerian two-fluid method was used for the numerical simulations and they were carried out with an OpenFOAM based solver. The main objective of the simulations was to evaluate the feasibility of using OpenFOAM for CFB simulations. OpenFOAM is open source and, as such, an attractive platform for research, especially in an academic environment. While the public OpenFOAM release offers a pre-built solver as well as most of the required models, the stability and speed of the solution proved disappointing to the point that meaningful simulation of the pilot scale CFB was impossible.

To rectify the situation, a modified solver was written. To improve the stability and speed, a solution algorithm with adaptive under-relaxation and iterations within the time step was adopted. A more implicit treatment was used for the frictional pressure, and an algorithm was developed to eliminate the tendency of frictional pressure to act as an unphysical momentum source. The algorithm works by limiting the instantaneous frictional pressure magnitude in individual computational cells, based on in- and out-fluxes caused by the frictional pressure and the rest of the flow. This limiter proved to be the key feature for the stability of the solution. With these modifications, good speed of solution – also in parallel – and stability were achieved, making OpenFOAM a viable platform for transient CFB simulations. Attention could then be shifted to the physical modelling. The most significant additions to the physical models were adaptation of a filtered approach for turbulence modelling, with the Smagorinsky (1966) SGS-model, and the addition of Johnson and Jackson (1987) boundary conditions for the particle phase. The simulation results appear physically consistent, but they do differ from the behaviour of the experimental device.

Image-based measurement methods were used for the experimental work. For imaging the CFB riser was illuminated from behind owing to the limitations of device geometry

and light penetration. Several different methods, each with their strengths and weaknesses, were reviewed and some of them applied to the pilot scale CFB. The methods applicable to the pilot-scale CFB are listed in Table 8.1. Imaging was carried out with two sizes of measurement window: over the whole width of the riser for a general overview and with a small enough window to allow the detection of individual particles.

The grey-scale volume fraction estimate applied to the images has the major advantage of simultaneous volume fraction and velocity measurement, which allows the calculation of derived quantities useful for modelling, such as volume fraction weighted averages and Reynolds stresses. The method however, requires good lighting and the definition of correct reference values can be challenging. The method is also incapable of resolving volume fractions where the light does not measurably penetrate the suspension. These limitations mean that while the results are useful for qualitative analysis and the calculation of the derived quantities, the quantitative accuracy leaves much room for improvement.

For both image sizes the particle velocities were calculated with PIV, which on the small scale proved accurate and capable of resolving velocities at a wide range of volume fractions. However, the velocities cannot be determined with backlight illumination if no light penetrates the suspension, as is the case with the fully packed regions of the pilot scale CFB. With the larger imaging area PIV proved incapable of capturing the sharpest velocity gradients, but – even with the sub-optimal accuracy – the results provide a valuable overall picture of the flow and time-resolved visualization and data. A comparison of these whole-field results with the simulations shows a clear qualitative difference in the large-scale behaviour of the flow, possibly caused by friction at high particle volume fractions on front and back walls of the experimental device.

The high accuracy and long sampling periods of the small imaging area measurements allow meaningful calculation of particle fluctuation quantities: Reynolds stresses and small-scale particle random motion energy. The Reynolds stresses were measured to be highly anisotropic – by an order of magnitude. The small-scale random motion was measured with two different methods, in the first of which it was calculated as local instantaneous fluctuations in PIV velocity fields. This method is only capable of capturing particle motion in scales larger than the PIV interrogation area. The second method utilized the change in the PIV correlation peak width and is able to measure the random motion in scales smaller than the PIV-interrogation area. However, both of the methods are affected – at least to a degree – by the possible three-dimensionality of the pseudo two-dimensional experimental device. Interpretation of these results requires further study. Most of the anisotropy in the measured small-scale random motion is

probably caused by the velocity gradients across the riser depth, instead of describing the particle fluctuations as defined in the kinetic theory.

Table 8.1. *Strengths and weaknesses of the reviewed measurement methods applicable to the pilot-scale CFB.*

Method	Strengths	Weaknesses
Grey-scale VOF estimate	- Simultaneous measurement of volume fraction and velocities - Good spatial and temporal resolution	- Definition of reference values is challenging - Incapable of resolving high particle volume fractions - Sensitive to lighting conditions
Time-resolved PIV with fluorescent backlight illumination	- Time-resolved data - Large measurement area - Excellent visualization of the physical phenomena - Analysis of large scale behaviour	- Spatial resolution - Long sampling periods require large datasets - Incapable of determining velocities at volume fractions close to the packing limit
PIV with pulsed laser backlight illumination	- Excellent spatial resolution - Possibility to extend with the correlation peak width based calculations - Reasonably sized datasets - Applicable to wider range of volume fractions	- Not time-resolved - Incapable of determining velocities at volume fractions close to the packing limit
Shadowgraphy PTV	- Best possible spatial resolution - Measurement of particle size, shape etc. - Possibility of depth-wise focus segmentation	- Only applicable in dilute regions - Higher computational cost than with PIV - Careful calibration needed for accurate size measurements and depth-wise focus segmentation

The two measurement scales complement each other, and neither could comprehensively characterize the particle flow on their own. Together they provide both detailed numerical data and cover the large portions of the riser needed to analyze the

large-scale behaviour of the CFB. Although a lot has been covered, more work is still needed. Possible directions for future research are listed below.

Recommendations for future work:

- Evaluation of the effects of wall friction on the large scale behaviour of the experimental device, with experiments using low particle loads and 3D-simulations to include the front and back wall friction.

- Application of PTV in dilute regions to compare particle size distribution in different locations.

- Evaluation of the effect of flow three-dimensionality on the small scale particle random motion measurements, by applying PTV with depth-wise focus segmentation.

- Cluster size measurements from existing image data.

- Further statistical analysis of the data. For instance, segmentation of velocity measurements based on volume fraction or cluster size.

- Experimentation with simultaneous front- and backlighting to enable PIV particle velocity measurements at all volume fractions.

- Combining the grey-scale volume fraction estimate with a more reliable, non-time-resolved volume fraction method in order to obtain more accurate mean volume fraction values and calibration of the grey-scale estimate.

REFERENCES

Agrawal, K., Loczos, P.N., Syamlal, M., Sundaresan, S., 2001. The role of meso-scale structures in rapid gas-solid flows. Journal of Fluid Mechanics 445, p. 151.

Bouillard, J.X., Lyczkowski, R.W., Gidapow, D., 1989. Porosity distributions in a fluidized bed with an immersed obstacle, AIChE Journal 35, pp. 908-922

Crowe, C., Sommerfeld, M., Tsuji Y. 1998. Multiphase flows with droplets and particles, CRC Press, 471 p.

Derevich, I.V., 1988, Inzhermo-Fizicheskii Zhurnal 55(1), pp. 26-31

Elgobashi, S.E., 1991. Applied Scientific Research 48, pp. 301-304

Enwald, H. Peirano, E. Almstedt, A. 1996. Eulerian two-phase flow theory applied to fluidization. International Journal of Multiphase Flow 22, pp. 21-66

Ergun, S. 1952. Fluid flow through packed columns. Chem. Engineering. Progr. 48 pp. 89-94

Ferziger, J.H., Peric, M., 2002. Computational Methods for Fluid Dynamics, 3rd rev. edition. Springer-Verlag, Berlin, Heidelberg, New-York. 423 p.

Geldart, D. 1973. Types of gas fluidization, Powder Technology 7, pp. 285-292.

Gibilaro, L.G., Di Felice, R.I., Waldram, S.P. 1985. Generalized friction factor and drag coefficient correlations for fluid-particle interactions. Chem. Engineering Science 40, pp. 1817-1823.

Gidaspow, D., Syamlal, M., 1985. Solid-gas critical flow. AIChE Meeting, Chigago, 10-15 November.

Gidaspow, D., 1994, Multiphase Flow and Fluidization, 1st edition, Academic Press, New York, 467 p.

Grace, J.R., Knowlton, T.M., Avidan, A.A. 1997. Circulating Fluidized Beds. Blackie Academic & Professional, London, 608 p.

Grasa, G., Abanades, J.C., 2001. A calibration procedure to obtain solid concentrations from digital images of bulk powders. Powder Technology 114, pp. 125-128.

Guldén, M. 2008. Pilotmodell av en cirkulerande fluidiserad bad. Master of science thesis, Åbo Akademi. 65 p.

Honkanen, M., Marjanen, K., 2007. Analysis of the overlapping images of irregularly-shaped particles, bubbles and drops. 6th International Conference on Multiphase Flow, ICMH 2007, Leipzig, Germany, July 9-13, 2007, Proceedings on DVD

Hrenya, C.M., Sinclair, J.L., 1997. Effects of particle-phase turbulence in gas-solid flows. AIChe Journal 43 (4), pp. 853-869.

Huilin, L. Gidaspow, D., Bouillard, J., Wentie, L, 2003. Hydrodynamic simulations of gas-solid flow in a riser using kinetic theory of granular flow. Chemical Engineering Journal 95, pp. 1-13.

Huilin, L. Yunhua, Z., Zhiheng, S., Ding, J., Juying, J., 2006. Numerical simulation of gas-solid flow in tapered risers. Powder Technology 169, pp. 89-98.

Ibsen, C.H., Solberg, T., Hjertger, B.H., 2000. A study of dilute to dense flow in a circulating fluidized bed. MFTP-2000, Internationl Symposium on Multiphase Flow and Transport Phenomena, 5-10 November 2000, Antalya, Turkey.

Ibsen, C.H., Helland, E. Hjertager, B.H., Solberg, T., Tadrist, L. Occelli, R., 2004. Comparison of multifluid and discrete particle modelling in numerical predictions of gas particle flow in circulating fluidised beds. Powder Technology 149, pp. 29-41.

Jasak, H. 1996. Error analysis and estimation for finite volume method with applications to fluid flow. PhD Thesis, Imperial College, University of London. 394 p.

Jenkins, J.T., 1992. Boundary conditions for rapid granular flow: flat, frictional walls, Journal of Applied Mechanics 59, pp. 120-127.

Jenkins, J.T., Louge, M.Y., 1997. On the flux of fluctuation energy in a collisional grain flow at a flat, frictional wall, Physics of Fluids 9(10), pp. 2835-2840.

Johnson, P.C., Jackson, R., 1987. Frictional-collisional constitutive relation for granular materials, with application to plane shearing. Journal of Fluid Mechanics 130, pp. 67-93.

Kallio, S. Airaksinen, J. Guldén, M. Hermanson, A. Peltola, J. Ritvanen, J. Seppälä, M. Shah, S. Taivassalo, V. 2009a. Experimental and numerical study of hydrodynamics in a circulating fluidized bed. Finnish-Swedish Flame Days 2009 proceedings, Naantali, Finland.

Kallio, S. Guldén, M. Hermanson, A., 2009b. Experimental study and CFD simulation of a 2D circulating fluidized bed. FBC20 Proceedings of the 20th International Conference on Fluidized Bed Combustion, Xi'an, China, May 18-21, 7 p.

Koch, D., 1990. Kinetic theory for a monodispersed gas-solid suspension. Physics of Fluids A 2, pp. 1711-1723.

Koch, D., Sangani, A.S., 1999. Particle pressure and marginal stability limits for homogenous monodisperse gas fluidized bed: kinetic theory and numerical simulations. Journal of Fluid Mechanics 400, pp. 229-263.

Launder, B. E., Spalding, D. B., 1974. The numerical computation of turbulent flows. Comp. Methods Appl. Mech. Eng. 3, pp. 269-289.

Kunii, D., Levenspiel, O., 1991. Fluidization engineering, 2nd edition, Butterworth-Heinemann series in chemical engineering. Reed Publishing, USA, 491 p.

Louge, M.Y., 1994. Computer simulations of rapid granular flows of spheres interacting with a flat, frictional boundary, Physics of Fluids 6(7), pp. 2253-2269.

Lun, C.K.K., Savage, S.B., Jeffrey, D.J., Chepurniy, N., 1984. Kinetic theories for granular flow of inelastic particles in coquette flow and slightly inelastic particles in a general flow field. Journal of Fluid Mechanics 140, pp. 223-256.

Lun, C.K.K., Savage, S.B., 1986. The effects of an impact velocity dependant coefficient of restitution on stresses developed by sheared granular materials. Acta Mechanica. 63, pp. 15-44.

Michaelides, E.E., 2006. Particles, Bubbles and Drops – Their Motion, Heat and Mass Transfer. World Scientific Publishing, Singapore. 410 p.

Ogawa, S., Unemura, A. Oshima, N.Z., 1980. On the Equation of fully fluidized granular materials. Zeitschrift fur angewandte Mathematik und Physik, 31, pp. 483-493.

Passalacqua, A. 2008. CFD simulation of gas-solid flows. PhD thesis. Politecnico di Torino, 144 p.

Passalacqua, A., Marmo, L., 2009. A critical comparison of frictional stress models applied to simulation of bubbling fluidized beds. Chemical Engineering Science, doi: 10.1016/j.ces.2009.03.005, 12 p.

Peirano, E. Leckner, B., 1998. Fundamentals of turbulent gas-solid flows applied to circulating fluidized bed combustion. Prog. Energy Combust. Sci. vol. 24, pp. 259-296

Pope, S.B., 2000. Turbulent Flows. Cambridge University Press, United Kingdom, 771 p.

Putkiranta, M., 2007. Spray measurements using shadowgraphy, Master of Science thesis, Tampere University of Technology, Department of Environmental Technology. 78 p.

Richardson, J.F., Zaki, W.N., 1954. Sedimentation and fluidization – Part 1. Trans. Inst. Chem. Engr. 32, pp. 35-53

Rietma, K., Mutsers, S.M.P., 1973. The effect on interparticle forces on the expansion of a homogenous gas-fluidized bed, Proceedings of the International Symposium on Fluidization, Toulouse, France.

Rusche, H. 2002. Computational fluid dynamics of dispersed two-phase flows at high phase fractions. PhD thesis, Imperial College, University of London. 343 p.

Samuelsberg, A., Hjertager, B.H., 1996. Experimental and numerical study of flow patterns in a circulating fluidized bed reactor. International Journal of Multiphase Flow 22(3), pp. 575-591.

Savage, S.B., 1998. Analysis of slow high-concentration flows of granular materials. Journal of Fluid Mechanics 337, p. 1.

Schaeffer, D.G., 1987. Instability in the evaluations describing incompressible granular flow. Journal of Differential Equations 66, pp. 19-50.

Schiller, L., Naumann, Z. 1935. Z. Ver. Deutsch. Ing. 77, p. 318

Shen, N., Tsuji, T. Morikawa, Y., 1989. Numerical simulation of gas-solid two-phase flow in a horizontal pipe. JSME 55, p. 2294

Smagorinsky, J., 1963. General circulation experiments with primitive equations. Monthly Weather Review 91, pp. 99-164.

Srivastava, A., Sundaresan, S., 2003. Analysis of a frictional-kinetic model for gas-particle flow, Powder Technology 129, pp. 72-85

Syamlal, M., O'Brien, T.J. 1988. Simulation of granular layer inversion in liquid fluidized beds. International Journal of Multiphase Flow 14, pp. 22-31

Syamlal, M., Rogers, W., O'Brien, T.J., 1993. MFIX Documentation: Theory Guide. Technical Report DOE/METC-9411004, NTIS/DE9400087, National Technical Information Service, Springfield, V.A., USA.

Tardos, G.I., 1997. A fluid mechanistic approach to slow, frictional flow of powders. Powder Technology 92, pp. 61-74.

Tsuji, T., Morikawa, Y., Shioni, H., 1984. Journal of Fluid Mechanics 139, pp. 417-434

Tsuji, Y., 2007. Multi-scale modeling of dense phase gas-particle flow, Chemical Engineering Science 62, Issue 13, pp. 3410-3418.

Weller, H.G. 2002. Derivation, modelling and solution of the conditionally averaged two-phase flow Equations. Technical Report TR/HGW/02, Nabla Ltd.

Wen, C.Y., Yu, Y.H. 1966. Mechanics of fluidization. AIChe Symposium Series 62, pp. 100-111.

Zhang, M.H., Chu, K.W., Wei, F., Yu, A.B., 2008. A CFD-DEM study of the cluster behavior in riser and downer rectors. Powder Technology 184, pp. 151-165.